# SYNTHESIS, CHARACTERIZATION, AND OPTICAL PROPERTIES OF COLLOIDAL ORGANIC DYE-CONTAINING FLUORESCENT CORE-SHELL SILICA NANOPARTICLES

A Dissertation

Presented to the Faculty of the Graduate School

of Cornell University

in Partial Fulfillment of the Requirements for the Degree of

Doctor of Philosophy

by

Erik Herz

August 2009

# SYNTHESIS, CHARACTERIZATION, AND OPTICAL PROPERTIES OF COLLOIDAL ORGANIC DYE-CONTAINING FLUORESCENT CORE-SHELL SILICA NANOPARTICLES

Erik Herz, PhD

Cornell University 2009

Since fluorescence was first observed in a solution containing quinine sulfate in 1845, methods employing fluorescent materials have abounded. Today, fluorescent probes are widely used in many fields, including biological imaging and security. For all applications brightness, stability, size control and compatibility are key parameters for probe design. Recent research to address these parameters has been focused on synthesizing nanoparticle materials. A class of those materials, core-shell silica nanoparticles, covalently encapsulating organic dyes within the core, have been found to be particularly effective in meeting the need for brighter, more stable probes, while also providing size and compatibility control.

This dissertation will describe how I have built on previous research by focusing on the synthesis, characterization and optical properties of core-shell silica nanoparticles that span the full spectral range, from ultraviolet to near-infrared emission. Through scattering corrected comparisons of coumarin dye-containing nanoparticles and dye in aqueous solution, relative quantum yield enhancements of an order of magnitude were measured. Similar brightness enhancements were observed when large Stokes-shift dyes were incorporated into the particles. By creating a graded series of Stokes-shifted particles, single-excitation functionality was added to the fluorescent core-shell silica nanoparticle platform, to allow for spectral multiplexing.

Since both light scattering and autofluorescence backgrounds in biological samples tend to be stronger at shorter wavelengths, new probe design has swiftly

moved toward near-infrared (NIR) excitation and emission. To this end, NIR fluorescent silica nanoparticles with emissions up to 800nm were synthesized and dye structure-optical property correlations were investigated. Using a self-built fluorescence correlation spectroscopy (FCS) instrument, cyanine dye containing particles of the NIR series were investigated in further depth. The FCS allows for measurement of the size, brightness and concentration of the particles in solution and, with small modifications to the beam-path also provides information on the fluorescence stability of the particles in solution, which is of particular importance in NIR probes. Photostability in aqueous solution was investigated for the NIR dye Cy5 and compared to the dye incorporated into particles, leading to findings that will impact future probe designs.

## BIOGRAPHICAL SKETCH

Erik Herz was born in Baltimore, Maryland, in December of 1979 to Margrit and Robert Herz. He spent his childhood enjoying the outdoors in northern Harford County's woods and fields. Seventh grade marked an important turning point in Erik's life. His seventh grade science teacher, Mr. Goetz, instilled in him a real love for science and understanding how things work. Also during Erik's seventh grade year, his father passed away due to late-stage cancer, and Erik grew up quickly, suddenly discussing decisions about the family business with his mother. Sorely missing his father, Erik put his full efforts into doing well in school. Throughout his time as a student at North Harford High School he was active in marching band and orchestra as a percussionist. In his senior year, he represented the student population of Harford County on the county school board. During the summers he enjoyed bailing hay, doing construction, and working at the local orchard.

In the fall of 1998, Erik began pursuing a degree in Materials Science and Engineering at Virginia Tech under the guidance of Prof. Ronald Kander, whose encouragement to become involved in research early was a key element in keeping Erik excited about science and engineering. Erik undertook a second and third major in Economics and International Studies, respectively, during his time at Virginia Tech, in order to better understand the decision making that often influences engineering. Under the research direction of Prof. Richard O. Claus and daily interaction with Dr. Ken Meissner, Erik completed a senior honors thesis and subsequent M.S. thesis in Materials Science and Engineering on the synthesis of CdSe/ZnS quantum dots. His interaction with Dr. Meissner and Prof. Claus at Virginia Tech led him to decide to pursue further graduate work. With Dr. Meissner's encouragement, Erik applied for and was granted a Fulbright U.S. Student fellowship to research single quantum dot

optical phenomena in the physics department at the University of Dortmund, Germany, under the direction of Prof. Ulrike Woggon.

Erik was fortunate in meeting his wife, Ashley, early in college; upon learning of the Fulbright (and its accompanying spouse-only policy) they decided to be married in August 2003, three weeks after Erik defended his master's! A year of intense research into the optical physics associated with single quantum dots and a simultaneous year-long honeymoon followed in Dortmund.

After a brief visit to the Max Plank Institute for Polymer Research in Mainz, Germany, to do some solid-state NMR for his new mentor, Erik returned to the United States and settled into graduate life in Ithaca, NY. Erik earned a second M.S. in Materials Science and Engineering from Cornell University and thereafter completed his doctoral work in August of 2009.

*To my family:*

*von Herzen vielen Dank an Euch alle.*

# ACKNOWLEDGEMENTS

This section could go on for many pages and I am sure that I will inadvertently omit some deserving of thanks, let the words here indicate the gratitude that I feel towards everyone that has helped me in my pursuit of this dissertation.

First and foremost, I would like to thank Prof. Uli Wiesner for taking a chance on a young student from Virginia Tech and for convincing me to "see the light" and switch from my master's work on CdSe/ZnS nanoparticles to core-shell silica nanoparticles containing organic dye. His sound guidance on how to execute scientific research and his infectious excitement about good science have made my doctoral experience a privilege.

I also thank my committee members Prof. Alex Gaeta and Prof. Chekesha Liddell for their guidance and scientific advice over the years, and Prof. Wesley Sine for challenging me in his courses and for his suggestions on coursework in business.

Special thanks goes out to all of my collaborators in the Webb, Frey, and Gaeta groups, as well as to Dr. Steve Switalski and Tom Marchincin at the Eastman Kodak Company in Rochester. Prof. Warren Zipfel and Dr. Johanna Dela Cruz were invaluable in helping to build the fluorescence correlation spectroscopy rig – Johanna, thank you very much for all of the hours spent in the dark depths of the Clark Hall basement turning micrometer screws and debugging fit routines.

Uli's group contains many members, past and present, who deserve independent mention. I thank the students who came before me for helping to build up the labs to where they were when I arrived – I have since learned how much work building labs is! Thank you. To Hooisweng Ow, thank you for all of the research that you did for your Ph.D., for the groundwork that you laid, and for teaching me the basics of sol-gel silica chemistry. To Andrew Burns, thank you for being a great

sounding board, partner in crime, bicycle mechanic, scientist and, most of all, friend throughout my time here at Cornell. Your encouragement, advice, and even the occasional kick in the pants kept my head above water! Hitesh, thank you for the late-night discussions in the Bard Hall sub-basement while you were doing AFM and I was working on FCS. Aey and Srikant, thank you for your constant wit and humor, as well as for all of your diligence in continuing the work on C dots. I thank Marleen, Scott, Chris, Hiro, Cathy, and all the other group members for their excellent discussion and challenges in group meeting, their comradeship, and encouragement.

In the laboratory, I would like to thank the undergraduate students who worked with me – Daniel Bonner, Akeisha Belgrave, Laura Connelly, and Peter Bai – for all of their hard work and independent thought.

My family, spread over a couple continents as it is, is the bedrock to which I can always turn for support, stability, and encouragement. My wife, Ashley, is my partner and best friend who is always there in the way that is needed most. Her love is a constant in an ever-changing world. Thank you for keeping me sane and reminding me of what is important in life. To my mom, thank you for always being there and for being both mom and dad after he passed away – you are an inspiration. To my sister Kristina, I want you to know that without your support at home, I would not have finished my Ph.D. now – thank you so much for taking care of Mom – you humble me in your selflessness.

Without all of the help from the staff at the Nanobiotechnology Center and the Cornell Center for Materials Research, I would still be trying to pull data from the DLS or make the optical table float.

Funding from the NSF through the Cornell Center for Materials Research, the Army (via NEI Corp.), Hercules Corp. and material support from Dyomics Gmbh over the years is gratefully acknowledged.

TABLE OF CONTENTS

LIST OF FIGURES

LIST OF TABLES

# CHAPTER 1

# AN INTRODUCTION TO FLUORESCENT SILICA NANOPARTICLES

## 1.0 Motivation

Since the discovery of fluorescence in quinine sulfate solution over 160 years ago, the use and study of fluorescence as a tool for imaging, sensing, and security applications has led to a wide array of probes used to track, tag, sense, and separate.[1] All of these applications benefit from brighter, more stable, and environmentally robust fluorescent probes and much research has been devoted to this challenge. With brighter probes, a higher signal to noise ratio is possible and leads to brighter, clearer images and higher sensitivity. Increased colloidal stability leads to better probe distribution throughout a given system (for example when particles are colloidally stable in blood, they will circulate throughout the body).[2] Increased photostability allows for longer imaging times and should allow for better signal to noise in ratiometric sensing systems.

## 1.1 Commonly available fluorescent species

The most commonly used probes are fluorescent dyes, fluorescent proteins, quantum dots, and hybrid particles, as shown in Figure 1.1, each with their own advantages and disadvantages.[3] Fluorescent dyes are small in physical size (1 to 2nm in their largest dimension), so they can quickly diffuse throughout, for example, a liquid system. Unfortunately, their chemical structure is in direct contact with the local environment, including solvents, ions, and other solutes, meaning that interactions

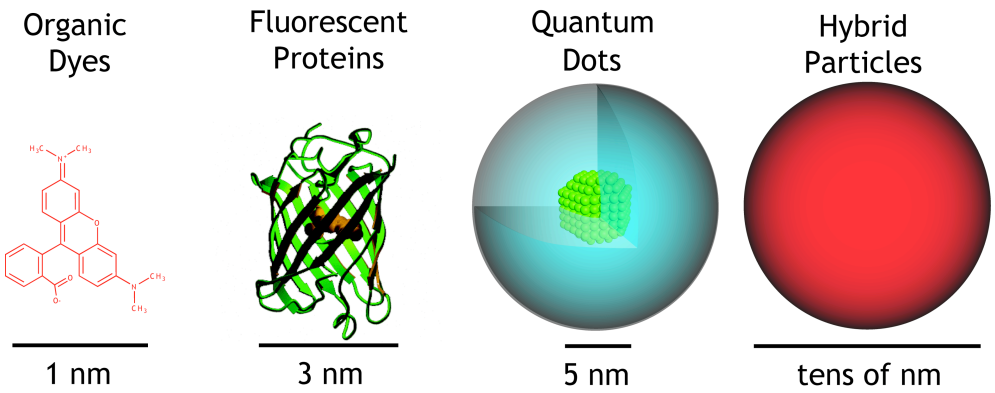


Figure 1.1: Schematic representations of the commonly available fluorescent probes, including dyes, fluorescent proteins, quantum dots and hybrid nanoparticles.

with the environment that quench the excited state or damage the dye molecule occur frequently, leading to photobleaching, triplet states, and other effects considered detrimental to dye fluorescence.[4,5] Fluorescent proteins are exquisite probes for biological function. They are slightly larger than dyes and are encoded for in the genes of interest such that when the genes are expressed, the fluorescent protein is also expressed. They suffer from similar drawbacks to dyes in that they photobleach and interact with their local environments. Quantum dots are semiconductor nanocrystallites that are very bright (with high quantum yields) and photostable.[6] They are considered to be some of the brightest available nanosized materials.[7] However, and unfortunately, quantum dots usually contain toxic heavy metal compounds such as lead, mercury, and cadmium, making production, use and disposal challenging at best.[8-10] Even when encapsulated, quantum dots have been found to leach toxic heavy metals over time in biologically relevant solutions.[11] Hybrid particles are a large subset of fluorescent probes that have been synthesized with a matrix material (either amorphous or crystalline) that entraps multiple dyes or quantum dots to produce a brighter probe. These particles are generally quite bright because they contain multiple dyes. When such particles physically entrap the dyes, there is a risk of the dye leaching from the particles over time. Furthermore, when the host matrix is a polymeric material, the particles tend to be sticky and aggregate. Finally, hybrid particles usually still suffer from the challenges, such as photobleaching, associated with the incorporated fluorophore.

## 1.2 An alternative radiative materials platform

This dissertation will build on previous research by focusing on the synthesis, characterization and optical properties of core-shell silica nanoparticles that span the full spectral range, from ultraviolet to near-infrared emission. Building upon the early fluorescent silica particle work of van Blaaderen *et al*[12], Nyffenegger *et al*[13], and Ow *et al*[14,15], over 30 different dye structures were incorporated during this work. In exploring the different dye structures that could be incorporated, several new conjugation chemistries for covalently incorporating the dyes were investigated. These are shown schematically in Figure 1.2, where the standard amine-terminated silane (3-aminopropyltriethoxysilane) shown at the top with the amine-isothiocyanate reaction coming from the original work by Ow and coworkers. The middle silane (3-mercaptopropyltrimethoxysilane) has been quite useful for incorporating dyes that are not available with amine-reactive linkages and has allowed for the production of very small silica nanoparticles. Finally, the bottom silane (3-isocyanatopropyltrimethoxysilane) is both amine reactive and hydroxyl reactive.

This dissertation is structured in the following way. In the second chapter there is an in-depth introduction to the core-shell silica nanoparticles platform, elucidating some of the potential applications. The third chapter describes a comparison of scattering corrected relative quantum yield measurements of coumarin dye-containing nanoparticles and free dye in aqueous solution, thereby quantifying the brightness enhancements observed upon dye encapsulation in silica. The fourth chapter reports on the incorporation of large Stokes-shift dyes into the silica matrix of the particles to allow for spectral multiplexing. Since both light scattering and autofluorescence backgrounds in biological samples tend to be stronger at shorter wavelengths, the fifth chapter focuses on the synthesis of near-infrared (NIR) fluorescent silica nanoparticles with special emphasis on the development of dye structure-optical property

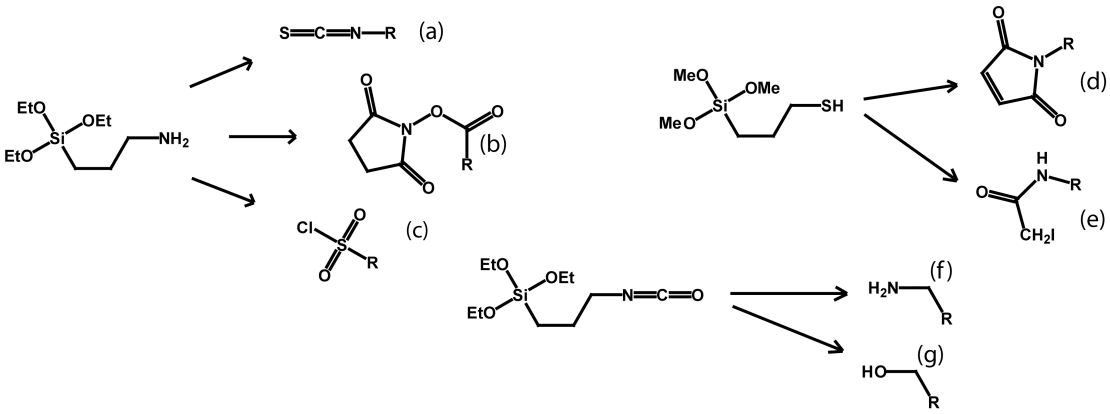


Figure 1.2: Conjugation chemistries for conjugating dye with a reactive silane precursor. 3-aminopropyltriethoxysilane has been used to incorporate dyes (denoted as R) with (a) isothiocyanate, (b) succinimidyl ester, and (c) sulfonyl chloride reactive groups. 3-mercaptopropyltrimethoxysilane has been used to incorporate dyes with (d) maleimide and (e) iodoacetamide reactive groups. 3-isocyanatopropyltriethoxysilane has been used to incorporate dyes with (f) amine and (g) hydroxyl group reactive groups.

correlations. Finally, using a self-built fluorescence correlation spectroscopy (FCS) instrument the photostability of cyanine dye (Cy5) containing NIR emitting particles was investigated and is reported on in Chapter 6. Chapter 7 concludes the dissertation with an overview of potential future work.

## REFERENCES


(1) Herschel, S. J. F. W. *Philosophical Transactions of the Royal Society of London* **1845**, *135*, 143-145.

(2) Burns, A., J. Vider, H. Ow, E. Herz, O. Penate-Medina, M. Baumgart, S. M. Larson, U. Wiesner, M. Bradbury *Nano Letters* **2009**, *9*, 442-448.

(3) Herz, E.; Burns, A.; Lee, S.; Sengupta, P.; Bonner, D.; Ow, H.; Liddell, C.; Baird, B.; Wiesner, U. *Proceedings of SPIE* **2006**, *2006*, 6096-6108.

(4) Widengren, J.; Rigler, R.; Mets, U. *Journal of Fluorescence* **1994**, *4*, 255-258.

(5) Song, L.; Hennink, E. J.; Young, I. T.; Tanke, H. J. *Biophysical Journal* **1995**, *68*, 2588-2600.

(6) Yoffe, A. D. *Advances in Physics* **2001**, *50*, 1-208.

(7) Gao, X.; Cui, Y.; Levenson, R. M.; Chung, L. W. K.; Nie, S. *Nature Biotechnology* **2004**, *22*, 969-976.

8) Kirchner, C.; Liedl, T.; Kudera, S.; Pellegrino, T.; Javier, A. M.; Gaub, H. E.; Stölzle, S.; Fertig, N.; Parak, W. J. *Nano Lett* **2005**, *5*, 331-338.

(9) Chang, E.; Thekkek, N.; Yu, W. W.; Colvin, V. L.; Drezek, R. *Small* **2006**, *2*, 1412-1417.

(10) Derfus, A. M.; Chan, W. C. W.; Bhatia, S. N. *Nano Lett* **2004**, *4*, 11-18.

(11) Mancini, M. C.; Kairdolf, B. A.; Smith, A. M.; Nie, S. *Journal of the American Chemical Society* **2008**, *130*, 10836-10837.

(12) Blaaderen, A. v.; Vrij, A. *Langmuir* **1992**, *8*, 2921-2931.

(13) Nyffenegger, R.; Quellet, C.; Ricka, J. *Journal of Colloid and Interface Science* **1993**, *159*, 150-157.

(14) Ow, H.; Larson, D. R.; Srivastava, M.; Baird, B. A.; Webb, W. W.; Wiesner, U. *Nano Lett.* **2005**, *5*, 113-117.

(15) Larson, D. R.; Ow, H.; Vishwasrao, H. D.; Heikal, A. A.; Wiesner, U.; W.W.Webb *Chemistry of Materials* **2008**, *20*, 2677.

# CHAPTER 2

# FLUORESCENT CORE-SHELL SILICA NANOPARTICLES: AN ALTERNATIVE RADIATIVE MATERIALS PLATFORM*


## *2.0 Abstract*

We report on monodisperse fluorescent core-shell silica nanoparticles (C dots) with enhanced brightness and photostability as compared to parent free dye in aqueous solution. Dots containing either tetramethylrhodamine or 7-nitrobenz-2-oxa-1,3-diazole dyes with diameters ranging from tens of nanometers to microns are discussed. The benefits of the core-shell architecture are described in terms of enhanced fluorescent yield of the fluorophores in the quasi-solid-state environment within the particle as compared with parent free dye in water. Several applications of these particles in the fields of photonics and the life sciences are discussed. Specifically, fluorescent core-shell silica nanoparticles are investigated as an active medium for photonic building blocks assembled on zinc sulfide-based seed particles. Initial assembly results for these composite raspberry structures are shown. Finally, applications in the life sciences are explored, including targeting of specific antibody receptors using these single-emission nanoparticles. We expand on single-emission core-shell architecture to incorporate environmentally-sensitive fluorophores to create quantitative ratiometric nanoscale sensors capable of interrogating chemical concentrations on the sub-cellular to molecular levels and demonstrate initial results of intracellular pH imaging. The concept of a single particle laboratory (SPL) is introduced as an active investigator of its environment.



*Originally Published as: Erik Herz[+], Andrew Burns[+], Stephanie Lee, Prabuddha Sengupta, Daniel Bonner, Hooisweng Ow, Chekesha Liddell, Barbara Baird, Ulrich Wiesner. *Fluorescent Core-Shell Silica Nanoparticles: An Alternative Radiative Materials Platform.* Proceedings Volume 6096, Colloidal Quantum Dots for Biomedical Applications, 2006. DOI:10.1117/12.661782. + these authors have contributed equally to the work described. Reproduced by permission of SPIE.

### *2.1 Introduction*

A vast number of applications, including the investigation of cell biology with fluorescence imaging, creation of active materials for display technologies, and industrial security and quality control all benefit from the use of improved photoluminescent materials. In order to maximize the potential of such materials, two key characteristics are bright and stable fluorescence. Currently, the most common materials utilized in these applications are organic fluorophores. While widely available and easy to use, dyes are often susceptible to emission fluctuation and degradation in common working environments. Factors such as heat, extended excitation, oxidation, collision with ions, changes in pH, and many other environmental factors can change the fluorescent properties of the dyes. Interactions with such dynamic environments lead to photobleaching, quenching, non-specific sticking and solvatochromic effects that can make quantitative measurements difficult. As a result of these shortcomings under challenging conditions, as well as insufficient brightness levels of individual fluorophores, a search for alternatives has been underway for several decades. Among the products of this research are new classes of emitters such as fluorescent proteins (i.e. GFP), semiconductor quantum dots and processes for encapsulation of dyes in a host of matrix materials to enhance the dyes' native properties.

In the last two decades in particular, colloidal semiconductor quantum dots (QDs) have become of great academic and technological interest for their brightness and apparent stability. In many cases, QDs have been encapsulated in polymeric or inorganic matrices to overcome their natural hydrophobicity, thereby allowing them to be used in biological media and other aqueous environments.[1] While exhibiting many desirable photophysical properties, QDs face significant challenges relating to their toxicity and disposal.[2,3]

An alternative approach to creating new emitters builds upon the strengths of organic fluorophores, namely their chemical and photophysical tunability and relative ease of functionalization for entrapment or encapsulation within a protective matrix. This concept effectively increases the robustness of the emitter by limiting degradation and protecting the fluorescent moieties. Encapsulation may add other desirable qualities such as hydrophilicity, brightness enhancement, compatibility with various substrates or polymer formulations, facile incorporation in hierarchical structures, as well as increased biocompatibility.

Among the variations on this concept, polymers[4], lipids[5], and silica[6] have all been employed as matrix materials, depending on the application's constraints and ease of synthesis with a given dye. Polymer-based particles are currently the most common, including commercially available polystyrene beads.[4] Swelling, diffusion, de-swelling[7] or entrapment during polymerization techniques are widely used to non-covalently incorporate dyes within a polymer matrix[8] creating, e.g., biocompatible particles. Though these particles can integrate multiple dye molecules to increase per-particle brightness, the polymer network often affords the dyes relatively little protection against quenching or leaching. Another approach is the use of lipid-based particles as vehicles for the dyes. These microparticles provide a highly biocompatible alternative to polymers, though they lack the robustness and small size necessary for certain biological applications.[9]

To address the issues associated with organic encapsulation of the dyes, inorganic silica matrices have been considered. In general, monodisperse colloidal silica nanoparticles may be synthesized via a sol-gel condensation process[10,11] in which alkoxysilanes are hydrolyzed and condensed in an ammonia-catalyzed reaction in alcohol solution as originally described by Stöber and coworkers in 1968.[12] Subsequent work has shown the ability to incorporate various organic compounds

homogenously into particles grown by the sol-gel method[13] including both non-covalent, reverse micelle-based[6] and covalent, modified Stöber synthesis based[14] incorporation of photoemitters. These methods all provide a robust vehicle for the dyes as well as a biocompatible and easily functionalized outer surface.

The Wiesner group has recently developed monodisperse fluorescent silica nanoparticles based on a core-shell architecture with greatly enhanced brightness and photostability compared to the parent fluorophore in solution.[15] This concept (Figure 2.1a) involves the covalent localization of the fluorescent dye molecules (e.g. tetramethylrhodamine isothiocyanate, TRITC) within an organosilica matrix, which is encased in a shell of pure silica for protection. The strength of the fluorescent core-shell silica nanoparticle platform is the ability to bind the dye in a chemically sequestered, quasi-solid state environment within the nanoparticle core, which prohibits dye leaching and decreases perturbations to the fluorescence as evinced by decreased solvatochromic shifts and increased resistance to photobleaching in comparison to dye molecules in water.[15] The protection of multiple dye molecules from the solvent environment by means of a silica shell around the core provides a way to introduce dyes into a variety of solvent environments independent of their innate behavior in those solvents. For example, many dyes have aggregation issues or low quantum yield in aqueous solutions, which may be ameliorated through encapsulation in a silica matrix.

The fluorescent core-shell modification retains the well-established synthetic versatility originally described by Stöber while expanding on the functionality and benefits of silica nanoparticles. For example, this method has advantages in comparison to reverse microemulsion techniques in that it is an easily scalable, low

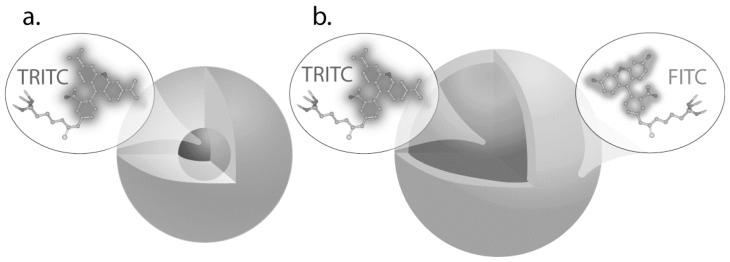


Figure 2.1: Schematic description of two fluorescent core-shell architectures employed in this study. (a) A dye-rich core encapsulated by a protective pure silica shell for labeling and photonic applications and (b) a reference dye-rich core coated by a sensor-dye rich outer shell for ratiometric chemical imaging applications.

dye-loss method that employs no surfactants. Furthermore, with the structure/property tunability afforded by controlling the encapsulated dye, particle architecture and hierarchical assemblies of particles, our work begins to explore the rich interface between materials design, photonics, and biological investigation. Here we will discuss the general premise underlying the core-shell design, photophysical properties of these particles and how encapsulation is a flexible method for designing composite particle architectures for the generation of active photonic crystal building blocks. We will then discuss several promising applications in biological imaging.

## *2.2 Methodology*

### *2.2.1 Scanning Electron Microscopy*

Scanning Electron Microscopy (SEM) is a useful technique for analyzing particle size, monodispersity and surface morphology of nanoparticles from tens of nanometers to microns in size. While it lacks the statistics of ensemble averaging measurements such as dynamic light scattering or fluorescence correlation spectroscopy, SEM allows the simultaneous visualization of the surface architecture of, e.g. composite particles, as well as giving an indication of the average size and monodispersity of a given sample. SEM analysis was carried out on particles dispersed on clean silicon wafer surfaces and imaged in a LEO 1550 Field-Effect SEM at low beam current and working voltage to minimize sample damage and achieve the desired surface resolution.

### *2.2.2 Confocal Fluorescence Microscopy*

Confocal laser-scanning Fluorescence Microscopy (CFM) provides an excellent tool for imaging the spatial and temporal distribution of fluorescence in biological and other samples. All cellular images were collected on a Leica TCX-SP2 confocal microscope with Argon (488nm line) and Helium-Neon (543nm) laser excitation using a 63x 0.9 NA water immersion objective. For the dual-emission sensor nanoparticles, sensor and reference channel images were collected using separate excitation wavelengths and emission filters to ensure spectral separation and were line-averaged to enhance clarity.

### *2.2.3 Optical Characterization*

The photophysical characteristics of the as-made nanoparticles were investigated using spectrophotometry and spectroflourometry. Absorption and emission spectra were collected with the particles or parent dye in the solvent of choice, usually spectroscopically pure water, or an appropriate buffer (as noted in the data), contained in a three milliliter quartz cuvette with a one centimeter path length. Absorption spectra were collected on a Cary 300 Bio UV/VIS dual beam spectrophotometer using one nanometer intervals across the spectrum of interest. Optical density at the absorption maximum was matched and the emission spectra measured when particles were compared to free dye. For both single- and dual-emission nanoparticles and ZnS raspberry particles, fluorescence emission spectra were collected on a PTI spectrofluorometer using an excitation wavelength that matched the peak of the absorption spectrum, again using one nanometer intervals. All single- and dual-emission nanoparticle spectra were collected from samples in solution, whereas the spectra for ZnS raspberry particles were collected from powder

samples affixed to a glass slide. In all cases, the fluorometer excitation source was a xenon lamp spectrally selected by a monochromator.

### *2.2.4 Targeting Using Single-Emission Fluorescent Core-Shell Silica Nanoparticles*

The Immunoglobulin (IgE) antibodies were adsorbed onto the particle surface using a 1:1 ratio in Tyrode's buffer (pH 7.4, 1mg/ml Bovine Serum Albumin) before incubation with the Rat Basophilic Leukemia (RBL) mast cells. Cells were exposed to the antibody-bound particles and antibody-free particles (control) for 30 minutes at 37ºC in the buffered solution at a concentration of $10^4$ particles per cell. The cells were then washed thrice by centrifugation and resuspended in Tyrode's buffer before plating on 35mm Petri dishes with coverglass bottoms (0.16-0.19mm; MatTek Corp) and imaging via confocal fluorescence microscopy as described above.

### *2.2.5 Cellular Application of Dual-Emission pH Sensor Nanoparticles*

RBL mast cells were exposed to 70nm dual-emission pH sensor particles in Tyrode's buffer (pH 7.4, 1mg/ml Bovine Serum Albumin) at a loading of $10^5$ particles per cell. Cells were incubated at 37ºC for one hour including a 20 minute incubation with phorbol (12,13) dibutyrate at a concentration of 50ng/ml. The cells were then washed thrice by centrifugation (to remove free particles) and resuspended in Tyrode's buffer before plating on 35mm Petri dishes with coverglass bottoms (0.16-0.19mm; MatTek Corp) and imaging via confocal fluorescence microscopy as described above.

### *2.3 Results and Discussion*

#### *2.3.1 Single-Emission Fluorescent Core-Shell Silica Nanoparticles*

Figure 2.1.a. shows a schematic of the single-emission fluorescent core-shell nano-particles (C dots) described in a recent publication of the Wiesner group.[15] An isothiocyanate derivative of tetramethylrhodamine (TRITC) was used to covalently bind the fluorophores in the core of the particles. The synthesis of the core-shell architecture was accomplished by the so-called Stöber process. In this first paper we described particles of a hydrodynamic radius of ~10-15nm with narrow particle size distributions (as measured by fluorescence correlation spectroscopy (FCS)). For many applications, however, it is desirable to generate particles of various sizes from the nanometer- all the way to the micron-size regime. The Stöber process, which proceeds via hydrolysis and condensation mechanisms, occurs in a homogeneous alcohol reaction medium (e.g., ethanol). It thus provides a convenient way to access various particle sizes by simply controlling the reaction conditions.[12] Figure 2.2 shows how this can be used to generate fluorescent core-shell particles of various sizes all the way up to the micron regime. The figure depicts scanning electron micrographs of particles of 50nm (a), 150nm (b), 200nm (c), 300nm (d), 550nm (e), and 1.5μm (f) in diameter. In all cases, the images suggest narrow particle size distributions as expected for the Stöber synthesis in this size regime.

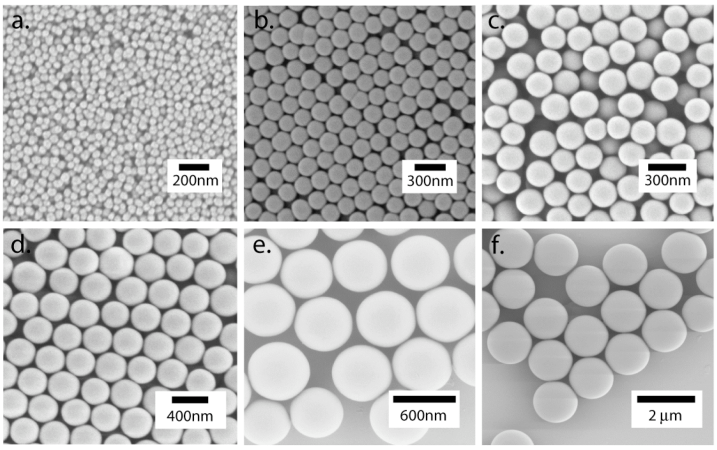


Figure 2.2: Scanning Electron Micrographs of monodisperse core-shell fluorescent silica nanoparticles synthesized in a variety of sizes ranging from tens of nanometers to microns in diameter.

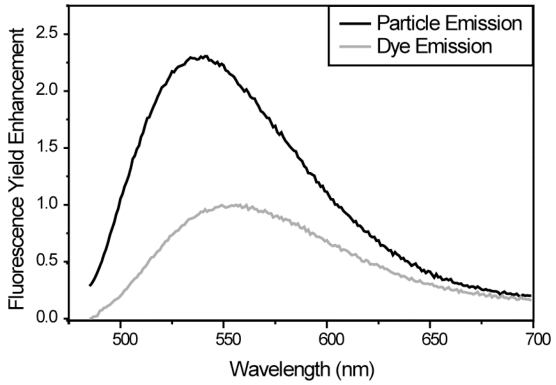


Figure 2.3: Fluorescence yield comparison for NBD-based silica nanoparticles emission compared to un-conjugated dye in water for nano-particle and dye samples of equal peak optical density. Samples were excited at their respective maximum absorption wavelengths.

In order to demonstrate how the photophysical properties of organic dyes benefit from silica encapsulation, Figure 2.3 shows fluorescence emission spectra of particles in which the tetramethylrhodamine dye (a highly optimized dye for aqueous environments) has been replaced by 7-nitrobenz-2-oxa-1,3-diazole (NBD). NBD is a yellow-emitting dye with peak absorption and emission wavelengths spectrally distinct from the rhodamine dye. Like TRITC, it is well known in the fluorescence community for labeling and imaging. NBD is further known to be a weak emitter[16] whose quantum yield may be very low (~0.01) in water.[4] In Figure 2.3 the emission of the NBD dots is compared to the emission of unconjugated NBD in water. Samples were matched to the same optical density, as described in the Methodology section. As is evident from the comparison in Figure 2.3 the emission of the encapsulated dye is significantly enhanced over that of the free dye in water. Hence, via encapsulation within a protective silica particle we can enhance the dye's behavior relative to that in aqueous solution. In addition, encapsulation within the particles separates the dye molecules from one-another, which limits energy transfer and attendant quenching, increases ease of handling (especially in the larger particle format), and allows for a much broader range of possible conjugation chemistries for biological and other applications through common organosilicate chemistry.

We would like to stress the importance of the enhanced emission of the dots compared to free parent dye in aqueous solutions. Dyes often have low quantum efficiencies in water or are highly optimized for fluorescence in biologically relevant solutions, but are then extremely expensive if at all commercially available. The results presented here and in our previous paper[15] suggest that encapsulating un-optimized organic fluorophores in a core-shell architecture might render dyes with low optical performance in water more competitive to highly optimized dyes.

### *2.3.2 Functional Assemblies for Integration into Photonic Structures and Devices*

The integration of optical devices onto a chip in a manner analogous to electronics can open the door to a new technology that can leverage and complement the strengths of conventional CMOS technology.[17,18] Highly confined photonic structures offer fundamentally novel mechanisms to control the flow of light and to concentrate it, allowing for enhanced light-matter interactions. Recent results have shown the ability to guide, filter, bend and split light on silicon chips using nano-size structures demonstrating compatibility with the microelectronics industry.[19,20,21,22] However development of active devices, such as emitters, amplifiers and modulators remain a challenge, mainly due to the low electro-optics coefficient of Si and to its indirect bandgap.

The introduction of efficient *active* light-emitting elements into 3D photonic crystals (PCs) is essential for the realization of the interesting phenomena predicted to occur in photonic band gap (PBG) materials. Ultra-small optical circuits (combining passive and active PC structures and utilizing photonic band gaps, artificially introduced defects, and light sources) are envisioned with integrated elements such as sharp-bend waveguides, wavelength selectors, nano-ampere laser arrays and optical modulators.[23]

One of the basic structures required to realize these goals is the photonic bandgap crystal, which may be created through self-assembly of monodisperse colloidal particles. Depending upon the materials employed, this assembly can be used to create structures of sufficient index of refraction contrast and appropriate period to form a depleted local photon density of states to block a particular wavelength of light in a given direction (photonic stopband).

Fluorescent dyes have great potential in the exploration of photonic bandgap interactions in optically active structures because their broad emission spectra can

easily interact with the stopband.[24] The principal challenge in realizing these benefits has been the preservation of the dye's emission characteristics during incorporation in the PC.[25] Introducing the dye into the PC requires a dye that can survive the processing steps. The end result is generally a dye adsorbed to the surface of the PC building blocks, which often leads to stacking and inhomogeneous dye distribution.[26] In addition, the dyes may be prone to photobleaching[27] and fluorescence quenching at high dye concentrations.[28] Overall, these interactions can lead to reduced fluorescence quantum yields and shortened excited state lifetimes.[29]

In order to address these shortcomings, and to overcome the issue of low refractive index contrast seen in polystyrene- and silica-based PCs,[30,31] we have recently described the synthesis of a hierarchically-structured active composite based on submicron "raspberry" building blocks with high refractive index Zinc Sulfide (ZnS) or ZnS-coated polystyrene (ZnS-PS) cores and a coating of single-emission fluorescent core-shell silica nanoparticles. The ZnS raspberry particle synthesis is designed to provide monodisperse particles with a high loading of active emitters on the surface, in this case TRITC-based single-emission core-shell silica nanoparticles. A schematic detailing the ZnS seed with a core-shell silica nanoparticle studded surface is depicted in Figure 2.4a. A representative SEM image of ~500nm diameter ZnS raspberry particles is shown in Figure 2.4b. Observation of distinct C dot nanoparticles nicely demonstrates the complete and uniform coverage of the ZnS surface. Full characterization of the particles shows that the C dots form a monolayer (~25nm) on the ZnS seed particle and that the narrow size distribution of the ZnS seed particles is preserved by the coating process (data not shown).

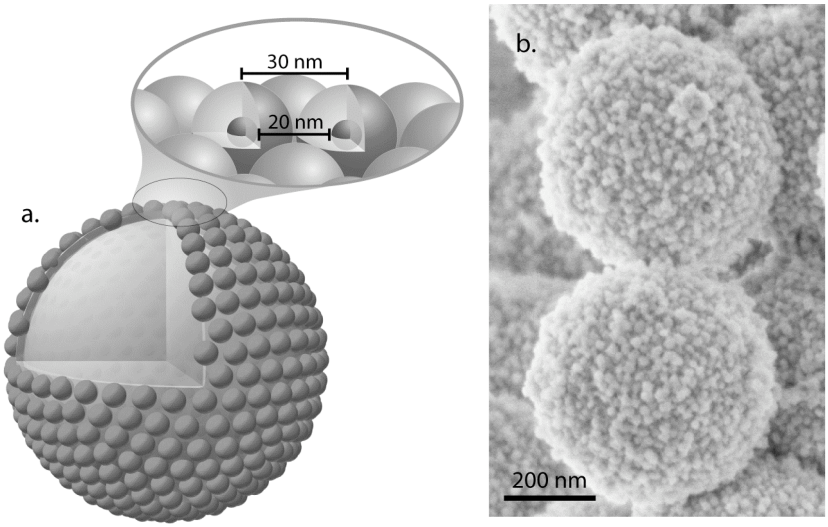


Figure 2.4: ZnS raspberries: (a) cut away schematic illustrating the ZnS seed and co-condensed ZnS/C-dot shell, with a magnified inset schematic depicting the juxtaposition of particles and particle cores on the raspberry surface, and (b) SEM image of two raspberry particles based on 445nm ZnS seed particles and 30nm fluorescent nanoparticles on the surface.

Comparison of the fluorescence emission spectra of the raspberry composite and pure silica indicates that the ZnS raspberry synthesis does not significantly affect the fluorophores protected by their silica shell (data not shown). Dye molecules adsorbed onto surfaces often assume p-p stacked arrangements known to have low fluorescence yield due to energy transfer; the silica shell, shown schematically in the enlarged area in Figure 2.4a, keeps the dye rich cores from interacting with one-another, allowing high surface dye loadings while alleviating such energy transfer. A monolayer of the core-shell nanoparticles on the ZnS seed thus allows for maximal emission intensity for this architecture. Finally, in Figure 2.5, an assembly of the ZnS-PS raspberry-type particles into larger scale structures is shown. In this fluorescence micrograph the regions of hexagonal packing demonstrate the ability to assemble the raspberry structures into 2-D periodic lattices, a prerequisite for the formation of PCs with interesting optical properties. In the future, studies of the modification of C dot emission characteristics due to changes in the local density of photon states within the PC will be performed as the assembly (crystallization) is optimized.

### *2.3.3 Applications of Fluorescent Silica Core-Shell Nanoparticles in the Life Sciences*

Many fundamental issues in experimental biology hinge on the understanding of the biomolecular and biochemical interactions and conditions at the nano- and micro-scale. Recent developments in bioinformatics, imaging and computational analysis technologies are enabling researchers to investigate this realm of antigens and antibodies, enzymes and substrates and complex phenomena at the cellular and molecular levels. Nanoparticle-based probes are beginning to play a part in these studies, creating multifunctional vehicles for imaging and analysis while maintaining

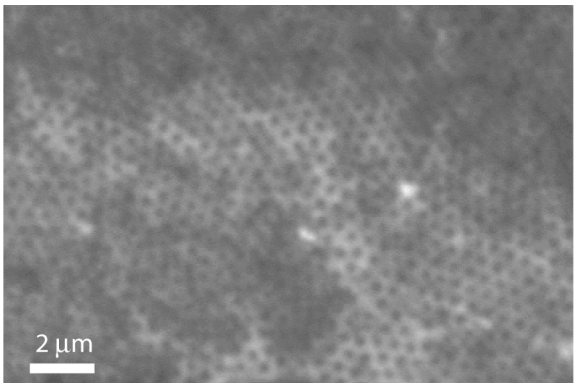


Figure 2.5: Fluorescence image of ZnS-PS raspberry particle assembly showing emission of TRITC-based single-emission core-shell silica nanoparticles

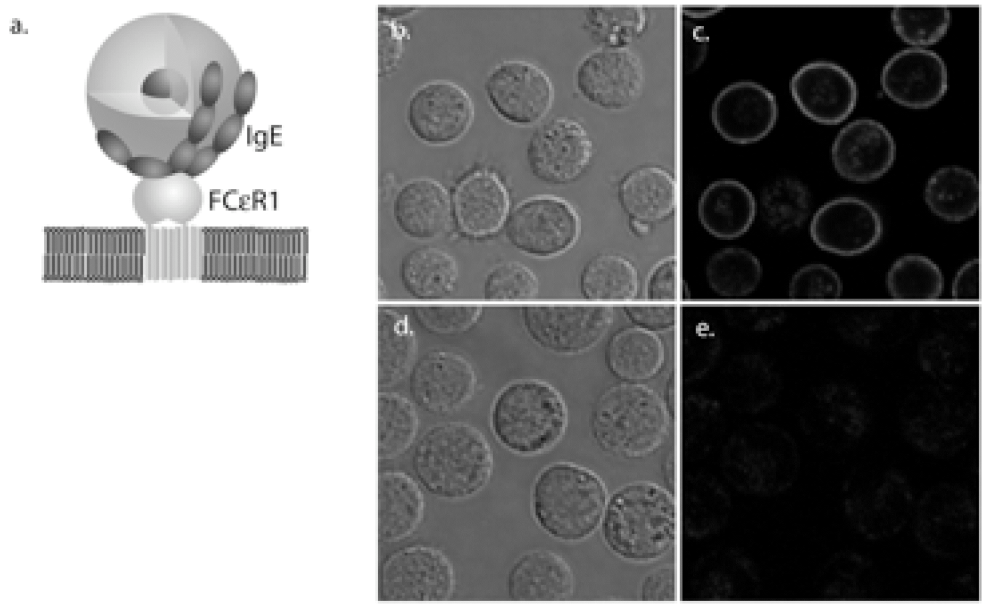


Figure 2.6: IgE-mediated targeting in RBL mast cells (a) schematic of 30nm IgE-bound silica nanoparticle at the FcεR1 cell surface receptor, (b,c) brightfield and CF images of surface-receptor labeled RBL mast cells and (d,e) BF and CF images of cells incubated with bared 30nm fluorescent nanoparticles.

sufficiently small sizes to avoid significant perturbations to the biological systems under investigation.

### *2.3.4 Targeting Using Single-Emission Fluorescent Core-Shell Silica Nanoparticles*

One major challenge in any fluorescence-based biological experiment is ensuring that the probe only labels the specific biological target of interest. Silica may be easily functionalized with a vast array of biologically active substances from small molecules to antibodies. To demonstrate the single-emission fluorescent core-shell silica particles as biological labels, we chose to pursue antibody-mediated labeling of cell surface receptors in mammalian cells, because of its conceptual generalizability across cell lines and receptors.

As a proof-of-principle for antibody-mediated targeting, we investigated the interaction between Immunoglobulin E antibodies (IgE) and the FceR1 cell surface receptor of Rat Basophilic Leukemia mast cells (RBL-2H3). RBL mast cells are blood-borne immune cells that operate in the body's allergic response. FceR1 is integral to this response and is known to form a strong, but reversible complex with IgE *in vitro*.[32] Upon exposure to an allergen, IgE antibodies specific to the allergen bind to and cross-link the cell surface receptors. This initiates a signal transduction cascade throughout the cell, ultimately leading to degranulation and release of histamine and heparin which transduce further steps in the allergic response, ultimately leading to bodily allergy symptoms.[33] In recent work, we demonstrated specific cell surface labeling towards on-going investigations into the underlying biochemical pathways in allergic response.[15]

Following incubation with cells, the particles bound to the IgE antibody are attached to the cell surface via the IgE-FceR1 interaction, which is diagrammed in

Figure 2.6a. The effectiveness of this interaction is shown in the confocal and bright field images in Figure 2.6b-c, which depict equatorial CFM and brightfield images of the nanoparticles bound to live cells and show even labeling levels across the whole cell membrane. As a control, nanoparticles without antibody were incubated under the same conditions and showed no appreciable binding to the cell surface after washing as shown in the CFM and bright field images in Figure 2.6d-e. The combination of specific targeting and the robust nature of these core-shell fluorescent silica nanoparticles creates an ideal tool for long-term studies such as determining the fate of antibodies or other proteins in a variety of biological systems.

### *2.3.5 Dual-Emission Fluorescent Core-Shell Silica Nanoparticles for Sensing Applications*

In addition to simply labeling particular locales in the cellular milieu, many biological phenomena depend heavily on chemical gradients, which exist within and around cells. Regulation of the concentration of ions such as $Na^{+}$, $Ca^{+2}$ and $H^{+}$ are integral to cellular biochemistry and changes in these concentrations can be indicative, e.g. of signal transduction and overall cellular health. For example, within eukaryotic cells, materials (e.g. drugs, proteins) that are endocytosed by the cell are transported through a series of membrane-bound organelles known as endosomes which sequentially lower pH until reaching the lysosome which ultimately degrades the foreign material, unless it undergoes trafficking to other locales in the cell.[34] On an extracellular scale, e.g. the rampant growth of tumor cells quickly outstrips the blood supply, creating an acidic and hypoxic environment within the growing tumor.[35] Thus, the ability to quantitatively image the concentrations of biologically active ions, such as $H^{+}$ is of major importance for both *in vitro* and *in vivo* experiments.

To this end, the archetypal single-emission fluorescent core-shell silica nanoparticle architecture shown in Figure 2.1a can be expanded to develop a class of dual-emission core-shell ratiometric sensor nanoparticles schematically shown in Figure 2.1b. Using the core dyes as an internal reference against which sensor dyes in the periphery of the particle may be compared facilitates quantitative chemical sensing and imaging in an optimized architecture down to the single particle level. By localizing the reference dye deep within the particle core, it is effectively sequestered from environmental fluctuations that could compromise its stability. Covalently bound sensor dyes in the outermost shell are exposed to the highest available surface area for interaction with analytes in solution while still afforded some of the protection of the surrounding silica matrix. This provides greater sensitivity and more uniform response than particles with sensor and reference dye molecules dispersed homogenously throughout the particle.

As proof-of-principle for the dual-emission core-shell sensor nanoparticle architecture, we have recently developed a ratiometric pH sensor for quantitative *in vitro* chemical imaging and spectrofluorometric analysis.[36] Fluorescein was chosen as a pH sensor dye because it exhibits a significant change in quantum yield depending upon the protonation state of the hydroxyl groups on the π-conjugated xanthene backbone of the dye. In the protonated, mono-anionic form, the dye exhibits the relatively low quantum yield of 36%, whereas upon deprotonation the quantum yield increases to 93% for the dianion form.[4] The pKa of this transition is 6.4, which places fluorescein's pH sensitivity in the biologically relevant range from pH 5-8.5. Tetramethylrhodamine (TRITC) was chosen as an internal standard for its stability against fluctuations in pH, relative brightness and spectral separation from fluorescein. Figure 2.7a shows an SEM image of the 50nm tetramethylrhodamine (TRITC)-rich core particles, which serve as an internal reference to the fluorescein (FITC) bound in

a 10nm shell on these cores. A representative SEM image of the resulting 70nm core-shell particles is shown in Figure 2.7b. In both cases, smooth and uniform, monodisperse particles were produced. Particle size and architecture were chosen for ease of uptake into cells[37] as well as ease of handling during synthesis and characterization.

The pH sensitivity was calibrated by spectrofluorometry of particles suspended in sodium phosphate buffers between pH 5 and pH 8.5. The fluorescein and tetramethylrhodamine emission spectra were collected for each solution and the peak emission intensities for each pH were analyzed to determine the fluorescence ratio between the two intensities. In order to account for particle concentration fluctuations in real samples, the ratio between peak emission intensities was determined by dividing the peak sensor intensity by the peak reference intensity, to create a ratiometric calibration curve as shown in Figure 2.8. This calibration curve exhibits the typical behavior of a system in equilibrium between two states, in this case the mono- and di-anionic states of fluorescein and shows an effective pKa at pH 6.4 which corroborates well with the literature value.[4] Similarly, confocal microscopy images of both sensor and reference channels were taken on nanoparticle suspensions across the pH range from 5-8.5 and analysis via MATLAB generated a second ratiometric calibration curve for imaging applications (data not shown).

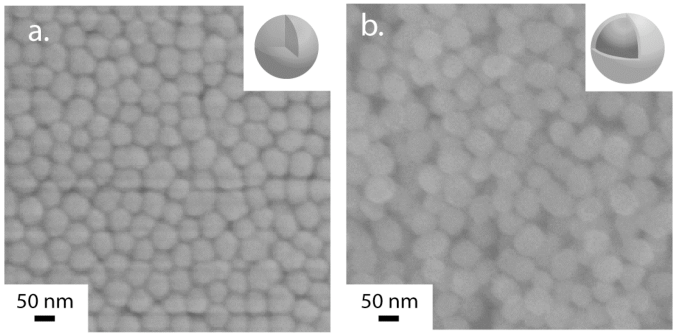


Figure 2.7: Scanning electron micrographs and schematics (insets) of (a) TRITC-based 50nm core particles and (b) 70nm dual-emission core-shell pH sensor particles incorporating FITC in the outer shell.

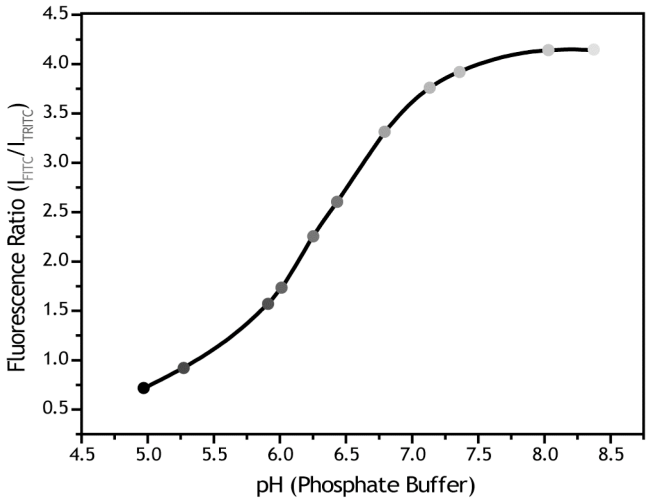


Figure 2.8: Calibration curve of the sensor/reference peak intensity ratio across pH 5-8.5 for the dual-emission core-shell fluorescent sensor nanoparticles.

In addition to measuring pH in solution, an important goal of these nanoparticle sensors was the ability to perform quantitative chemical measurements inside individual cells towards spatial and temporal mapping of proton concentrations within the cell. In order to demonstrate quantitative intracellular imaging, we again chose to use RBL mast cells as a model system for their particle-uptake characteristics. The cells were found to readily and effectively uptake the sensor particles upon incubation with phorbol (12,13) dibutyrate (PDB), a reagent commonly used in DNA transfection which is proposed to mediate macropinocytotic uptake of membrane-associated and extracellular material.[38] Upon endocytosis, the particles were taken into so-called early endosomes, which act to sort incoming material to various intracellular destinations. In the case of the sensor nanoparticles, the early endosomes matured into late endosomes and eventually lysosomal compartments with concomitant decreases in pH. The particles were imaged via CFM as shown in Figure 2.9 using separate excitation wavelengths and emission channels for reference and sensor dyes. The reference dye (TRITC) channel (Figure 2.9a) acts not only as an internal standard for pH measurements but also as a stable indication of particle location and local concentration allowing the particles to be tracked through the cell. Based on the sensor dye (FITC) channel (Figure 2.9b) and the previously determined calibration curve, the pH at various locations within any particular confocal image plane can be determined from the pixel-wise ratio between sensor and reference dyes as represented by the false-spectrum image overlaid on a bright field image of the cell in Figure 2.9c. Various intracellular locations are found to have pH values varying from ~pH 6.5 (early endosome) to late endosomal and lysosomal compartments with much lower pH values between 5-5.5. These experiments demonstrate the applicability of the concept of dual-emission core-shell silica sensor nanoparticles

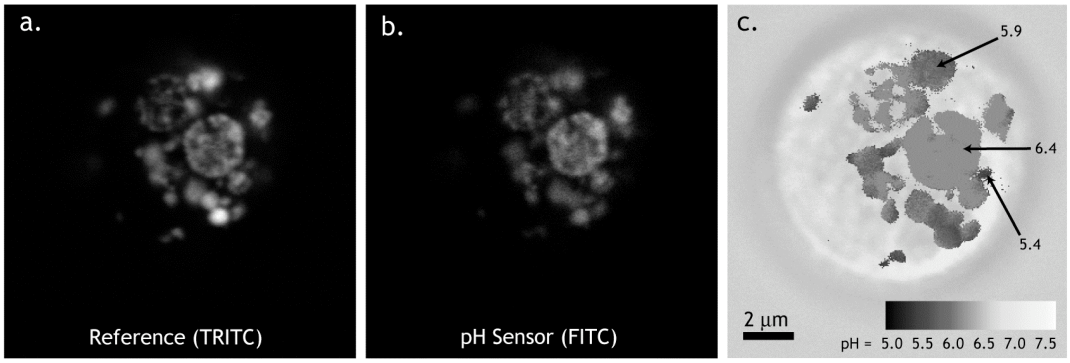


Figure 2.9: Ratiometric chemical imaging of pH within intracellular vesicles in RBL mast cells. Confocal Fluorescence microscopuy images of (a) sensor (FITC) dye fluorescence, (b) reference (TRITC) dye fluorescence, and (c) calibrated ratiometric chemical imaging of proton concentration overlaid on brightfield cell image.

for investigating fundamental biology and open the door to further experiments, which build upon the specific targeting capabilities of these nanoparticles to investigate biological phenomena.

The dual-emission sensor nanoparticles we have developed facilitate quantitative chemical imaging as a tool enabling biologists and pharmaceutical developers to determine the local chemical effects of biochemical stimuli with high spatial and temporal resolution. This architecture creates bright probes which co-localize sensor and reference dyes allowing high throughput, high content imaging for diagnostics and pharmaceutical development. Furthermore, our initial results of intracellular imaging in mammalian cells open the door to developing so-called Single Particle Laboratories (SPL).[36] This unique concept incorporates reference and sensor dyes as well as catalytic or enzymatic sites in hierarchically structured particles to create highly functional materials, which interact with and respond to their environment for a wide range of applications.

### *2.4 Conclusions*

In this paper we have described a novel radiative materials platform based on fluorescent core-shell silica nanoparticles with organic fluorophores covalently attached in a silica-based core surrounded by a silica shell. This architecture leads to enhanced brightness and photostability as compared to the parent free dye in solution. We have shown that the enhanced brightness is in part due to an increase in fluorescence yield of the dyes in the quasi-solid-state environment of the core relative to its behavior in aqueous solution. Since this effect may be generalizable to many different fluorophores with un-optimized fluorescence behavior in water, these studies open up a huge arena for the investigation of alternatives to high end fluorophores for

fluorescent probe studies. With investigations of the behavior of raspberry composite structure particles and their assemblies we have made first steps towards the generation of active photonic crystal-type materials. In these structures, the core-shell silica architecture of the active dots on the ZnS seed leads to inhibition of energy transfer between fluorophores in neighboring dots as a result of the silica shell around the dye rich core separating adjacent emitters by more than the Förster radius. This results in high brightness levels even for dense C-dot particle packing and thus constitutes an interesting design concept for active photonic materials. Finally, we have demonstrated the utility of this fluorescent core-shell silica nanoparticle platform for biological labeling and sensing. In particular, building on the bright and stable core-shell design, we created a dual-emission ratiometric sensor architecture by incorporating environmentally-sensitive dyes in the outer shell. This yields particles with optimized architecture for quantitative sensing down to the single particle level. This sensor architecture may be of particular importance in complex biological environments where many species can potentially interfere with sensing. Since many fluorphores with sensing capabilities are available, this approach may be generalizable towards multiple analytes, including metal ions, oxygen, or redox status indicators. Cocktails of such particles may further allow high content imaging for high throughput drug screening whereby metabolic parameters of cells are monitored with high temporal and spatial resolution down to the molecular level. The results presented in this article point towards the utility of multifunctional, fluorescent core-shell silica nanoparticles as single particle laboratories (SPLs) which may enable rapid imaging, screening, conversion and sensing of specific moieties in various environments.

### *2.5 Acknowledgements*

The authors would like to thank the Cornell Center for Materials Research (CCMR) and the Cornell Nano-biotechnology Center (NBTC) for funding and facilities. This material is based upon work supported in part by the STC Program of the National Science Foundation under Agreement No. ECS-9876771 and through the NSF Grant DMR 0520404, part of the NSF MRSEC Program as well as NSF NIRT grant 0404195.

## REFERENCES


[1] D. Gerion, F. Pinaud, S. C. Williams, W. J. Parak, D. Zanchet, S. Weiss, A.P.Alivisatos, *Journal of Physical Chemistry* B, **2001**, *105* (37) 8861-71

[2] C. Kirchner, T. Liedl, S. Kudera, T. Pellegrino, A. Munñoz Javier, H. E. Gaub, S. Stölzle, N. Fertig, W. J. Parak, *Nano Letters*, **2005**, *5* (2), 331

[3] A.M. Derfus, W. C. W. Chan, and S. N. Bhatia, *Nano Letters*, **2004**, 4 (1), 11-18

[4] R. P. Haugland, *The Handbook – A Guide to Fluorescent Probes and Labeling Technologies, Tenth Edition*, Molecular Probes, **2005**, Eugene, OR

[5] B.D. Kim, K. Na, H. K. Choi. *European Journal of Pharmaceutical Sciences*, **2005**, *24*, 199-205

[6] X. Zhao, R. Bagwe, W. Tan. *Advanced Materials,* **2004**, *16(2),* 173-176

[7] H. Zhu and M. J. McShane, Journal of the American Chemical Society, **2005**, *127*(39), 13448-13449

[8] R.S. Jardine, P. Bartlett, Colloids and Surfaces A: Physicochem. Eng. Aspect, **2002**, 211, 127-132

[9] A. Ma, Z. Rosenzweig, *Anal. Bioanal. Chem.*, **2005**, *382*, 28-36

[10] C. J. Brinker and G.W. Scherer, *Sol-Gel Science: The Physics and Chemistry of Sol-Gel Processing*, Harcourt Brace Jovanovich, **1990**, Boston.

[11] H. Bergna, Ed. *The Colloidal Chemistry of Silica*, American Chemical Society, **1994,** Washington, DC.

[12] W. Stöber, A. Fink, E. Bohn, *Journal of Colloid Interface Science*, **1968**, *26*, 62

[13] A. van Blaaderen, A. Vrij, *Journal of Colloid and Interface Science*, **1993**, *156*, 1-18

[14] A. Imhof, M. Megens, J.J. Engelberts, D.T.N. de Lang, R. Sprk, W.L. Vos, *Journal of Physical Chemistry B*, **1999**, *103*, 1408-1415

[15] H. Ow, D. R. Larson, M. Srivastava, B. A. Baird, W. Webb, U. Wiesner, *Nano Letters*, **2005**, *5*,113-117

[16] B. Maliwal, J. Malicka, I.Gryczynski, Z. Gryczynski, J. Lakowicz, *Biopolymers* **2003,** *70* (4), 585-594

[17] R. C. Johnson, "Intel reveals long-term goals for silicon photonics, sensors," *EE Times,* February 28, 2002

[18] L.C. Kimerling, *The Electrochemical Society Interface*, Summer 2000, 28-31

[19] K. K. Lee, D. R. Lim, L. C. Kimerling, J. Shin, F. Cerrina, *Optics Letters,* **2001,** *26*, 1888-1890

[20] A. Liu, R. Jones, L. Liao, D. Samara-Rubio, D. Rubin, O. Cohen, R. Nicolaescu, M. Paniccia, Nature, **2004**, *427*, 615-618

[21] V. R. Almeida, C. A. Barrios, R. R. Panepucci, M. Lipson, M. A. Foster, D. G. Quzounov, A. L. Gaeta, Optics Letters, **2004**, *29*, 2867-2869

[22] V. R. Almeida, C. A. Barrios, R. R. Panepucci, M. Lipson, Nature, **2004**, *431*, 1081-1084

[23] S. Noda, M. Imada, M. Okano, S. Ogawa, M. Mochizuki, A. Chutinan, *IEEE J. Quant. Electron,* **2002**, *38*, 726-735

[24] (a) M. Megens, J.E.G.J. Wijnhoven, A. Lagendijk, W. L. Vos, *Phys. Rev. A: At. Mol. Opt. Phys.* **1999,** *59,* 4727-4731.

(b) S.G. Romanov, T. Maka, C.M. Sotomayor Torres, M. Muller, R. Zentel, *J. Lightwave Technol.* **1999,** *17,* 2121-2127

[25] (a) Y.A. Vlasov, N. Yao, D. J. Norris, *Adv. Mater.* **1999,** *11,* 165-169

(b) A.L. Rogach, D. Nagesha, J.W. Ostrander, M. Giersig, N. A. Kotov, *Chem. Mater.* **2000,** *12,* 2676-2685

[26] H.P. Schriemer, H.M. van Driel, A.F. Koenderink, W.L. Vos *Phys. Rev. A: At. Mol. Opt. Phys.* **2000,** *63,* 011801

[27] I.S. Nikolaev, P. Lodahl, W.L. Vos *Phys. Rev. A: At. Mol. Opt. Phys.* **2005,** *71,* 053813

[28] T. Maka, S.G. Romanov, M. Muller, R. Zentel, C.M. Sotomayor Torres, *Phys. Stat. Sol.* **1999,** *215,* 307-312

[29] S.V. Gaponenko, V.N. Bogomolov, E.P. Petrov, A.M. Kapitonov, D.A. Yarotsky, I.I. Kalosha, A.A. Eychmueller, A.L. Rogach, J. McGilp, U. Woggon, F. Gindele, *J. Lightwave Technol.* **1999,** *17,* 2128-2137.

[30] T. Yamasaki, T. Tsutsui, *Appl. Phys. Lett.* **1998,** *72,* 1957-1959

[31] S.G. Romanov, T. Maka, C.M Sotomayor Torres, M. Muller, R. Zentel, *Appl. Phys. Lett.* **1999,** *75,* 1057-1059

[32] P. Schwille, U. Haupts, S. Maiti, W. W. Webb, *Biophysical Journal,* **1999**, *77*, 2251.

[33] J. Rivera, C. Gonzalez-Espinosa, M. Kovarova, V. Parravicini. *ACI International*, **2002,** *14(1)*, 25–36

[34] H. Lodish, ed. *Molecular Cell Biology,* ($4^{th}$ ed.), **1999**, W.H. Freeman, New York

[35] P. Carmeliet, R. Jain, *Nature*, **2000**, *407*, 249-257

[36] A. Burns, P. Sengupta, T. Zedayko, B. Baird, U. Wiesner. *Small,* **2006**, *2*, (in press)

[37] W. Zauner, N. Farrow, A. Haines, *Journal of Controlled Release,* **2001**, *71*, 39-51

[38] C. Ra, K. Furuichi, J. Riviera, J. Mullins, C. Isersky, K. White, *European Journal of Immunology*, **1989**, *19*, 1771-1777

# CHAPTER 3

# RELATIVE QUANTUM YIELD MEASUREMENTS OF COUMARIN ENCAPSULATED IN CORE-SHELL SILICA NANOPARTICLES[*]

## 3.0 Abstract

Fluorescent silica nanoparticles encapsulating organic fluorophores provide an attractive materials platform for a wide array of applications where high fluorescent brightness is required. We describe a class of fluorescent silica nanoparticles with a core-shell architecture and narrow particle size distribution, having a diameter of less than 20 nm and covalently incorporating a blue-emitting coumarin dye. A quantitative comparison of the scattering corrected relative quantum yield of the particles to free dye in water yields a relative quantum yield enhancement of about an order of magnitude. This enhancement of quantum efficiency is consistent with previous work on rhodamine dye-based particles. It provides support for the argument that improved brightness over free dye in aqueous solution is a more general effect of covalent incorporation of fluorescent organic dyes within rigid silica nanoparticle matrices. These results indicate a synthetic route towards highly fluorescent silica nanoparticles that produces excellent probes for imaging, security, and sensing applications.

[*] Accepted for publication in the *Journal of Fluorescence*.

## 3.1 Introduction

Since the discovery of fluorescence in quinine sulfate solution over 160 years ago, the use and study of fluorescence as a tool for imaging, sensing, and security applications has led to a wide array of probes used to track, tag, sense, and separate [1]. All of these applications benefit from brighter, more stable, and environmentally robust fluorescent probes and much research has been devoted to this challenge. The most commonly used probes are fluorescent dyes, quantum dots, and fluorescent particles, each with their own advantages and disadvantages [2].

Organic fluorescent dyes come in a multitude of absorption and emission wavelengths, are extremely small (even on the molecular biology scale), and many have been refined and specialized to operate in specific environments with the highest possible brightness. Unfortunately, many potential applications subject these dyes to harsh environments, including acidic or basic extremes, enzymatic activity, and interactions with ions [3, 4]. These environments may quench the dye's emission through chemical interactions with its structure or cause aggregation or self-quenching that is due to insolubility of the dye [3]. Colloidal semiconductor quantum dots are a relatively new class of very bright, quantum-confined inorganic materials that have garnered significant attention as nanoscale fluorescent probes. They have several advantages over dyes, including narrow emission, broad short-wavelength excitation, and highly tunable size dependent emission wavelength [5]. However, their production, use, and disposal present a challenge to the scientific community because of their heavy metal content [6, 7]. Finally, hybrid fluorescent particles, which incorporate fluorophores within a polymeric or inorganic matrix, are another class of probes that endeavor to combine the best properties of the dyes with those of the matrix [4, 8-10]. Through incorporation into a matrix material, a fluorescent dye can be protected from the surrounding environment and in turn protect the environment

from any toxicity, to create benign probes [11, 12]. The homogeneous entrapment of dyes within a matrix has been accomplished in several ways, but may lead to particles with some dyes that are not well protected and will interact with or leach into the surrounding environment [13].

The Wiesner group has recently developed a class of core-shell silica nanoparticles, referred to as C dots [2, 14-18]. The particle synthesis approach, using a modified Stöber technique, provides a materials platform with a number of advantages over existing fluorescent probes including: (i) defined placement of covalently bound fluorescent dyes that do not leach, (ii) small particle sizes and size distributions, (iii) control over particle architecture and color, and (iv) enhanced brightness and photostability as compared to the parent dye in water [2, 14-18]. Here we describe the synthesis of coumarin dye containing C dots and investigate the per-dye enhanced fluorescent properties, over free dye in aqueous solution, by means of relative quantum yield analysis. One effect that has not been accounted for in previous C dot work is the contribution of scattering. To this end, for the present study we chose a blue absorbing and emitting coumarin dye, for which scattering effects should be at a maximum, and covalently encapsulated it within a core-shell silica particle. Quantum efficiency enhancements were assessed using scattering corrected relative quantum yield measurements.

Relative quantum yield is a reproducible measure of a fluorescent probe's efficiency in converting absorbed photons to emitted photons relative to a reference standard of known quantum yield and was chosen for this study for its spectral flexibility [19]. The standard acts to calibrate the instrumentation and methods used to measure the absorption and integrated emission of all samples, input that is then used to calculate the relative quantum yield. The relative quantum yield also provides a

means to compare fluorescent probes of different composition and type to each other using one of the most important measures of performance, the efficiency of emission.

### 3.2 Experimental Section

Fluorescent core-shell silica nanoparticles for this work were produced by a three-step synthesis illustrated in Figure 3.1a–c, based on modifications to the Stöber method for producing pure silica particles [20]. First, a 2 mL solution of 7-diethylaminocoumarin-3-carboxylic acid, succinimidyl ester (DEAC, 4.5 mM in dimethylformamide, Anaspec) is conjugated to 3-aminopropyltriethoxysilane (APTS, 0.45 mmol, Gelest) while stirring in a nitrogen atmosphere glove box for 12 h. The resulting conjugate is removed from the glove box, added to a 500 mL stirring mixture of ethanol, water, and ammonia (2.0 M in ethanol, Sigma-Aldrich) in a 7.43 : 0.4275 : 0.1 mole ratio and allowed to equilibrate. Immediately thereafter, 0.025 mol tetraethylorthosilicate (TEOS, Sigma-Aldrich, Inc.) is added and allowed to co-condense with the conjugated dye for 12 h to produce a dye-rich core. Finally, pure TEOS is added stepwise to synthesize the pure silica shell of desired thickness that protects the core and dyes within it. The TEOS is added slowly in order to avoid secondary nucleation [21]. After synthesis, particles are stored in darkness in the reaction solution until needed, and in this way are both chemically and colloidally stable for at least 6 months.

In order to properly compare the relative quantum yield of a dye encapsulated in the C dots versus free dye, a scattering correction was performed. To this end, same-sized blank core-shell silica particles containing no dye were produced by removing the dye and the conjugation step from the synthesis procedure described above and adding the APTS directly to the particle core synthesis (Figure 3.1b).

Because of their small size, purification of all particles was accomplished by dialysis into 18.2 MΩ/cm deionized water (deionized by a Millipore Synthesis system), using 3500 MWCO dialysis tubing (Snakeskin, Pierce). Particles were dialyzed (1:500) for 8–12 h and subsequently filtered through a 0.2 μm pore size syringe filter. After purification, the physical attributes of the freshly dialyzed particles were characterized using dynamic light scattering and scanning electron microscopy (SEM, LEO 1550 FE-SEM). Dynamic light scattering (DLS, Malvern Zetasizer Nano ZS) provides the hydrodynamic particle size and particle size distribution while SEM allows for the real space observation of size and shape. SEM was performed on a single crystal silicon wafer substrate upon which the particles were deposited from a dilute ethanol solution of water-dialyzed particles to speed drying of the deposited sample.

After investigating the physical particle attributes, fluorescence and absorption measurements on the particles, constituent dye, and a standard dye were performed in preparation for relative quantum yield calculations. The spectrophotometer (Varian Cary 5E) was calibrated by checking the baseline, performing a spectral position check (using a holmium oxide standard SRM 2034), and finally by checking the photometric response (using an SRM 930D NIST transmittance standard glass filter, nominal 20% transmittance, 0.7045 absorbance at 546 nm). The spectrofluorometer (Jobin Yvon Spex Fluorolog Tau 3) was calibrated using the Raman peak of water at 397 nm when excited at 350 nm. All calibrations for the equipment used were performed daily and logs thereof retained. For the spectrophotometer, a solution of blank particles was used as a reference standard to correct for the aforementioned difference in scattering between free dye and particles in aqueous solution. The correction was achieved by matching the scattering intensity of the blank and dye-containing particles at short wavelengths and subsequent spectral subtraction. For the

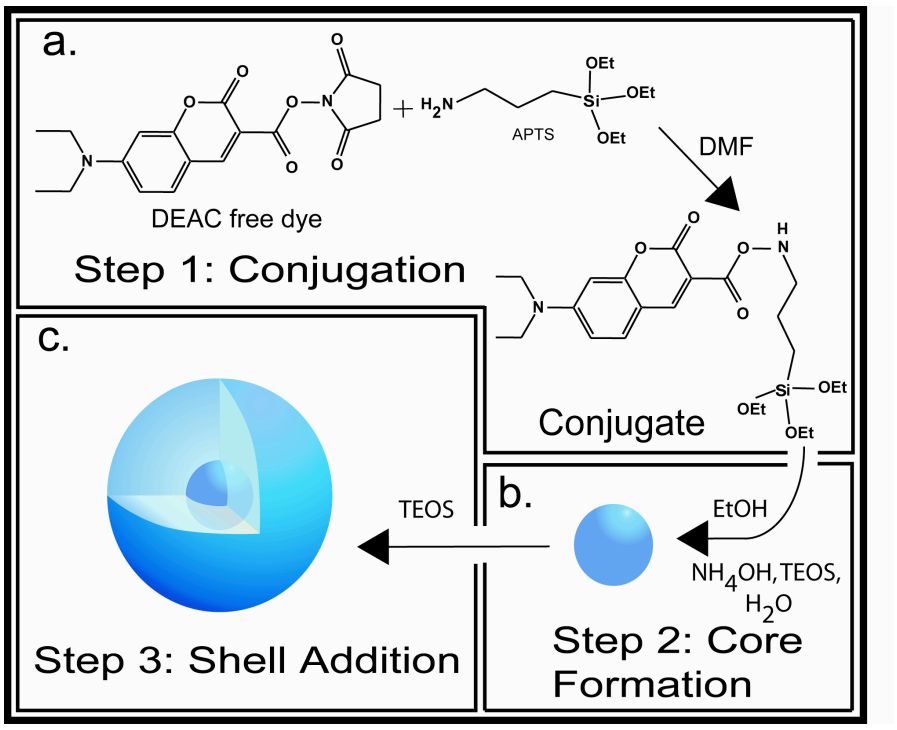


Figure 3.1: Core-shell fluorescent silica nanoparticle synthesis: (a.) Conjugation of 7-diethylaminocoumarin-3-carboxylic acid, succinimidyl ester (DEAC) dye with 3-aminopropyltriethoxysilane (APTS) to form the dye-silicate precursor; (b.) Core formation using tetraethoxysilane (TEOS) and the conjugate in basic ethanol and water solution; (c.) Addition of pure TEOS to form a protective shell.

spectrofluorometer, all emission spectra were corrected using a standard lamp with a NIST traceable calibration.

After calibrating the instruments, samples of DEAC-based fluorescent nanoparticles and the free dye were diluted with water to an absorption-matched molar concentration of between $10^{-6}$ and $10^{-7}$ moles/L of dye molecules (whether free in solution or encapsulated within the particles). The NIST referenced standard dye, quinine sulfate dihydrate in 1N $H_2SO_4$, was selected for its spectral overlap with DEAC and its good quantum yield of 0.546 [22]. The standard was freshly prepared. Each sample was placed in a 10 cm path length optical glass cell for spectrophotometry measurements. An aliquot of the spectrophotometry sample was then taken for fluorometry measurements in a 1cm path length quartz cell. Both measurements were performed thrice on each sample to ensure repeatability and minimize effects of local temperature fluctuations on absorption measurements.

For the calculation of relative quantum yield, from scattering corrected spectra, the following equation was used [19]:

$$\phi_s = \phi_{st} \frac{A_{st}}{A_s} \frac{F_s}{F_{st}} \left( \frac{n_s}{n_{st}} \right)^2 \qquad (1)$$

The ratio of the quinine sulfate reference standard absorption ($A_{st}$) to the absorption of the sample ($A_s$), at 380 nm, was found first and multiplied by the quantum yield [22] of the quinine sulfate solution ($\phi_{st}$) as well as the squared ratio of the sample refractive index ($n_s$) corrected to be that of water, 1.33, and the reference standard refractive index ($n_{st}$), 1.34 [23]. This product was then multiplied by the ratio of the integrated area under the emission spectrum (from 395 to 750 nm) of the sample ($F_s$) to that of the standard ($F_{st}$) to find the relative quantum yield of the particles and free dye. Note that the excitation wavelength of 380nm was used as it provides the spectral

position of maximum overlap of the absorption spectra of the quinine sulfate reference and DEAC dyes.

### 3.3 Results and Discussion

The synthesis reaction conditions reproducibly yielded sub 20 nm particles. Dynamic light scattering results indicate that the DEAC-based particles and the blank silica particles are both approximately 18 nm in diameter based on number statistics (see Figure 3.2a). A representative SEM image of the DEAC-based particles is shown in Figure 3.2b, corroborating the DLS results on size and demonstrating the narrow particle size distribution. From spectrophotometry and spectrofluorometry the absorption and fluorescence spectra of the particles were collected in water. Representative plots of normalized and corrected fluorescence and absorption spectra are shown in Figure 3.3a for the particles in water. Figure 3.3b depicts fluorescence as a function of absorption at 380 nm for a series of dye and particle samples. From this plot it is evident that the particles are significantly brighter than the free dye. The linear fits of the data include the zero fluorescence at zero absorption point. The quality of the fits implies that no reabsorption of fluorescence is occurring.

From the data in Figure 3.3b and use of equation (1), the relative quantum yield, $\phi_s$, for the particles is 0.178 (±0.0178) while that for the dye is only 0.02 (±0.002) [24]. The results demonstrate an approximately ten-fold increase in quantum yield achieved by covalently encapsulating the dye within a core-shell silica nanoparticle. To the best of our knowledge this is the largest enhancement reported to date for a fluorophore encapsulated in a sub 20 nm silica nanoparticle. In order to rule out conjugation effects on the enhancement, a sample of DEAC was conjugated to 4-amino-1-butanol through the succinimidyl ester reactive moiety on the dye and compared to free dye by absorption matching aqueous solutions at 380 nm and then

comparing the emission. The results are shown in Figure 3.4 and indicate that, if anything, the free dye is brighter than the conjugated one. Hence, the silica matrix of the nanoparticles clearly allows for more efficient light emission from encapsulated DEAC dye molecules relative to free dye in solution, a finding consistent with our previous work on other dye families [16, 17]. For a rhodamine-based C dot we found that the covalent encapsulation of multiple dye molecules lead to 30 nm particles close to 30 times brighter than the single dye molecule in water [17]. This brightness enhancement over free dye could be accounted for by the product of the per-dye quantum efficiency enhancement and the number of dyes per particle. Small changes in the internal architecture of the C dots were found to enhance the quantum efficiency up to three-fold on a per-dye basis, with no observable energy transfer between dyes for up to about 10 dyes per 5 nm core in a 30nm diameter particle. The quantum efficiency increase was due to a uniform two-fold enhancement in the radiative rate and a reduction in the nonradiative rate, which was found to vary inversely with the degree of rotational mobility the dye experienced within the silica particle matrix. These results taken together with the current work provide strong support for the argument that silica, with a glass transition temperature about an order of magnitude above that of organic polymers, is an especially well-suited matrix for dye-encapsulation because it provides a particularly rigid local environment that enhances dye performance.

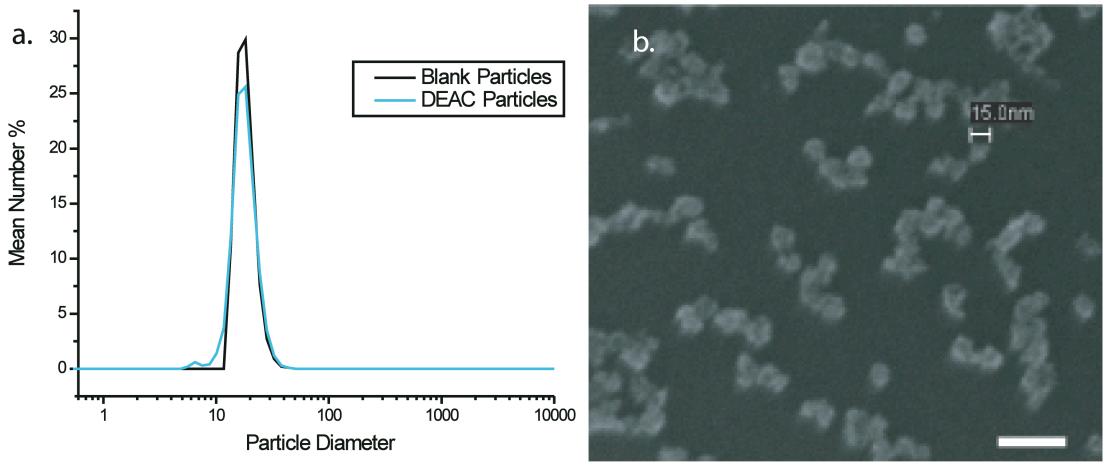


Figure 3.2: (a.) Results of dynamic light scattering measurements of blank silica and DEAC-containing silica particles used in this study. (b.) Representative scanning electron microscopy image of DEAC-containing core-shell particles (scale bar = 50 nm), corroborating DLS results.

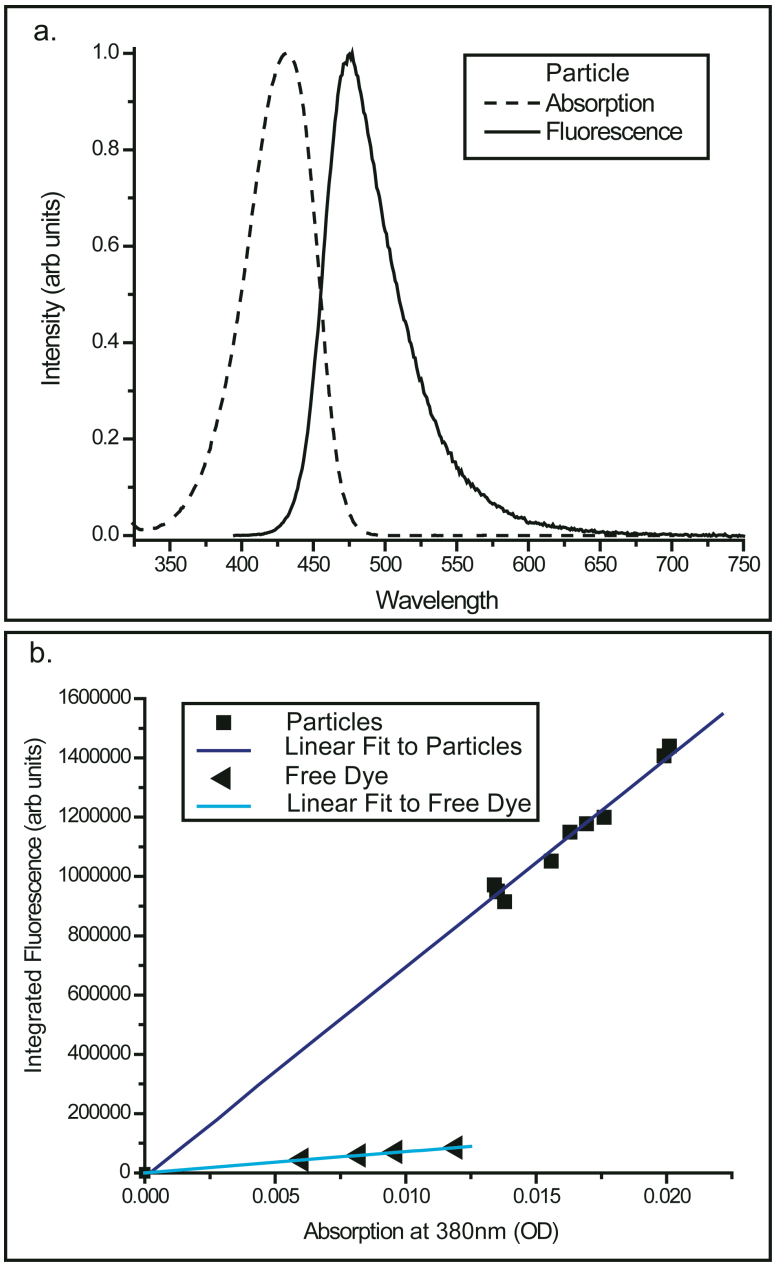


Figure 3.3: (a.) Normalized and scattering corrected absorption and normalized fluorescence for DEAC containing core-shell silica nanoparticles in water; (b.) Integrated fluorescence as a function of absorption at 380 nm for particles and free dye.

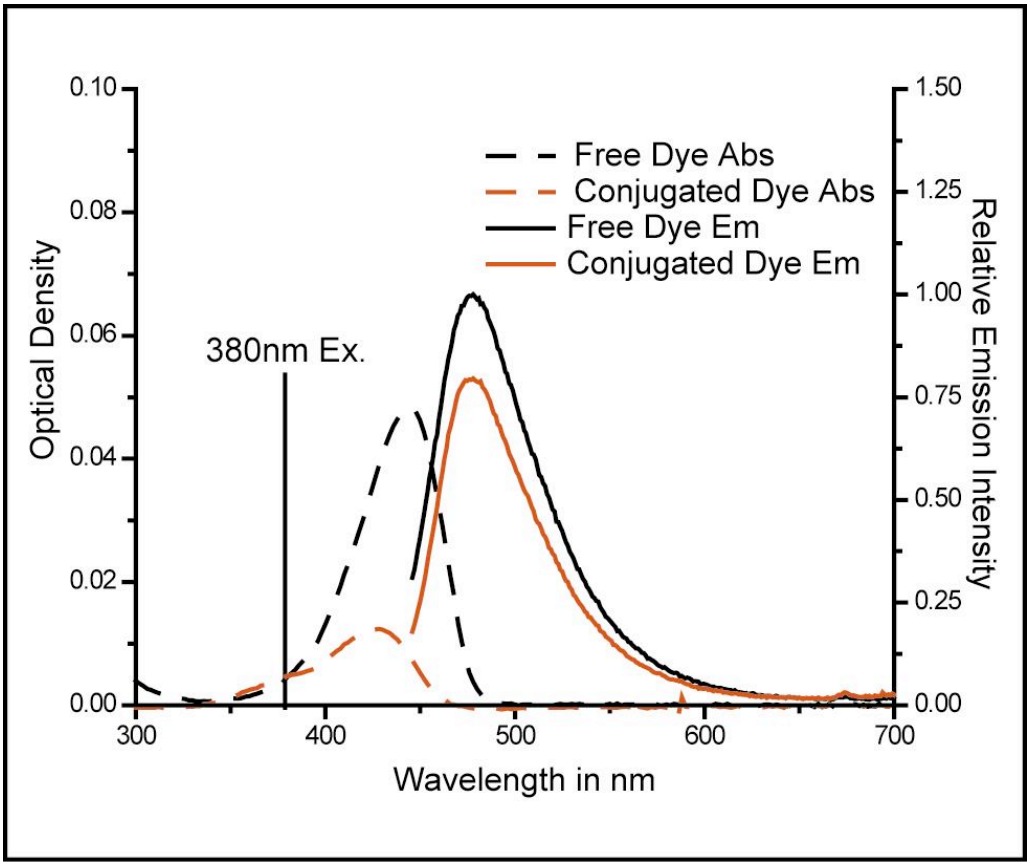


Figure 3.4: DEAC free dye compared to DEAC dye conjugated to 4-amino-1-butanol to test effect of conjugation only (i.e. without encapsulation in silica). The resulting conjugate, absorption matched at 380 nm is slightly less bright than the free dye, indicating that the enhancement observed in the particles is not due to conjugation, but rather the encapsulation.

### 3.4 Conclusions

In summary, we have reported on the synthesis of fluorescent core-shell silica nanoparticles with diameters between 15 and 20 nm, incorporating a blue-emitting dye, 7-diethylaminocoumarin-3-carboxylic acid succinimidyl ester. The dye's relative quantum yield, as measured by means of scattering corrected relative quantum yield analysis, is enhanced by an order of magnitude over that of the free dye in water. The results demonstrate that the C dot architecture can lead to significant improvements of the photophysical properties of organic fluorophores in water by sequestering them away from the solvent into a rigid, solid-state silica-type environment that itself is compatible with water. The enhanced relative quantum yield, combined with the ability to incorporate multiple dyes per particle, leads to significantly increased probe brightness as compared to free dye, making these particles excellent candidates for imaging, security, and sensing applications. These results, taken together, demonstrate a practical method for synthesizing highly fluorescent silica nanoparticles. Enhancing the performance of dyes through encapsulation in core-shell silica nanoparticles may significantly reduce costs and at the same time catapult performance characteristics of relatively inexpensive dyes to levels competitive with optimized fluorescent probes.

### 3.5 Acknowledgments

The authors thank the Army for funding through award number W911NF-06-C-0124, in collaboration with the NEI Corporation. Special thanks to the Cornell Center for Materials Research for facility use as well as the Keck FE-SEM facility and facility manager Mick Thomas for his advice on imaging the particles. Support for the CCMR is provided through the NSF Grant DMR 0520404, part of the NSF MRSEC Program.

## REFERENCES

[1]S. J. F. W. Herschel, (1845), On a case of superficial colour presented by a homogeneous liquid internally colourless, Philosophical Transactions of the Royal Society of London, 135: 143-145.

[2]A. Burns, H. Ow and U. Wiesner, (2006), Fluorescent core–shell silica nanoparticles: towards Lab on a Particle architectures for nanobiotechnology, Chemical Society Reviews, 35: 1028-1042.

[3]J. R. Lakowicz (1999) Principles of Fluorescence Spectroscopy 2nd ed., Kluwer Academic/Plenum Press, New York.

[4]E. Rampazzo, S. Bonacchi, M. Montalti, L. Prodi and N. Zaccheroni, (2007), Self-organizing core-shell nanostructures: spontaneous accumulation of dye in the core of doped silica nanoparticles, J. Am. Chem. Soc., 129: 14251-14256.

[5]C. B. Murray, D. J. Norris and M. G. Bawendi, (1993), Synthesis and characterization of nearly monodisperse CdE (E = sulfur, selenium, tellurium) semiconductor nanocrystallites, J. Am. Chem. Soc., 115: 8706-8715.

[6]E. Chang, N. Thekkek, W. W. Yu, V. L. Colvin and R. Drezek, (2006), Evaluation of quantum dot cytotoxicity based on intracellular uptake, Small 2: 1412-1417.

[7]A. M. Derfus, W. C. W. Chan and S. N. Bhatia, (2004), Probing the cytotoxicity of semiconductor quantum dots, Nano Lett 4: 11-18.

[8]F. Wang, W. B. Tan, Y. Zhang, W. Fan and M. Wang, (2006), Luminescent nanomaterials for biological labelling, Nanotechnology, 17: R1-R13.

[9]G. Bosma, C. Pathmamanoharan, E. H. A. d. Hoog, W. K. Kegel, A. v. Blaaderen and H. N. W. Lekkerkerker, (2002), Preparation of monodisperse, fluorescent PMMA-latex colloids by dispersion polymerization, Journal of Colloid and Interface Science, 245: 292-300.

[10]M. Pagliaro, R. Ciriminna, M. W. C. Man and S. Campestrini, (2006), Better chemistry through ceramics: the physical bases of the outstanding chemistry of ORMOSIL, J. Phys. Chem. B, 110: 1976-1988.

[11]J. Choi, A. Burns, R. M. Williams, Z. Zhou, A. Flesken-Nikitin, W. Zipfel, U. Wiesner and A. Y. Nikitin, (2007), Core-shell silica nanoparticles as fluorescent biological labels for nanomedicine applications, Journal of Biomedical Optics, 12(6): 1-11.

[12]C. Graf, W. Schartl, K. Fischer, N. Hugenberg and M. Schmidt, (1999), Dye-labeled poly(organosiloxane) microgels with core-shell architecture, Langmuir, 15: 6170-6180.

[13]X. Zhao, R. P. Bagwe and W. Tan, (2004), Development of organic-dye-doped silica nanoparticles in a reverse microemulsion, Advanced Materials, 16: 173-176.

[14]A. Burns, P. Sengupta, T. Zedayko, B. Baird and U. Wiesner, (2006), Core/shell fluorescent silica nanoparticles for chemical sensing: towards single-particle laboratories, Small 2: 723-726.

[15]J. E. Fuller, G. T. Zugates, L. S. Ferreira, H. Ow, N.N.Nguyen, U. Wiesner and R. S. Langer, (2008), Intracellular delivery of core-shell fluorescent silica nanoparticles, Biomaterials 29 (10): 1526-1532.

[16]E. Herz, A. Burns, S. Lee, P. Sengupta, D. Bonner, H. Ow, C. Liddell, B. Baird and U. Wiesner, (2006), Fluorescent core-shell silica nanoparticles: an alternative radiative materials platform, Proceedings of SPIE 2006: 6096-6108.

[17]D. R. Larson, H. Ow, H. D. Vishwasrao, A. A. Heikal, U. Wiesner and W.W.Webb, (2008), Silica nanoparticle architecture determines radiative properties of encapsulated fluorophores, Chemistry of Materials, 20 (8): 2677-2684.

[18]H. Ow, D. R. Larson, M. Srivastava, B. A. Baird, W. W. Webb and U. Wiesner, (2005), Bright and stable core-shell fluorescent silica nanoparticles, Nano Lett. 5(1): 113-117.

[19]A. T. R. Williams and S. A. Winfield, (1983), Relative fluorescence quantum yields using a computer-controlled luminescence spectrometer, Analyst, 108: 1067-1071.

[20]W. Stöber, A. Fink and E. Bohn, (1968), Controlled growth of monodisperse silica spheres in the micron size range, Journal of Colloid and Interface Science 26: 62-69.

[21]R. Nyffenegger, C. Quellet and J. Ricka, (1993) Synthesis of fluorescent, monodisperse, colloidal silica particles, Journal of Colloid and Interface Science 159: 150-157.

[22]W. H. Melhuish, (1961), Quantum efficiencies of fluorescence of organic substances: effect of solvent and concentration of the fluorescent solute, Journal of Physical Chemistry 65: 229-235.

[23]Sulfuric Acid vs. Refractive Index (20 degrees C), (Mettler Toledo, 2008) p. http://us.mt.com/mt/ed/appEdStyle/Sulfuric_Acid_re_e_0x000248e100025992000764 16.jsp

[24]Stated error in quantum yield of quinine sulfate dihydrate NIST standard given at 10%.

# CHAPTER 4

# LARGE STOKES-SHIFT FLUORESCENT SILICA NANOPARTICLES WITH ENHANCED EMISSION OVER FREE DYE FOR SINGLE EXCITATION MULTIPLEXING[*]

## *4.0 Summary*

We describe a polycondensation reaction of silica precursors in a modified Stöber-type basic ethanol solution to produce graded Stokes-shift core-shell silica nanoparticles providing bright and spectrally multiplexed sets of fluorescent tags that are excitable using a single excitation source. Dynamic light scattering and scanning electron microscopy demonstrate particles sizes in the sub-10nm regime. Absorption matched emission comparisons between encapsulated and free dyes in aqueous solution reveal about an order of magnitude per-dye brightness enhancements that are apparent by simply looking at the solutions under laser illumination conditions.

[*]Accepted for publication in *Macromolecular Rapid Communications*.

### *4.1 Introduction*

The preponderance of methods that rely on fluorescence of an organic dye molecule for a myriad of applications leads to a general interest from the fields of biology, information technology, and security in creating bright and stable emitters. [1, 2] While many options exist to address the applications in these fields, current trends in environmental awareness and regulation of disposal are leading the field away from toxic, heavy metal, and volatile organic compound-containing materials toward benign, water-based materials and processes. [3-7] One of these materials is silica, specifically sol-gel silica.

Since 1968 when Stöber and coworkers first reported a polycondensation reaction of silica precursors that leads to a polymeric silica network structure for the formation of monodisperse pure silica particles, there has been an interest in using the particles for tracking, tagging, and identifying flows, cells, organs, and even barcodes.[8-10] The extensive body of research concerning the chemistry of the reaction and the many well-known ways to modify silica surfaces, has acted as a broad, solid foundation upon which to build the current research. [11-15] The particularly useful covalent incorporation of fluorescent molecules into the polymeric silica matrix, first for large silica particles and later for nanoparticles allowed for the broadened use of fluorescent nanoparticles in all of the aforementioned fields, as well as an increased understanding of how dyes are incorporated into the silica matrix. [16-21] The silica matrix has a significantly higher glass transition temperature than organic polymers, leading to improvements in the optical properties of the encapsulated dyes.[17, 22] However, for spectral multiplexing, one of the drawbacks of these early particle systems is that each emission wavelength requires a different excitation wavelength. This means that in order to create spectrally distinct tags, not only do the correct dyes have to be incorporated into the sol-gel process, but the correct excitation wavelength

(usually provided by a laser) also needs to be secured. The bulk and expense of spectrally multiplexing systems thus increases with every additional color added, severely limiting this elegant method.

On the basis of the broad foundation of sol-gel silica work and the motivation provided by the need for spectral multiplexing in many different fields, recent work has focused on creating sets of particles whose emission may be stimulated by a single excitation wavelength. For example, by focusing on fluorescence resonance energy transfer (FRET), the essence of such single excitation particle sets has been recreated, while forgoing some of the fluorescence enhancement advantages of silica encapsulation due to separation of the dyes.[23] The use of FRET, whose efficiency in most applications is much less than 100 percent, to accomplish the spectral multiplexing may limit the brightness per dye molecule, however, and with 70nm diameters, the resulting particles were rather large.

In order to circumvent these challenges, we took a different, much simpler approach. In the work presented here, Dyomics dyes, DY485, DY510, DY480, and DY521, a series of dyes with graded Stokes shifts covering the visible to the near-infrared (NIR) spectrum from 540nm to 690nm in emission, but only requiring a single excitation wavelength at 514nm or 488nm, were covalently encapsulated in the silica matrix of core-shell nanoparticles using a modification of techniques described previously. [19] It should be noted that by having only a single dye emission from each nanoparticle, confusion as to whether the observed emission comes from a single particle with two emission wavelengths or two particles with a single emission wavelength, is eliminated. Furthermore, the sub-10 nanometer size regime achieved with these new particles should allow for enhanced versatility in the application of such particles to, for example, cellular bioimaging.

### *4.2 Experimental*

The covalent dye encapsulation was accomplished using a thioether linker chemistry, made up of a maleimide on the dye structure and a thiol group on the silica precursor, as shown generally in Figure 4.1(a), where –R represents the DY485, DY510, DY480, and DY521 dye structures, as shown in Figure 4.1(b). For a typical 20mL synthesis, one milligram of dye was dissolved in one milliliter of dimethylsulfoxide or dimethylformamide and conjugated with a 50 times molar excess of 3-mercaptopropyltrimethoxysilane in a nitrogen atmosphere glove box. The reaction was allowed to mix overnight. The resulting fluorescent silica precursor solution was then removed from the glove box and added to a mixture of ethanol, water, and ammonia (for the particle size desired). For the cores of the ~10nm diameter particles reported here, 17.2mL of ethanol (200 proof, Pharmco-Aaper), 308 microliters de-ionized water (18.2MΩ-cm purity), 2 mL of 2.0M ammonia in ethanol (Sigma Aldrich), 243 microliters of the conjugated dye solution, and 223 microliters of tetraethylorthosilicate (TEOS, Sigma Aldrich) were mixed in a 50mL Erlenmeyer flask and allowed to react for 9 hours. After core formation, a shell of pure TEOS was added by controlled addition of 470 microliters at a rate of 10 microliters every 7.5 minutes. Such a slow addition rate keeps the concentration of hydrolyzed TEOS below the critical nucleation concentration for new (pure silica) particles and thus, allows for the building up of the silica shell to the desired thickness on the cores.[18] For immediate investigations in water, particles are dialyzed using Snakeskin dialysis tubing (Thermo-Fisher Scientific), 3500MWCO, and a ratio of 1mL of reaction mixture to 1L of water. After dialysis samples are filtered through a 200 nanometer pore-size PTFE syringe filter for further studies. For long-term storage, particles are first dialyzed to pure ethanol, in ways as described here for water, but using a ratio of 10mL to 1L of ethanol. Particles may be stored in pure ethanol for up to 6 months.

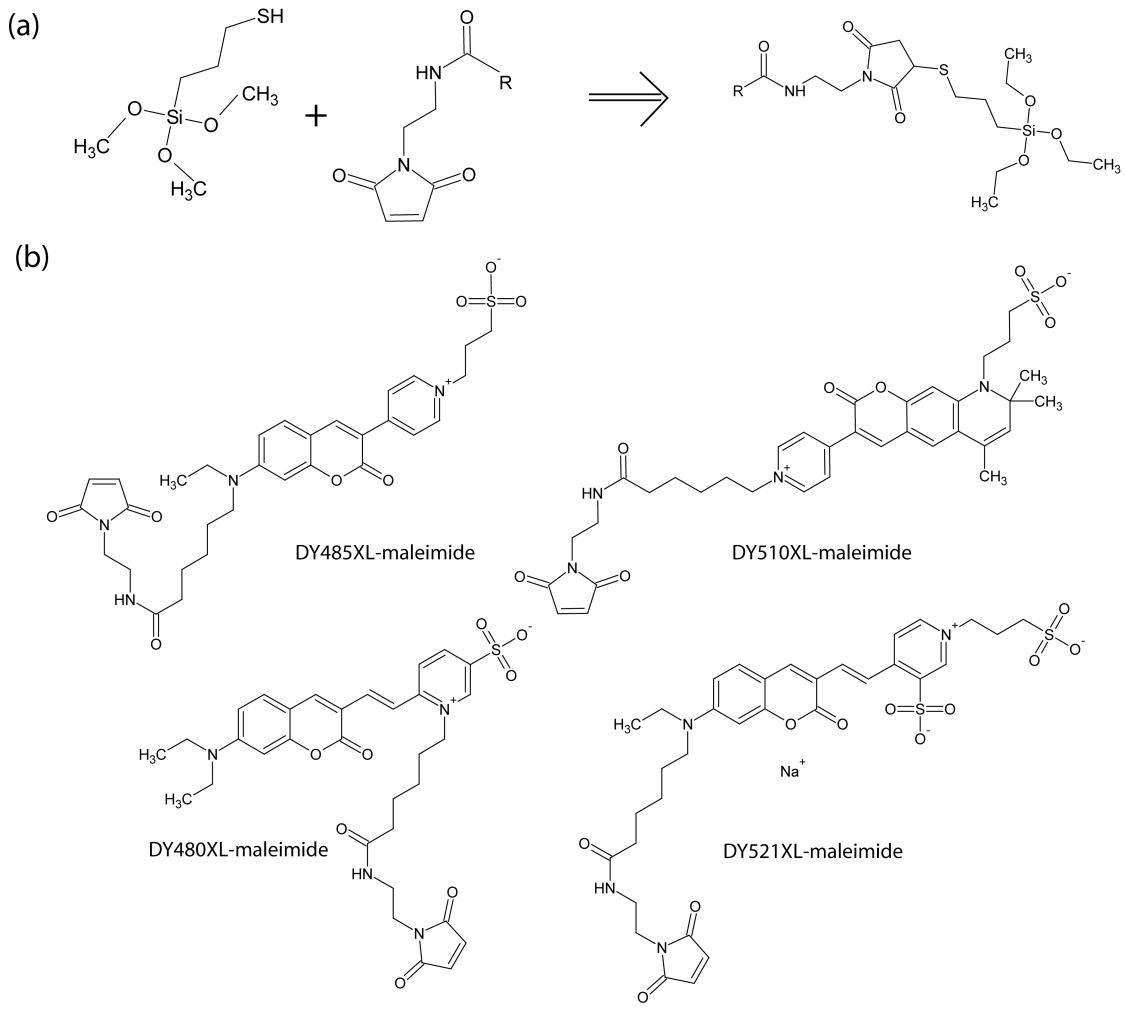


Figure 4.1. Schematic of thioether linker chemistry used to covalently bind the dyes to the silica precursor that is hydrolyzed and condensed with pure TEOS to form the matrix of the core of the particle. R=DY480, DY485, DY510, DY521.

### *4.3 Results and Discussion*

The resulting particle sizes obtained with the above-described reaction can be controlled down to the sub-10nm range. In Figure 4.2A the particle hydrodynamic diameter distribution for DY510 particles is displayed in two ways, as measured by dynamic light scattering, DLS (Malvern Zetasizer Nano-ZS, mean number statistics). The bar graph indicates the binned data, as produced by the instrument, while the line plot indicates the likely actual distribution centered around 7-8nm. Figure 4.2B is a scanning electron microscopy image of the same DY510 particles measured in Figure 4.2A, showing uniform and <10nm particle sizes. The size distributions of the DY485, DY480, and DY521 containing core shell silica nanoparticles were similar, with peak sizes measured ranging from approximately 7 to 11nm. Such small particle sizes are important for both *in vitro* applications where very low perturbation of the investigated system is necessary and *in vivo* applications where excretion through the kidneys is desirable for passage of the material out of the body.[24] Protection of the dye from the surrounding environment, separation between dyes, and the rigidity afforded by the silica allows for a significant increase in the brightness of the particles over the constituent free dye in identical surroundings, even for these small particle sizes. To quantify the brightness of the particles in comparison to free dye, standard absorption matching between free dye and particle solutions by spectrophotometry and subsequent emission investigation of these matched solutions by spectrofluorometry was performed for all particles produced. A representative example is shown for DY510 particles in Figure 4.3. The emission spectra of the absorption-matched solutions reveal a per-dye enhancement for this large Stokes shift dye of about an order of magnitude, see right side of Figure 4.3. The per-dye enhancements that result from the silica encapsulation are so significant that they can easily be detected by eye rather than having to use expensive equipment for detection. To this end photographs

of illuminated samples of free dyes and particles were taken. The pictures in Figures 4.4 (a) and (b) show 1 cm pathlength quartz cuvettes filled with, from left to right, absorption-matched DY485, DY510, DY480, and DY521 particles and dyes, respectively, in deionized water, and excited simultaneously from the right with a 514nm argon ion laser line. The two pictures were taken sequentially using identical settings of $1/13^{th}$ of a second exposure and aperture of 1.8 on a Canon Rebel EOS 300D camera fixed on a tripod, with identical power from the laser source. The significant brightness enhancement of the particles over the free dyes is very apparent from this optical comparison.

In order to quantify these results, fluorometric comparison of the absorption matched samples in deionized water were measured as shown for DY510 in Figure 4.3 on all the samples pictured. The quantitative per-dye enhancements realized by the particle encapsulation over free dye were found to be a *factor of* 12 for DY485, 10 for DY510, 11 for DY480, and 6.5 for DY521 particles (listed from green to red emission), with errors of ±10% as deduced from measurements of three particle synthesis batches per dye. Additional testing of the DY510 free dye, with quenched conjugation moiety, suggests that the fluorescence enhancements are due to the protective silica environment rather than chemical conjugation (see Appendix A).

A very important issue in nanoparticle studies is their colloidal stability in pure water as well as buffered solutions. In pure water silica nanoparticles are electrostatically stabilized due to the net negative charge on silica at neutral pH (the isoelectric point of silica is at pH 2-3).[25] In order to achieve colloidal stability in buffers, i.e. at high salt concentrations relevant to biological imaging, where repulsive Coulomb potentials are effectively screened, a PEG-silane (Gelest SIM6492.7) surface coating provides steric stabilization, as demonstrated in a recent animal study.[24]

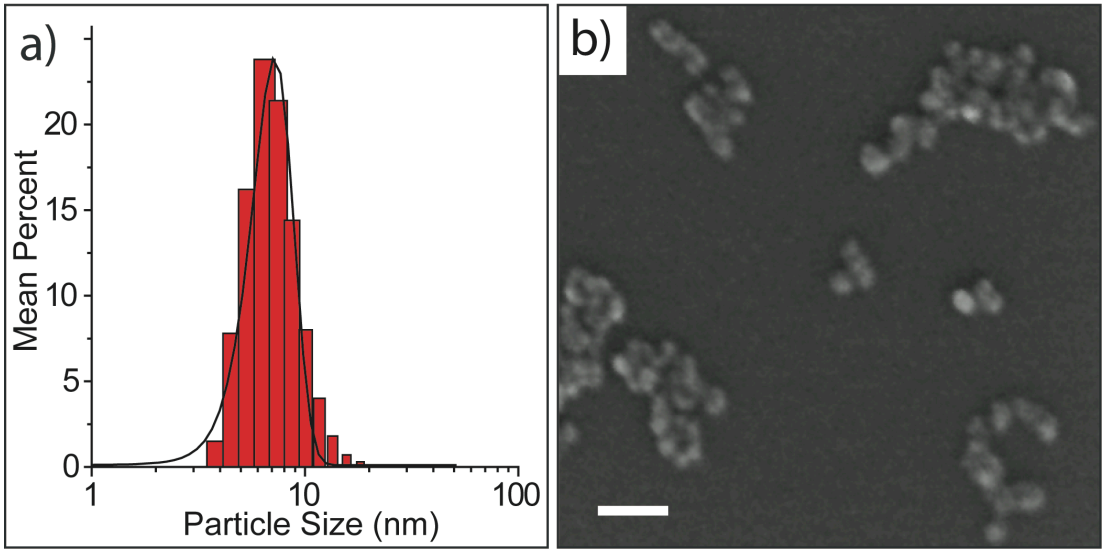


Figure 4.2. (a.) Hydrodynamic particle size for DY510 particles from dynamic light scattering (mean number percent). (b.) Scanning electron micrograph of particles measured in (a.) showing uniform particle sizes (scale bar is 50nm).

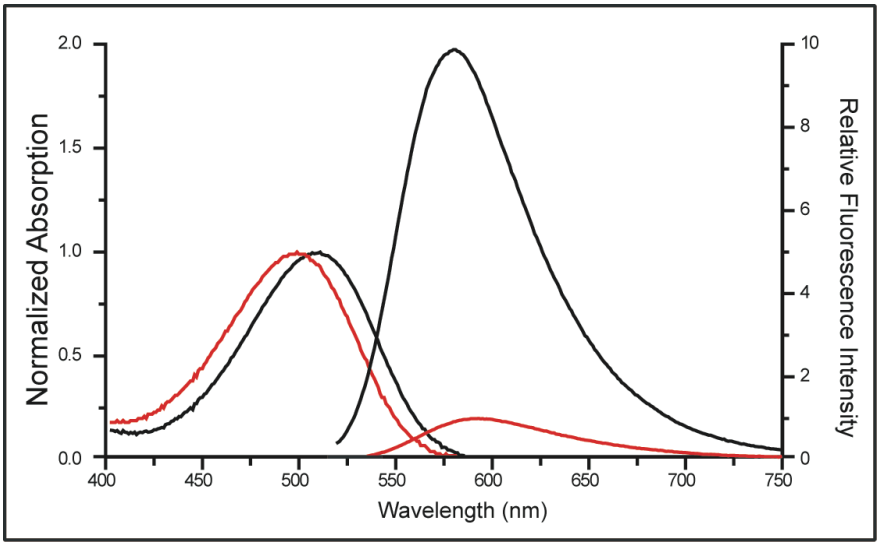


Figure 4.3. Absorption (left) and emission (right) comparison of DY510 free dye (red) and DY510 particles (black).

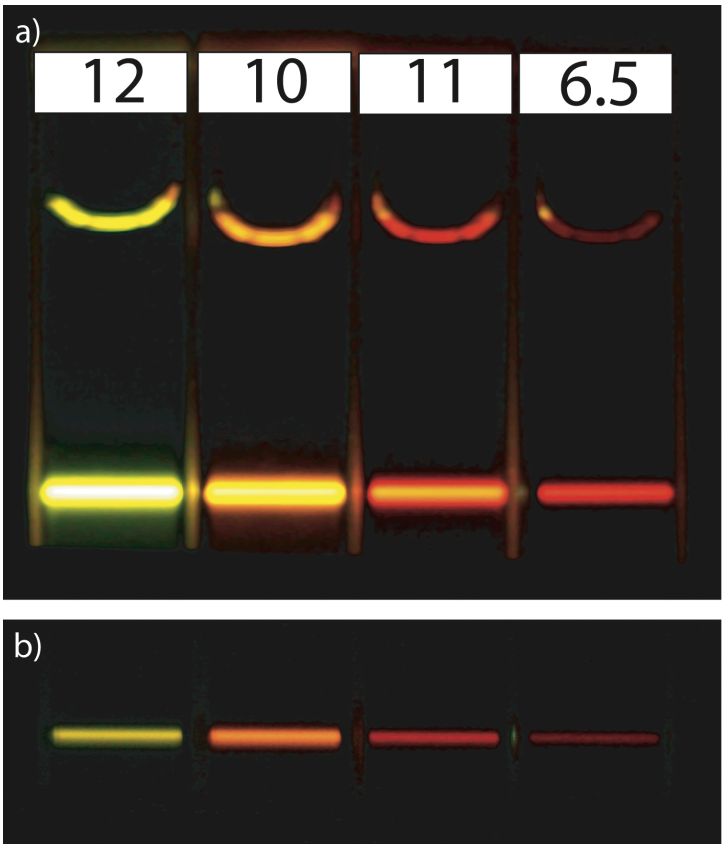


Figure 4.4. (a.) Photograph of fluorescence from DY485, DY510, DY480, DY521 particles in water in cuvettes, concentration matched to corresponding free dye in water, shown in (b.) Images (a.) and (b.) were taken sequentially using identical settings of $1/13^{th}$ of a second exposure and aperture of 1.8 on a Canon Rebel EOS 300D camera fixed on a tripod and identical power from a single 514nm line argon ion laser source coming from the right. Fluorometrically measured peak wavelength enhancement factors are shown in (a.) at the tops of the cuvettes.

### *4.4 Conclusions*

Our graded Stokes-shift particles constitute a strong fluorescent silica particle platform by providing a means to produce bright and stable spectrally multiplexed sets of fluorescent tags that are benign, non-toxic, contain no heavy metals, and are excitable using a single excitation source. It is the first time (to our knowledge) that silica particles of this size have been shown to simultaneously provide such a high per-dye enhancement in emissive properties over their free dye constituents under identical solvent conditions, combined with the ability to spectrally multiplex with a single excitation wavelength.

### *4.5 Acknowledgements*

Special thanks to the Army for current funding through award number W911NF-06-C-0124, in collaboration with the NEI Corporation. The authors would like to also thank the Cornell Center for Materials Research (CCMR) for past financial support for this research. Support for the CCMR is provided through the NSF Grant DMR 0520404, part of the NSF MRSEC Program. We thank the Cornell Nanobitechnology Center for use of several of their facilities. U.W. is a cofounder of Hybrid Silica Technologies.

# APPENDIX A

## *Supporting Information for Chapter 4*

### *Dye-conjugate comparison to free dye for DY510*

DY510 maleimide dye was conjugated to 4-mercapto-1-butanol to investigate the effect of conjugation, independent of the effects of encapsulation. Free DY510 dye and the conjugate were absorption matched at their peak and their fluorescence was then measured. The results, shown in Figure A1, indicate that conjugation does not have a significant effect on the enhancement of the dye. These data, in comparison to the data in Figure 4.1, suggest that encapsulation within the silica matrix is the dominant effect leading to the brightness enhancement.

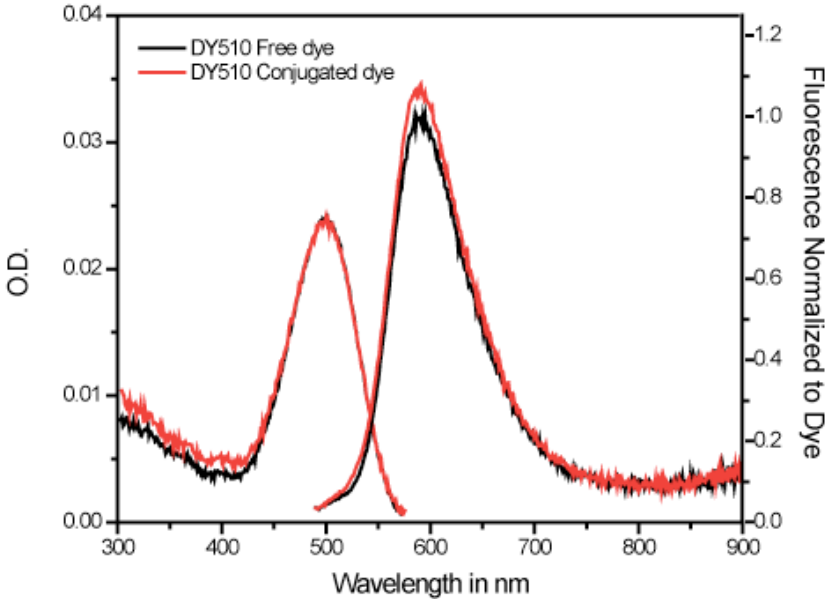


Figure A1: Absorption and emission spectra of DY510 free dye and DY510 dye conjugated to 4-mercapto-1-butanol to quench the conjugation moiety, indicating that conjugation has a minimal effect on brightness enhancement.

## REFERENCES


[1] M. S. T. Gonçalves, *Chemical Reviews* 2009, *109*, 190.

[2] J. R. Lakowicz, "*Principles of Fluorescence Spectroscopy"*, 2 edition, Kluwer Academic/Plenum Publishers, New York, 1999.

[3] R. E. Bailey, A. M. Smith, S. Nie, *Physica E: Low-dimensional Systems and Nanostructures* 2004, *25*, 1.

[4] A. D. Yoffe, *Advances in Physics* 2001, *50*, 1.

[5] A. M. Derfus, W. C. W. Chan, S. N. Bhatia, *Nano Lett* 2004, *4*, 11.

[6] C. Kirchner, T. Liedl, S. Kudera, T. Pellegrino, A. M. Javier, H. E. Gaub, S. Stölzle, N. Fertig, W. J. Parak, *Nano Lett* 2005, *5*, 331.

[7] E. Chang, N. Thekkek, W. W. Yu, V. L. Colvin, R. Drezek, *Small* 2006, *2*, 1412.

[8] A. Burns, H. Ow, U. Wiesner, *Chemical Society Reviews* 2006, *35*, 1028.

[9] A. Burns, P. Sengupta, T. Zedayko, B. Baird, U. Wiesner, *Small* 2006, *2*, 723.

[10] W. Stöber, A. Fink, E. Bohn, *Journal of Colloid and Interface Science* 1968, *26*, 62.

[11] A. v. Blaaderen, J. A. v. Geest, A. Vrij, *Journal of Colloid and Interface Science* 1992, *154*, 481.

[12] G. H. Bogush, C. F. Z. IV, *Journal of Colloid and Interface Science* 1991, *142*, 1.

[13] G. H. Bogush, C. F. Z. IV, *Journal of Colloid and Interface Science* 1991, *142*, 19.

[14] G. H. Bogush, M. A. Tracy, C. F. Z. IV, *Journal of Non-crystalline Solids* 1988, *104*, 95.

[15] A. P. Philipse, A. Vrij, *Journal of Chemical Physics* 1987, *87*, 5634.

[16] A. v. Blaaderen, A. Vrij, *Langmuir* 1992, *8*, 2921.

[17] D. R. Larson, H. Ow, H. D. Vishwasrao, A. A. Heikal, U. Wiesner, W.W.Webb, *Chemistry of Materials* 2008, *20*, 2677.

[18] R. Nyffenegger, C. Quellet, J. Ricka, *Journal of Colloid and Interface Science* 1993, *159*, 150.

[19] H. Ow, D. R. Larson, M. Srivastava, B. A. Baird, W. W. Webb, U. Wiesner, *Nano Lett.* 2005, *5*, 113.

[20] E. Rampazzo, S. Bonacchi, M. Montalti, L. Prodi, N. Zaccheroni, *J. Am. Chem. Soc.* 2007, *129*, 14251.

[21] C. Graf, W. Schartl, K. Fischer, N. Hugenberg, M. Schmidt, *Langmuir* 1999, *15*, 6170.

[22] E. Herz, H. Ow, D. Bonner, A. Burns, U. Wiesner, *Journal of Materials Chemistry* 2008, *accepted*.

[23] L. Wang, W. Tan, *Nano Lett* 2006, *6*, 84.

[24] A. Burns, J. Vider, H. Ow, E. Herz, O. Penate-Medina, M. Baumgart, S. M. Larson, U. Wiesner, M. Bradbury, *Nano Letters* 2009, *9*, 442.

[25] C. J. Brinker, G. W. Scherer, "*Sol-Gel Science: The physics and chemistry of sol-gel processing"*, Harcourt Brace Jovanovich, Boston, 1990, p. 908.

# CHAPTER 5

# DYE STRUCTURE-OPTICAL PROPERTY CORRELATIONS IN NEAR-INFRARED FLUORESCENT CORE-SHELL NANOPARTICLES*


## *5.0 Abstract*

In this paper we report on dye structure – optical property correlations for a range of near-infrared emitting (NIR, 650nm-900nm) fluorescent dyes in a 9-14nm diameter core-shell silica particle architecture (C dots), including Cy5, Alexa Fluor 700, DY730, Alexa Fluor 750, and DY780. For each dye an apparent per-dye enhancement in fluorescence is observed over free dye in aqueous solution ranging from 1.2x to 6.6x, highlighting the versatility of the silica encapsulation approach. For the Cy5 and DY730 dye/particle sample pairs photobleaching was undertaken and revealed that the particles photobleach slower than the dyes. For a particular NIR dye series with identical chemical backbone, DY730, DY731, DY732, and DY734, we demonstrate that with increasing number of sulfonated substituent groups the per-dye brightness enhancement decreases. Finally, we show that in special cases, like Cy5, brightness enhancement of dyes in dots over free dye may be a combination of effects from dye conjugation chemistry and immobilization in the silica matrix. These results provide powerful design criteria for next generation optical probes for applications ranging from bioimaging to security.



*Originally Published as: Erik Herz, Hooisweng Ow, Daniel Bonner, Andrew Burns, Ulrich Wiesner. *Dye Structure-Optical Property Correlations in Near-Infrared Fluorescent Core-Shell Silica Nanoparticles*. Journal of Materials Chemistry, in press. Reproduced by permission of The Royal Society of Chemistry

### *5.1 Introduction*

The study of fluorescent nanoparticles is an emerging research area focused on potential biological and photonic applications such as imaging, optical bar-coding, sensing, and optically-active materials.[1-6] Research communities in bioimaging, fluorescent particle chemistry, and beyond are moving toward detection and excitation in the near-infrared region (NIR) to decrease spectral interference, increase penetration depth and potentially enhance signal-to-noise ratios, aided by the ready availability of laser-diode excitation sources.[7, 8] However, several challenges exist in implementation of these particles, such as photodegradation, potential toxicity (leaching of heavy metal ions from quantum dots or cytotoxic dyes from non-covalently bound dye-doped particles) and quenching.[9-11] Hence, there is a need to protect the fluorophore(s) (dyes or quantum dots), while producing bright, stable, and size-controlled particles.

Hybrid particle architectures allow for optimized combinations of matrix and encapsulated payload properties. For example, a matrix can both protect the fluorophore and provide a convenient binding surface for interaction with the environment, while the fluorophore, in turn, can provide the desired optical properties.

A core-shell nanoparticle architecture offers particular control over placement of the fluorophores relative to the environment, allowing e.g. for tuning of the fluorophore-environment interaction. One of the main matrix materials currently used for such particles due to its stability, chemical versatility and desirable optical properties is silica.[12-19] In previous papers we introduced fluorescent core-shell silica nanoparticles, referred to as C-dots, with enhanced brightness and photostability levels relative to free dye in aqueous solutions.[20, 21] While NIR C-dots based on Alexa Fluor dyes were described therein, the present paper gives a full account of the generalized covalent incorporation of a number of NIR dyes from different dye sources into the core of core-shell silica nanoparticles not reported on before, with characterizations of

their size and brightness. Specific emphasis will be on the development of detailed dye chemistry – optical performance correlations that are lacking in the literature to date. The fluorescent core-shell silica particles produced exhibit absorption peaks ranging from 650 to 780nm and emission peaks from 660 to 800nm, depending on the dye incorporated. These wavelengths are of particular importance in biological imaging, where background fluorescence in the NIR wavelength regime (650 – 900nm) is at a minimum relative to the traditionally utilized visible wavelengths, thereby generating higher signal-to-noise ratios.[22, 23] Similarly, in tagging or bar-coding applications bright, non-visible emitters (such as those in the NIR) are of interest.

### *5.2 Experimental*

#### *5.2.1 Particle Synthesis*

For a typical particle synthesis of 25mL scale, the dye was dissolved to 4.5mM concentration in degassed, dry dimethylsulfoxide, dimethylformamide, or ethanol (depending on solubility) in a nitrogen-filled glovebox. The Cy dye was purchased from GE Healthcare, while the Alexa Fluor dyes were purchased from Invitrogen. The DY dyes were received from Dyomics. The solvents were purchased from Pharmco and used as received. 100 microliters of the resulting solution was conjugated with a 50 times molar excess of either 3-mercaptopropyltrimethoxysilane (for maleimide dyes) or 3-aminopropyltriethoxysilane (for N-hydroxysuccinimidyl ester dyes) (both from Gelest) and stirred for 12 hours under nitrogen. The dye-silicate solution was then removed from the glovebox and added to a mixture of ethanol, water, and ammonia (for the particle size desired). For example, for ~10nm diameter particles (by DLS) one would use 0.385mL of 18.2MΩ-cm water, 21.75mL of ethanol (Pharmco), and 2.5mL of 2.0M ammonia in ethanol (Sigma Aldrich). To this mixture 0.279mL tetraethylorthosilicate (Sigma Aldrich) was added. It should be noted that different

dyes will produce different particle sizes with the same reaction conditions due to differences in the reaction kinetics of the resulting fluorescent silica conjugate. After co-condensation under vigorous magnetic stirring over a 12 hour period, the cores were formed. Addition of further TEOS aliquots to the core solution, at a rate of 1 microliter per milliliter of reaction volume per quarter hour, produced a pure silica shell. Note, a stepwise addition of TEOS is necessary to keep the total amount of TEOS and hydrolyzed TEOS in the reaction at any time below the critical nucleation concentration to keep new (non-fluorescent) particles from forming. [14] For photobleaching experimentes particles were covalently coated with methoxy-terminated poly(ethylene glycol) chains (PEG, ~0.5kDa), which increases the animal tolerance of the probes for *in vivo* studies. [22] The addition of PEG to the surface increases the hydrodynamic diameter of the particles by about 2nm. After synthesis, samples were dialyzed to 18.2MΩ-cm deionized water or absolute ethanol using 3500 MWCO Snakeskin dialysis tubing (Pierce) and filtered with 0.2 micron PTFE syringe filters (Fisher Scientific), prior to characterization or storage.

### *5.2.2 Characterization*

Dialyzed particles were diluted at least 1:10 for dynamic light scattering measurements on either a Malvern Zetasizer Nano-ZS or a Brookhaven BI200 SM depending on the availability of the instrument. Standard polystyrene 1.5mL micro-cuvettes (Perfector Scientific) were used for the Malvern instrument while standard glass vials were used for the Brookhaven instrument. A standard CONTIN analysis was used to determine the average hydrodynamic particle size and size distribution for each sample. Number statistics were used in order to remove effects of dust in the sample.

Absorption and emission data were collected for the particles and constituent free dye under identical aqueous conditions. The samples were diluted to match optical density at the peak absorption wavelength using a Molecular Devices 384 instrument in 1cm path-length quartz cuvettes, under the assumption that the molar extinction coefficient of the dyes does not significantly change upon encapsulation into the silica nanoparticles. All optical densities were matched at or below 0.1. The cuvettes were then transferred to a Photon Technology International QM4 spectrofluorometer for emission measurements, using an excitation wavelength equal to the peak absorption wavelength. Baselines for both the spectrophotometric and spectrofluorometric data were used to correct the data.

Using a custom-built photobleaching apparatus, constructed in our laboratory, photobleaching of absorption matched dye and particle samples was tested. The apparatus consisted of a diode laser producing 635nm light coupled into a 3.5X (0.10 NA) objective, to provide the power necessary for photobleaching (between 530 microwatts and 3.5mW). A glass capillary with 0.4mm inner diameter and filled with two microliters of sample, diluted to approximately $10^{-10}$ molar of dye or the equivalent number of dyes within particles, was positioned parallel to the beam with a three axis tilt mount. Using this setup, the excited path length was approximately 1.5cm, with negligible dead volume. The emission produced from the samples was passed through a 500nm long-pass filter and collected using a Perkin-Elmer single photon counting module. Trace data from the single photon counting module were processed using a Correlator.com autocorrelator card, background corrected, and then normalized to the initial value. All data was collected in triplicate and the average and standard deviation calculated.

Scanning electron microscopy was performed on a LEO 1550 FE-SEM with 1.0kV accelerating voltage to minimize sample degradation during imaging. Dilute

dialyzed samples in ethanol (to promote fast drying) were dispersed on a piece of silicon wafer and allowed to dry, then vacuum dried for at least 1 hour before imaging.

### *5.3 Results and Discussion*

#### *5.3.1 Encapsulation of different NIR dyes in core-shell silica nanoparticles*

The dyes used in the present study are (in order of increasing emission wavelength) Cy5, Alexa Fluor 700, DY730, DY731, DY732, DY734, Alexa Fluor 750, and DY780. These long-wavelength dyes were originally designed for *in vitro* or *in vivo* biological imaging and are thus hydrophilic in nature. As we will show, they all benefit from successful incorporation into a rigid silica matrix, thus demonstrating the versatility of the C-dot approach. Our efforts focus on producing core-shell silica nanoparticle architectures covalently encapsulating organic fluorophores in a dye-rich core surrounded by a pure silica shell.[20, 21] This type of particle is produced by a modified Stöber process, shown schematically in Figure 5.1 with DY780 maleimide (DY780-mal) as an example. Normalized emission spectra are shown in Figure 5.2 for the distinct emission wavelengths of the Cy5, Alexa Fluor 700, DY730, Alexa Fluor 750 and DY780 particles produced, demonstrating the spectral range that these particles cover. To our knowledge, the peak emission wavelength of the DY780-mal particles, at 803nm, is the longest wavelength emitting fluorescent hybrid silica nanoparticle reported to date. The bottom of Figure 5.1, in step 4, shows representative results of dynamic light scattering experiments and SEM sizing (inset) for the DY780 particles, indicating a hydrodynamic size (diameter) of about 10nm. DLS/SEM (peak) particle sizes for all of the particles produced in this study are indicated in Table 5.1. They range from 9 to 14nm, demonstrating the ability to reproducibly synthesize 10-15nm diameter fluorescent particles, independent of the specifics of the dye used.

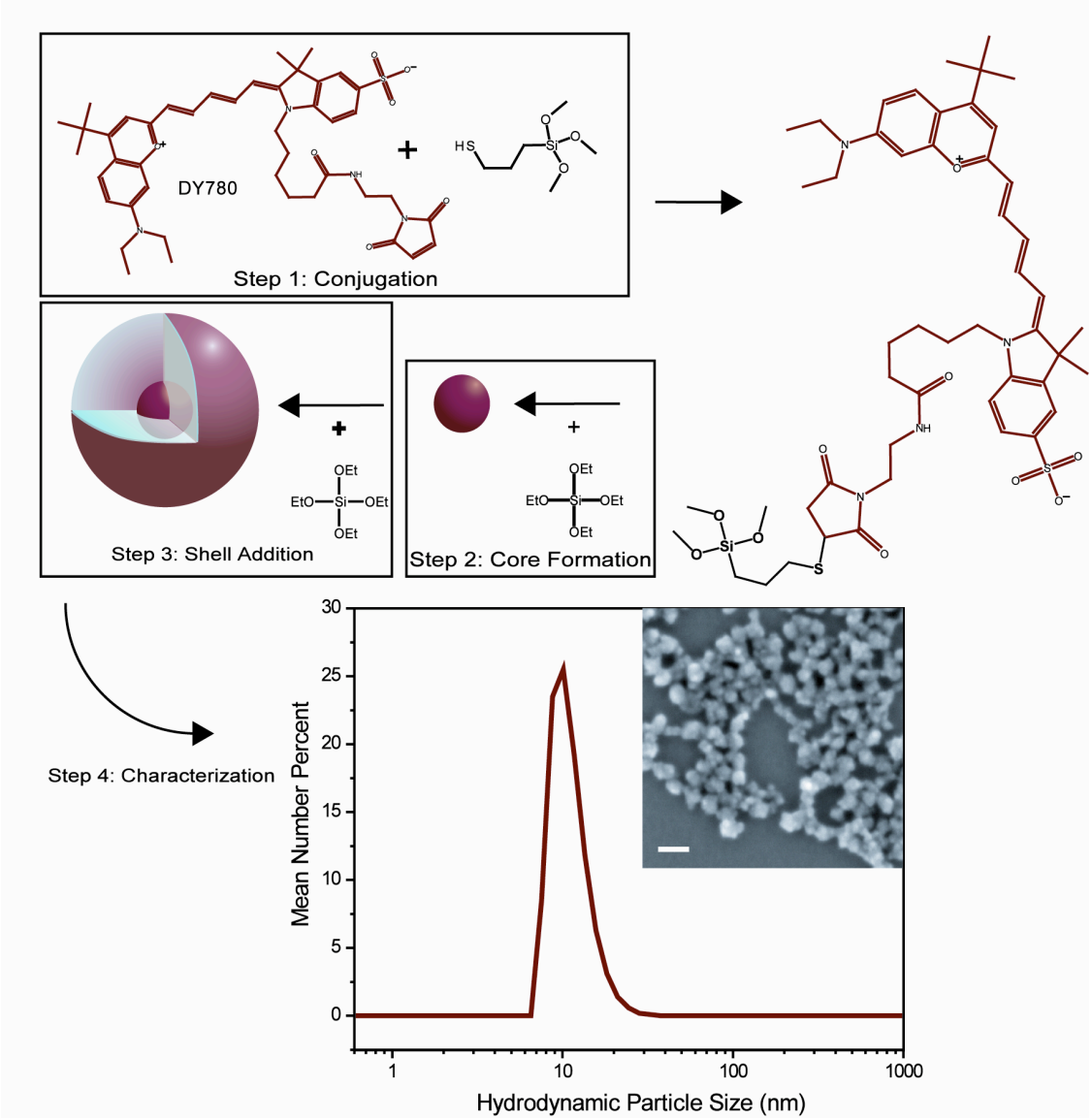


Figure 5.1: Fluorescent silica nanoparticle reaction schematic showing the dye structure for DY780 with a maleimide conjugation chemistry to conjugate to 3-mercaptopropyltrimethoxylsilane. Note, steps two and three occur in basic ethanol solution. Hydrodynamic particle size (diameter) distribution as measured by dynamic light scattering on a dilute aqueous colloidal suspension of DY780 particles. Inset shows an SEM image of the as made particles. Scale bar is 50nm. Note, aggregation occurs during drying onto silicon wafer surface.

The absorption and emission spectra for Cy5, Alexa Fluor 700, DY730, Alexa Fluor 750, and DY780 free dye and particles are shown in Figure 5.3. Except for DY780, all samples show essentially unchanged absorption and emission characteristics upon encapsulation into the C dot architecture. For further optical characterization, we have chosen to use the parameter $E_{fluor}$ to represent the apparent per-dye enhancement in fluorescence intensity upon encapsulation, defining $E_{fluor} = I_{particle} / I_{dye}$ where $I_x$ is the peak emission intensity of the corresponding absorption-matched solution. For Cy5, for example, from the data in Figure 5.3a, $E_{fluor} = 2.0$. By taking 3 sample measurements for each particle set and calculating $E_{fluor}$, error bars were estimated to be approximately ± 10% for most particles. Table 5.1 summarizes the results for all dyes incorporated into silica particles in this study with peak wavelengths of absorption and emission, $E_{fluor}$ values with error bars, and an indication of whether a maleimide (MAL) or n-hydroxysuccinimidyl ester (SE) was used as the conjugation chemistry. Per-dye enhancements range from 1.2 to 6.6 evidencing significant brightness improvements through encapsulation and corroborating earlier results on other dyes, [1, 20-22, 24] in the visible part of the optical spectrum.

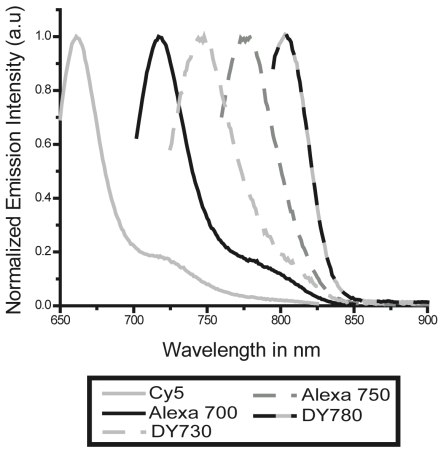


Figure 5.2: Normalized emission spectra of the set of fluorescent core-shell silica particles produced for this work, showing the extent of spectral coverage achieved.

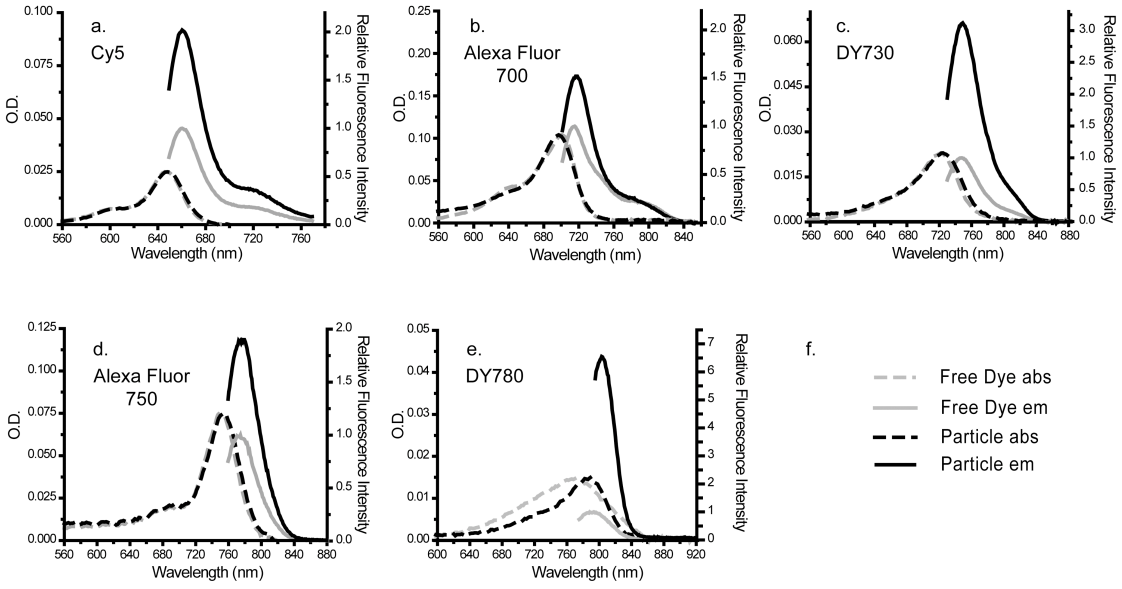


Figure 5.3: Absorption (left axis) and emission (right axis) measurements made for: (a) Cy5; (b) Alexa Fluor 700; (c) DY730; (d) Alexa Fluor 750; and (e) DY780 core-shell silica nanoparticles in water and the corresponding free dye. Particle emission intensity is shown relative to the free dye in water. The key to the graphs is given in part f. Please note that the absorption spectra of encapsulated and free dye are nearly indistinguishable for several of the dye/particle sets.

Table 5.1: Characterization results for the fluorescent (NIR) core-shell silica particles produced in this study, including average diameter (from DLS), peak absorption and emission wavelengths in water and relative enhancement over free dye in water $E_{fluor}$ as defined in the text.

| Dye Incorporated | Particle Hydrodynamic Size by DLS | Peak Particle Absorption Wavelength | Peak Particle Emission Wavelength | $E_{fluor}$ |
|---|---|---|---|---|
| Cy5-MAL | 10nm | 648 | 661 | 2.0 ± 0.2 |
| Alexa 700-SE | 9.1 nm | 697 | 718 | 1.5 ± 0.2 |
| Alexa 750-MAL | 10nm | 753 | 780 | 1.9 ± 0.2 |
| DY730-SE | 11nm | 726 | 750 | 3.2 ± 0.2 |
| DY731-SE | 12nm | 706 | 746 | 2.1 ± 0.1 |
| DY732-SE | 13.5nm | 718 | 749 | 1.3 ± 0.2 |
| DY734-SE | 10nm | 720 | 748 | 1.2 ± 0.1 |
| DY780-MAL | 11nm | 790 | 803 | 6.6 ± 1 |

It should be emphasized that $E_{fluor}$ is an apparent brightness enhancement. Absolute or relative quantum yield measurements must be performed to quantify the absolute increases over the behavior of the free dye in solution. Such measurements are quite involved, however, and have not been attempted for this larger dye and C-dot series. They have been performed in parallel studies on other dye systems, demonstrating similar results [24], see below. Quantum yield measurements are sensitive to changes in the overall emission spectra, which may be altered upon encapsulation. Furthermore, although particle sizes are small and thus scattering differences between dyes and particles are expected to be negligible, in particular for the NIR spectral range studied here, different scattering properties of free dye versus particles may also alter the results. Nevertheless, the data reported in Table 5.1 suggest that dye encapsulation into the core-shell silica nanoparticle architecture described here leads to improvements of the per-dye brightness levels. This is consistent with in depth photophysical characterizations, including static and time-resolved photophysical measurements on rhodamine-based C-dots, reported earlier, suggesting that per-particle brightness enhancements ($B.E_{p.}$) over free dye in water can be estimated by the product of the apparent per-dye quantum yield increase over the free dye in water, $QY_P/QY_{D,}$ multiplied by the number of dyes per particle, shown in Equation 1. [1, 20]

$$BE_p = \frac{\#\ \text{Dyes} \times QY_p}{QY_D} \qquad \text{Equation 1}$$

This is further corroborated by recent scattering corrected relative quantum yield measurements on coumarin based C-dots showing a ten-fold increase in quantum yield for the dye upon encapsulation in a C-dot. [20, 24]

### *5.3.2 Dye structure – optical property correlations for encapsulations within a dye family*

In addition to covering the NIR spectral range through incorporation of different organic fluorophores, a series of dyes, DY731, DY732, and DY734, was incorporated into the dots (Figure 5.4) that share the same chemical backbone, conjugation chemistry, and general absorption and emission characteristics of DY730 (parent dye, Figure 5.4a), but incorporate an increasing number of charged sodium sulfonate substituents. These groups are commonly added to increase dye solubility in water relative to the parent dye. DY731 has a single charged sulfonate group (structure in Figure 5.4e), DY732 has two (Figure 5.4c), and DY734 has three (Figure 5.4f), while the parent dye, DY730, has none. Although the particles are synthesized in a high dye concentration solution and the silica matrix of the particle locks in the dye, the lack of a short wavelength shoulder in the absorption spectra for the DY730, DY732 (Figure 5.4b and 4.4d) and DY734 particles (not shown) suggests that aggregation is not dominant. By comparing these four dyes, the influence of negatively-charged species on dye incorporation into the silica particles and the concomitant effects on enhancement could be probed. For example, it might be expected that dye-matrix interactions with the (negatively) charged silica matrix, as is produced in the modified Stöber-type synthesis, would vary as a function of the charge-state of the dye.

The experimental results (Table 5.1) suggest that $E_{fluor}$ decreases with increasing charge. Significantly, the zwiterionic dye leads to particles that demonstrate the greatest enhancements over free dye, with the enhancement decreasing with increasing number of sulfonate groups. Changes in $E_{fluor}$ values may be attributed to increases in the quantum yield of the parent fluorophores in aqueous solution, caused by increases in solubility and decreased aggregation at high concentrations for those

dyes with more sulfonate groups. Alternatively, the effect may be due to the increasing steric bulk of the added sodium sulfonate groups shielding the dye from interactions with the silica matrix, and decreasing some of the beneficial effects of encapsulation. While likely it is a combination of these effects, we believe the second is more dominant since no significant spectral changes were observed in the absorption spectra between free and encapsulated dyes.

### *5.3.3 Photobleaching comparison of fluorescent silica nanoparticles and free dye*

Absorption matched solutions of Cy5 and DY730 containing core-shell silica nanoparticles and dye were photobleached as described above. The Cy5 particles and dye were photobleached using 3.5mW of power at the sample and the DY730 particles and dye were photobleached using 530 microwatts of power at the sample. As shown in the peak intensity normalized plot in Figure 5.5 (a) for Cy5 and Figure 5.5 (b) for DY730, the particles photobleach more slowly than the dye in both cases, reaching 1/e in 49 seconds versus 37 seconds for the Cy5 dye and 345 seconds versus 246 seconds for the DY730 dye. It should be noted that the power a sample is typically subjected to during the collection of a single image using a confocal scanning microscopy setup is equivalent to the first few seconds of the photobleaching shown here. With this and the enhancements shown in Table 5.1 in mind, the particles clearly provide higher contrast for a longer period of time than do the dyes.

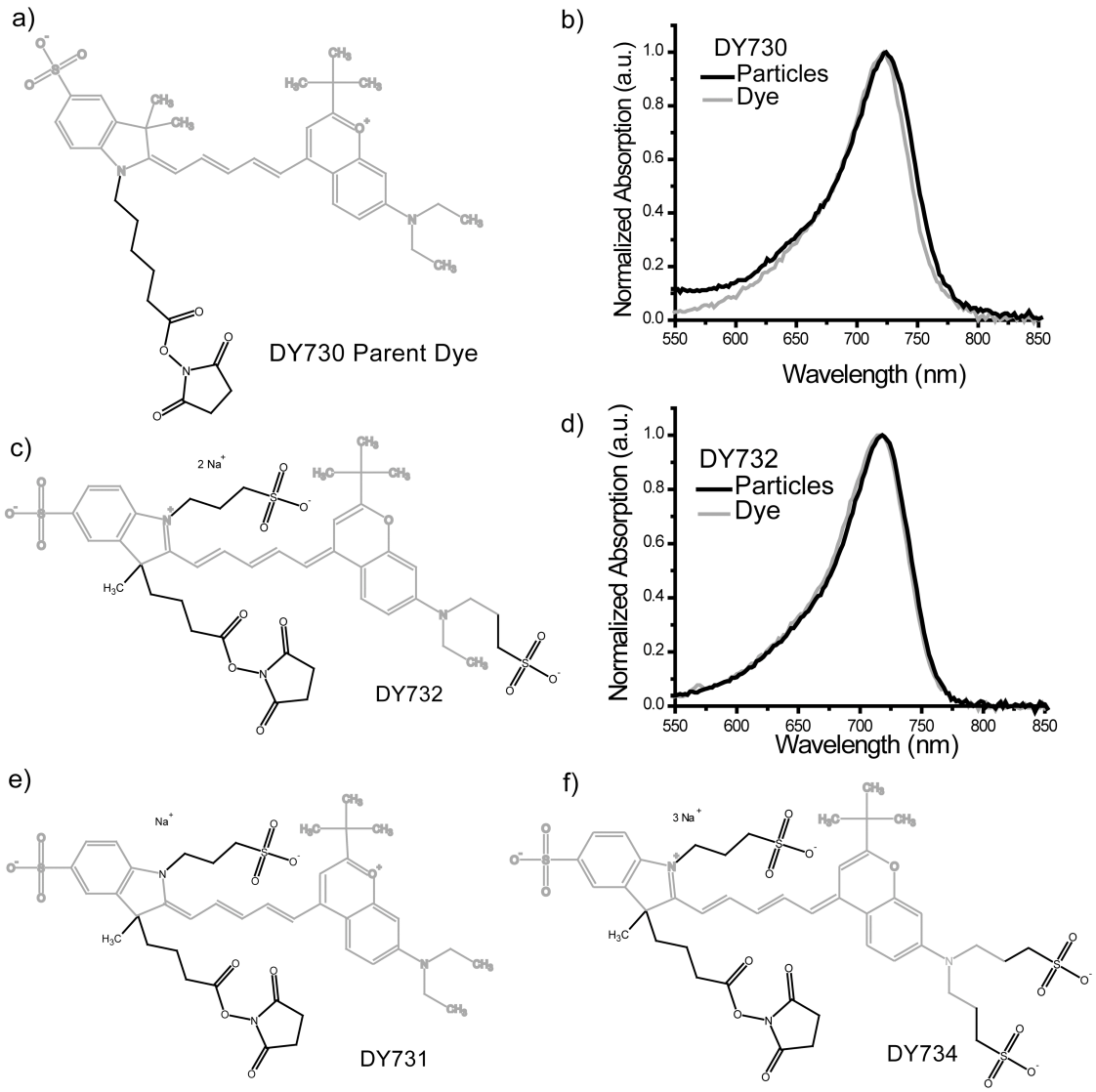


Figure 5.4: (a) DY730 parent dye structure; (b) Absorption spectra for DY730 dye and core-shell silica nanoparticles in aqueous solution; (c) DY732 dye structure; (d) absorption spectra for DY732 dye and silica nanoparticles in aqueous solution; (e) DY731 dye structure; (f) DY734 dye structure. All dye structures are displayed as shown on the Dyomics webpage.

### *5.3.4 Comparison of free dye to conjugated dye*

Finally, absorption and emission data were taken for free dye and dye conjugated to 4-amino-1-butanol for dyes with n-hydroxysuccinimidyl ester functional groups or 4-mercapto-1-butanol for dyes with maleimide functional groups, to investigate the effect of conjugation, independent of the effect of encapsulation. These data are shown for Cy5, DY730, and DY780 in water in Figure 5.6. The results indicate that conjugation can, but often does not, have an effect on the enhancement of the dye. Comparing the data in Figure 5.6 and the information from Table 5.1, it is important to note that for certain dye types, such as Cy5, enhancements may be due to a combination of effects from the covalent dye conjugation and silica encapsulation, while for other dyes, such as DY730 and DY780, encapsulation within the silica matrix is the dominant effect, leading to the brightness enhancement.

## *5.4 Conclusion*

We have synthesized a series of fluorescent core-shell silica nanoparticles via a modified Stöber process, referred to as C-dots, to investigate dye structure – optical property correlations for near-infrared emitting dyes with an emission range from 660 to 800nm. All hybrid silica nanoparticles were found to have enhanced per-dye emission properties relative to the constituent dye in aqueous solution, with apparent enhancement factors between 1.2 and 6.6. Particle diameters were in the 10nm range, with the smallest size going down to 9nm. Additionally, a series of dyes with increasing number of (charged) sulfonate groups were incorporated to elucidate the effects of the number of substituents and charge states on the optical properties of the resulting particles while the dye backbone structure was kept constant. It was found

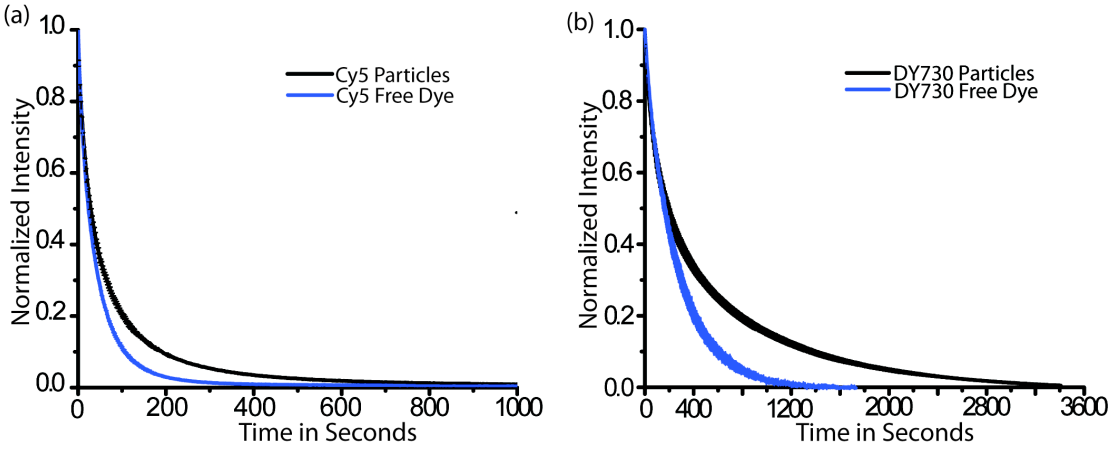


Figure 5.5: (a) Comparison of photobleaching of pegylated Cy5 containing core-shell silica nanoparticles to Cy5 free dye in aqueous solution under 3.5mW continuous excitation at 635nm. (b) Comparison of photobleaching of pegylated DY730 containing core-shell silica nanoparticles to DY730 free dye in aqueous solution under 530 microwatts continuous excitation at 635nm.

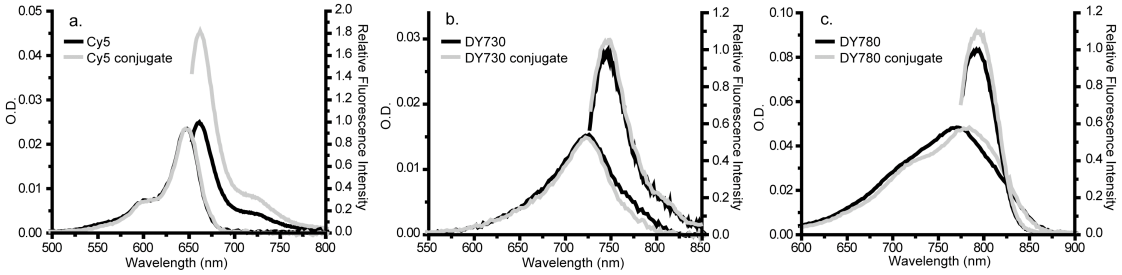


Figure 5.6: (a) Comparison of absorption matched Cy5 with maleimide functional groups and its conjugate with 4-mercapto-1-butanol in water; (b) DY730 with n-hydroxysuccinimidyl ester functional group and its 4-amino-1-butanol conjugate in water; (c) DY780 with maleimide functional group and its 4-mercapto-1-butanol conjugate in water.

that the parent zwitterionic dye produced the highest apparent enhancements in particles, over free dye in solution and that the enhancement decreased with increasing sulfonate substitutions. The ability to increase the brightness and photostability of NIR-emitting organic fluorophores by incorporation into hybrid silica nanoparticles, with 10nm sizes, paves the way towards high-efficiency probes for applications such as tagging and sensing in biological imaging, active photonic structures, and optical bar-coding. Moreover, higher apparent brightness values for incorporation of lower charged species suggests the use of less expensive precursor compounds to highly water soluble fluorophores and thus constitutes a significant advantage of silica nanoparticle over free dye approaches.

### *5.5 Acknowledgements*

Dyomics Gmbh graciously donated the DY dyes needed for this project. The authors thank the Army for funding through award number W911NF-06-C-0124, in collaboration with the NEI Corporation. Special thanks to the Cornell Center for Materials Research (CCMR) for facility support. Support for the CCMR is provided through the NSF Grant DMR 0520404, part of the NSF MRSEC Program. We thank the Cornell Nanobiotechnology Center for use of several of their facilities. U.W. is a cofounder of Hybrid Silica Technologies.

## REFERENCES


1. E. Herz, A. Burns, S. Lee, P. Sengupta, D. Bonner, H. Ow, C. Liddell, B. Baird and U. Wiesner, *Proceedings of SPIE*, 2006, **2006**, 6096-6108.
2. M. Han, X. Gao, J. Z. Su and S. Nie, *Nature Biotechnology*, 2001, **19**, 631-635.
3. A. Burns, H. Ow and U. Wiesner, *Chemical Society Reviews*, 2006, **35**, 1028-1042.
4. H. Xu, J. W. Aylott, R. Kopelman, T. J. Miller and M. A. Philbert, *Analytical Chemistry*, 2001, **73**, 4124-4133.
5. F. Tam, G. P. Goodrich, B. R. Johnson and N. J. Halas, *Nano Lett*, 2007, **7**, 496-501.
6. F. Stellacci, C. A. Bauer, T. Meyer-Friedrichsen, W. Wenselleers, S. R. Marder and J. W. Perry, *J. Am. Chem. Soc.*, 2002, **125**, 328-329.
7. R. B. Thompson, in *Topics in Fluorescence Spectroscopy*, ed. J. R. Lakowicz, Kluwer, New York, 2002, vol. 2, p. 360.
8. S. Kim, Y. T. Lim, E. G. Soltesz, A. M. D. Grand, J. Lee, A. Nakayama, J. A. Parker, T. Mihaljevic, R. G. Laurence, D. M. Dor, L. H. Cohn, M. G. Bawendi and J. V. Frangioni, *Nature Biotechnology*, 2003, **22**, 93-97.
9. H. Sun, A. M. Scharff-Poulsen, H. Gu and K. Almdal, *Chemistry of Materials*, 2006, **18**, 3381-3384.
10. C. Kirchner, T. Liedl, S. Kudera, T. Pellegrino, A. M. Javier, H. E. Gaub, S. Stölzle, N. Fertig and W. J. Parak, *Nano Lett*, 2005, **5**, 331-338.
11. A. M. Derfus, W. C. W. Chan and S. N. Bhatia, *Nano Lett*, 2004, **4**, 11-18.
12. A. v. Blaaderen and A. Vrij, *Langmuir*, 1992, **8**, 2921-2931.
13. C. Graf, W. Schartl, K. Fischer, N. Hugenberg and M. Schmidt, *Langmuir*, 1999, **15**, 6170-6180.

14. R. Nyffenegger, C. Quellet and J. Ricka, *Journal of Colloid and Interface Science*, 1993, **159**, 150-157.

15. F. Wang, W. B. Tan, Y. Zhang, W. Fan and M. Wang, *Nanotechnology*, 2006, **17**, R1-R13.

16. L. Wang and W. Tan, *Nano Lett*, 2006, **6**, 84-88.

17. A. Burns, P. Sengupta, T. Zedayko, B. Baird and U. Wiesner, *Small*, 2006, **2**, 723-726.

18. Y. Piao, A. Burns, J. Kim, U. Wiesner and T. Hyeon, *Advanced Functional Materials*, 2009, **18**, 3745-3758.

19. E. Rampazzo, S. Bonacchi, M. Montalti, L. Prodi and N. Zaccheroni, *Journal of the American Chemical Society*, 2007, **129**, 14251-14256.

20. D. R. Larson, H. Ow, H. D. Vishwasrao, A. A. Heikal, U. Wiesner and W.W.Webb, *Chemistry of Materials*, 2008, **20**, 2677.

21. H. Ow, D. R. Larson, M. Srivastava, B. A. Baird, W. W. Webb and U. Wiesner, *Nano Lett.*, 2005, **5**, 113-117.

22. A. Burns, J. Vider, H. Ow, E. Herz, O. Penate-Medina, M. Baumgart, S. M. Larson, U. Wiesner, M. Bradbury, *Nano Letters*, 2009, **9**, 442-448.

23. L. R. Hirsch, R. J. Stafford, J. A. Bankson, S. R. Sershen, B. Rivera, R. E. Price, J. D. Hazle, N. J. Halas and J. L. West, *PNAS*, 2003, **100**, 13549-13554.

24. E. Herz, T. Marchincin, L. Connelly, D. Bonner, A. Burns, S. Switalski and U. Wiesner, 2008, **in preparation**.

# CHAPTER 6

# PHOTOBLEACHING BEHAVIOR OF NEAR-INFRARED CORE-SHELL SILICA NANOPARTICLES


## *6.0 Abstract*

Near infrared probes are of increasing interest in bio-imaging applications because of the low autofluorescence and scattering background that is present in the near infrared spectral range. In this report we investigate the fluorescence photobleaching in water of core-shell silica nanoparticles (C dots) encapsulating the NIR dye Cy5 maleimide and comparing the kinetics of the photobleaching to the free dye in water. In both cases, the kinetics can best be described by a sum of a fast, stretched exponential and a slow, single exponential decay. While both bleaching components are also observed for the free NIR dyes in solution, the fast component is enhanced through dye encapsulation leading to anomalously fast particle bleaching behavior at short times. When compared to another NIR dye, DY730 succinimidyl ester, and particles derived from it, similar kinetics and kinetic changes upon encapsulation are observed. When compared to another cyanine dye, Cy3 maleimide in solution, this anomalously fast bleaching is not observed, but is present in particles derived from it. The fast component is attributed to photobleaching processes from strained, non-equilibrium conformations, which are emphasized through freezing-in of all dyes in the glassy silica matrix of the particles. Altogether, the observations reported upon here suggest powerful design criteria for creating more photostable NIR fluorescent silica nanoparticle probes for biological imaging including the use of rigid backbone based fluorescent dyes, post-synthesis densification of the silica nanoparticles and the use of dense surface coatings.

### *6.1 Introduction*

As light absorption and scattering in biological tissue decrease with increasing wavelength, fluorescence imaging has steadily been moving toward the near-infrared (NIR) spectral region (650-900nm) in an effort to increase the signal to noise ratio, contrast, and penetration depth available to tackle ever more challenging imaging problems in molecular imaging applications.[1,2] There are a large number of optical imaging probes that meet this spectral window. However, few are non-toxic, water soluble, and stable in biological media.[3-6] While in the last decade new NIR dyes have been introduced, fluorophore brightness and photostability are still areas of much needed improvement for providing more powerful biological imaging probes.[7]

In our recent work we have established that encapsulating fluorescent dyes within a core-shell silica nanoparticle matrix via a modified Stöber method leads to particles with narrow size distributions and provides significant improvements in per-dye brightness and photostability as compared to the free parent dye in aqueous solution.[1,8,9] We refer to these particles as C dots. By simultaneously reaching particle sizes down to the 3-6 nm range allows for efficient urinary excretion in animal studies, thereby paving the way for C dot applications in the emerging field of nanomedicine.[1,10] Building on the versatility of silica as a host material, the modularity of the core-shell architecture further suggests highly integrated "lab on a particle" architectures and "particle systems" that constitute promising clinically translatable materials platforms. [1,11,12]

At the same time that novel synthesis strategies and protocols for NIR fluorescent core-shell silica nanoparticles are developed,[13,14] thorough photophysical particle characterization studies have led to a better understanding of the key parameters for achieving dye brightness enhancements through silica encapsulation.[8,9,15] The silica matrix of the core separates the dyes, thereby

suppressing π-π stacking and energy transfer between neighboring dyes. Small changes in the internal particle architecture can lead to substantial enhancements of the quantum efficiency per dye as compared to the free dye in aqueous solution, which are due to an enhancement in the radiative rates and a reduction in the nonradiative rates of the encapsulated dyes. These studies have led to an effective methodology for selectively modifying the photophysical properties of fluorophores, thereby providing bright probes for biological and biomedical sensing, targeting and imaging applications.[10,11,16-18]

In contrast to the factors determining particle brightness, much less is known about the molecular origin and the detailed kinetics of photobleaching processes of (NIR) dyes encapsulated in silica nanoparticles. While a couple of recent reports concerning biological probes touch on comparative photobleaching of NIR free dyes and encapsulated dyes in either silica or calcium phosphate, there has been very little comprehensive research that elucidates key factors determining dye photostability in rigid silica particle matrices in aqueous solutions.[1,7] For long-time, high repetition / high intensity imaging, as is required for many *in vivo* biological imaging applications, such information is highly desirable, however. With the present paper we attempt to address this need by studying the photobleaching in water of ~20 nm sized fluorescent core-shell silica nanoparticles encapsulating Cy5, a NIR dye of the cyanine family emitting above 650 nm. Results on the detailed analysis of the photobleaching kinetics of these dots are compared to the behavior of the parent free dye as well as to densified (aged) particles and particles with a PEG-silane coating. Further cross experiments are performed with NIR DY730 dyes and dots as well as with Cy3 dyes (both also cyanine dyes) in order to elucidate the molecular origin of the observed bleaching behavior. As we will show, the ability to control photobleaching through silica nanoparticle architecture provides a powerful tool for the design of next

generation NIR fluorescent probes with enhanced photostability, inaccessible by the free dye in aqueous solution.

### *6.2 Experimental*

#### *6.2.1 Sample preparation and particle synthesis*

The particle synthesis of similar particles has been reported upon previously.[1] Briefly, 1 milligram of DY730 succinimidyl ester (Dyomics), Cy5 maleimide (GE Healthsciences), or Cy3 maleimide dye (GE Healthsciences) was dissolved in 1mL of dimethylsulfoxide (DMSO) in a nitrogen filled glovebox and allowed to mix for at least 1 hour to produce a stock dye solution for either the synthesis of particles or for spectroscopic comparison to particles. For example, for a 15mL Cy5 maleimide synthesis, 221 microliters of the dye solution was mixed with 2.53 microliters of 3-mercaptopropyltrimethoxysilane (or 3-aminopropyltriethoxysilane for the DY730 succinimidyl ester), in a 50:1 dye to silane ratio. The structures of the dyes and silanes used in this report, as well as the resulting conjugates for Cy5 and DY730 are shown in Figure 6.1 together with absorption and emission spectra of the free dyes in aqueous solution.[19] The conjugated dye solution was removed from the glovebox and added to a Stöber-type basic ethanol solution composed of 1.5mL of 2.0M ammonia in ethanol (Sigma Alrdrich) added to 12mL of ethanol in addition to 231 microliters of water mixing at a rate above 1000rpm in a 50mL round bottom or Erlenmeyer flask to insure fast, complete mixing. Once the conjugated dye was well mixed in the solution 167 microliters of tetraethylorthosilicate (Sigma Aldrich) was added and allowed to react for 8 hours in order to form the cores. Once the cores were formed, addition of 360

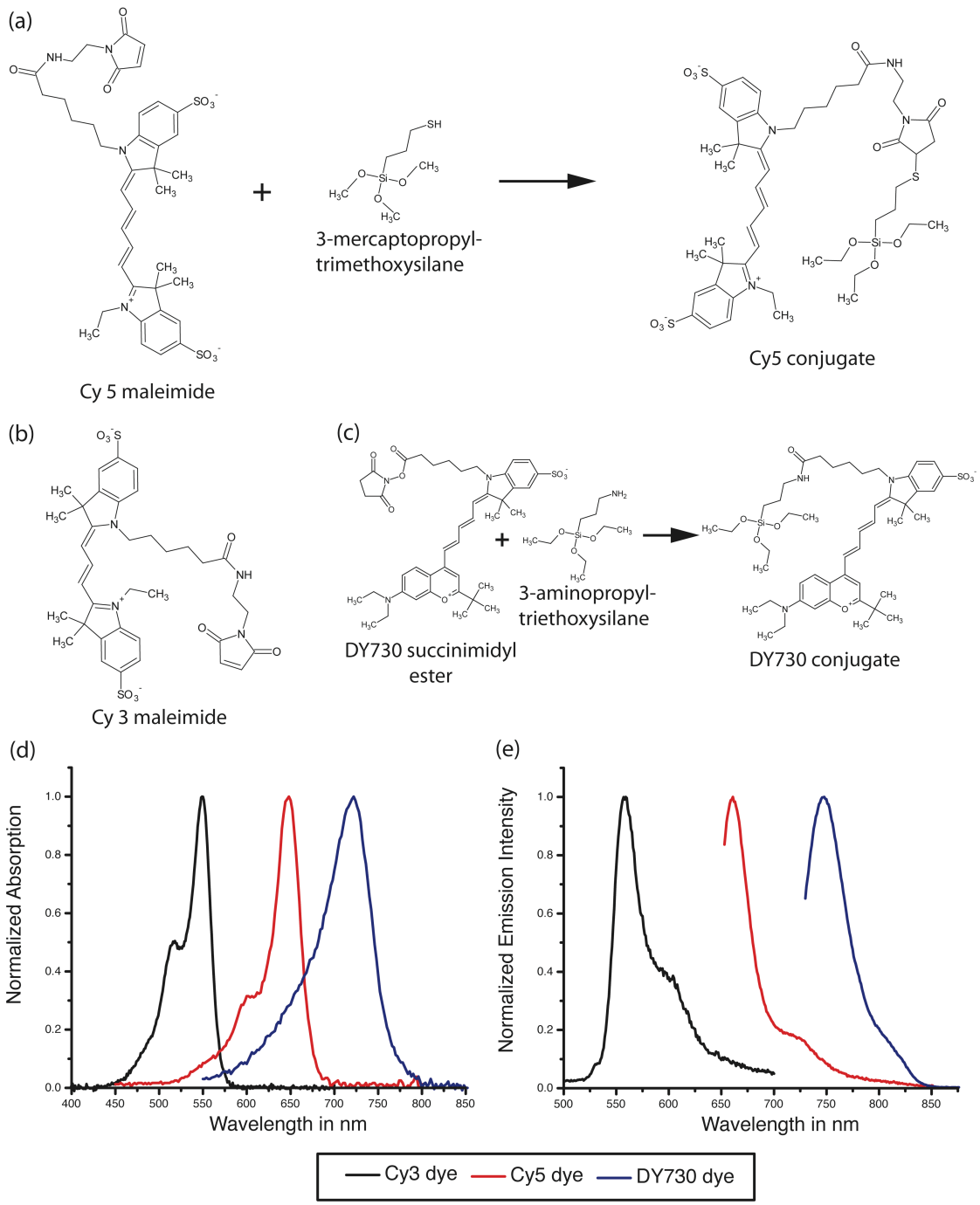


Figure 6.1: (a) Dye structure and conjugation reaction schematic for Cy5 maleimide and 3-mercaptopropyltrimethoxysilane, (b) dye structure for Cy3 maleimide, (c) Dye structure and conjugation reaction schematic for DY730 succinimidyl ester and 3-aminopropyltriethoxysilane, normalized plots of (d) absorption and (e) emission spectra of Cy3, Cy5, and DY730 dye in aqueous solution.

microliters in equal aliquots at equal time intervals over a period of 6 hours produced a pure silica shell around the core and achieved the desired size of ~20nm in diameter.

### *6.2.2 Particle densification*

Densification of the Cy5 particles was carried out using the as made particle reaction solution of standard core-shell silica nanoparticles and heating it to 58 °C in a Parr-Bomb apparatus in a temperature controlled oven for 9 hours. The densified particles were subsequently dialysed to pure ethanol using Snakeskin dialysis tubing, 3500MWCO (Thermo-Fisher Scientific), and a ratio of 1mL of as synthesized sample to ~1000mL of ethanol for 8 hours, after which they were stored for further experiments.

### *6.2.3 Fluorescence Correlation Spectroscopy*

To prepare samples for fluorescence correlation spectroscopy, FCS, the particles were dialyzed to water using the protocol and dialysis tubing described above for ethanol. After dialysis, samples were absorption matched to free dye (a small aliquot of the free dye in DMSO was diluted over 100 fold in water), at the appropriate laser excitation wavelength (488nm or 635nm), in 18.2 MΩ/cm deionized water (deionized by a Millipore Synthesis system), using a Varian Cary 5000 dual beam spectrophotometer and 1cm path length quartz cuvettes, with pure deionized water as the background reference.

A lab-built fluorescence correlation spectroscopy apparatus with a confocal configuration, a schematic of which is shown in Appendix B, was used to determine dye / particle size, particle size variations after processing, and per dye / particle brightness. For the Cy5 and DY730 dyes a 635nm diode laser (Power Technology)

was used for excitation. A 488nm diode pumped solid state laser (Newport) was used for excitation of the Cy3 dye. The excitation beam was reflected up at the sample by an excitation/emission dichroic (Chroma z488/633rpc, a polychroic with a reflection band for 488nm and 635nm and a pass band for the emissions of the dyes used), through the 60X Olympus UPlanSAPO, 1.2NA water immersion objective. A 100 microliter sample at nanomolar concentrations was placed in a microwell dish with a No. 1.5 coverslip bottom (MatTek P35G-1.5-7-C). The dyes in the sample emitted fluorescent light, which, once collected by the objective, passed through the excitation/emission dichroic and was reflected into a focusing lens by the emission mirror. The emission light was focused through a long-pass filter (Chroma) to remove any remaining excitation light and collect only emission photons. A 50 micron pinhole was used to axially limit the effective volume from which fluorescence is collected and to clean up the beam by limiting entry of scattered light into the detector, thereby increasing the signal to noise ratio.[20,21] The light then passed through a second lens and into a Perkin Elmer (SPCM 14) avalanche photodiode detector. An autocorrelator card from Correlator.com was used to process the output from the avalanche photodiode detector to provide both intensity trace data and autocorrelation data. All data were collected in 3 sets each consisting of 5 one-minute runs and averaged, with a standard deviation calculated for every delay time.

From the intensity trace data the per-focal volume brightness was determined as an average of the bin intensity (in counts per second) over the full collection time. From the per-focal volume brightness, per-particle or per-dye brightness values were calculated using the number of particles or dyes in the focal volume, N, which was obtained from a fit of the autocorrelation data. Due to the well-known presence of triplet in the emission of Cy5 and other cyanine dyes, and the short delay time artifacts

that triplets cause, the FCS autocorrelation data were fit using a triplet corrected autocorrelation function, G(τ), as shown in Equation 1 in analytical form. [22-24]

$$G(\tau) = 1 + \left(\frac{1}{N}\right) \times \left(1 - A + A \times \exp\left(\frac{t}{\tau_R}\right)\right) \times \left(\frac{1}{\left(1 + \frac{t}{\tau_D}\right)}\right) \times \left(\frac{1}{\sqrt{\left(1 + \frac{t}{\tau_D} s^2\right)}}\right) \qquad Eq.1$$

Here A is the amplitude of the triplet correction, $\tau_R$ is the apparent diffusion time of molecules or particles in the triplet state, and $\tau_D$ is the diffusion time of the molecule or particle in the singlet state. The number of molecules per focal volume is N and the structure factor parameter that describes the three-dimensional Gaussian focal volume in terms of a ratio of the axial to the radial axis is termed s and was calculated using a standard dye, as described below.

The radial radius, $r_0$, of the 3-D Gaussian focal volume was calculated daily employing a standard dye with known literature values of the diffusion constant in water or a suitable alternative that was matched to the literature values using Equation 2.[25] Hence, for all 635nm excitation based FCS work, the instrument was calibrated to Alexa Fluor 647 maleimide in water, a suitable (more stable against aggregation) alternative to Alexa Fluor 633 and matched to within 5% for the diffusion constant in literature for AF633, which is $3.0 \times 10^{-6}$ $cm^2/s$.[26]

$$D = \frac{r_0^2}{4\tau_D} \qquad Eq.2$$

After the radial radius, $r_0$, of the 3-D Gaussian focal volume was standardized, it was used, along with $\tau_D$ from the fit of Equation 1 to the autocorrelation data, to calculate the diffusion constant, D, of the sample of interest, using Equation 2. [25] From D and the Stokes-Einstein equation, Equation 3, the particle hydrodynamic radii, $r_{hydrodynamic}$, were calculated.

$$r_{hydrodynamic} = \frac{kT}{6\pi\eta D} \qquad Eq.3$$

Here k is the Boltzman constant in appropriate units, T is the sample temperature in Kelvin (assumed to be the temperature in the room), and $\eta$ is the viscosity of the sample solution (taken to be the viscosity of water, 8.9 x$10^{-3}$ dynes/cm$^2$ as the particle or dye concentrations were in the nanomolar regime).

### *6.2.4 Photobleaching experiments*

For photobleaching experiments dye and particle samples were absorption matched (see FCS measurements) such that the absorption at the excitation wavelength was less than 0.1 OD. A two microliter droplet of absorption matched sample was drawn into a 0.4 mm inner diameter glass capillary, providing approximately 1.5cm of pathlength through the sample, and placed into a custom 3-axis tilt holder. For photobleaching the objective on the FCS instrument was switched to a 3.5X 0.10NA objective. The capillary was aligned with the laser beam by the back-reflection of the top meniscus of the sample within the capillary and by maximizing the fluorescence intensity collected by the FCS detector. For alignment, low laser power was used. For the photobleaching experiments comparing Cy5 and DY730 dyes and particles 0.6mW laser power was used while for pegylated Cy5 particle comparisons 3.5mW was used. For Cy3 dye the photobleaching was carried out using a much higher laser power of 38mW because the 488nm excitation was so far from the peak absorption of the molecule that the absorption efficiency was very low. The emission was collected in the same confocal manner as for FCS and measured with the same avalanche photodiode, with an appropriate neutral density filter in front of it when the fluorescence was too bright (i.e. for Cy3). Once aligned at low intensity, the laser beam was blocked, the laser adjusted to high intensity, the detector restarted and the beam block removed. For Cy5 and DY730 dyes and

particles, the collection time was 20 minutes, with 2.5s data collection intervals. For the Cy3 dye the collection time was 1 hour with 7.5s intervals. All data was collected in triplicate to insure repeatability. The photobleaching traces were collected by the correlator card and exported to Origin 8 for fitting using a standard nonlinear least squares algorithm.

For analysis, the photobleaching data sets were normalized to the initial, maximum, intensities. All data were then fit with three different fit functions, see Eqs. 4, 5, and 6: (i) a stretched exponential or Kohlrausch-Williams-Watts (KWW) function (Eq. 4) containing a parameter, $\beta$, that can take on values, $0 < \beta \leq 1$, and is interpreted in terms of a distribution of relaxation times [27]; (ii) a double exponential function (Eq. 5); and (iii) a stretched exponential plus a single exponential function (Eq.6).

$$y = A_1 \exp\left(\frac{-x}{\tau_1}\right)^{\beta} + y_0 \qquad Eq.4$$

$$y = A_1 \exp\left(\frac{-x}{\tau_1}\right) + A_2 \exp\left(\frac{-x}{\tau_2}\right) + y_0 \qquad Eq.5$$

$$y = A_1 \exp\left(\frac{-x}{\tau_1}\right)^{\beta} + A_2 \exp\left(\frac{-x}{\tau_2}\right) + y_0 \qquad Eq.6$$

The parameter, $y_0$, in all fitting functions represents the background scattering.

### *6.3 Results*

#### *6.3.1 Results of Fluorescence Correlation Spectroscopy Studies.*

In this paper photobleaching studies were focused on Cy5 based fluorescent core-shell silica nanoparticles synthesized according to the protocol described in the experimental section. The structure of the commercially available maleimido derivative of this dye together with the conjugation chemistry to convert it to a silane species that can be covalently conjugated to the silica network of the core-shell silica nanoparticle is shown in Figure 6.1a. After particle synthesis, FCS was used to investigate particle size, particle solution concentration, and per-particle brightness in comparison to the parent free dye in aqueous solutions. In Figure 6.2, representative examples of FCS autocorrelation data, averaged over fifteen runs per sample, are shown with resulting standard deviation for particles and parent Cy5 dye, together with fits using a triplet corrected autocorrelation function, see Eq. 1. From the autocorrelation data, as expected, the dye diffuses through the focal volume significantly faster than the particle, leading to a faster decay of the correlation. From the fits, which nicely describe the data, and the resulting diffusion times, $\tau_D$, the hydrodynamic radii of dyes and particles can be calculated using Eqs. 2 and 3. Results, together with brightness values, are summarized in Table 6.1, which also lists the size of the reference dye Alexa Fluor 647. The Cy5 based C dots are 11 nm in radius and are about four times as bright as the parent free dye. This brightness enhancement can be rationalized as a combination of the per-dye enhancement due to dye encapsulation in the rigid silica matrix with the incorporation of multiple dyes into the same particle as quantitatively analyzed for TRITC containing dots in a recent publication.[8] It should be pointed out that in the present study we did not attempt to optimize particle brightness for any of the particles investigated by incorporating, e.g. the maximum number of dyes into the particles for a given particle size without seeing energy

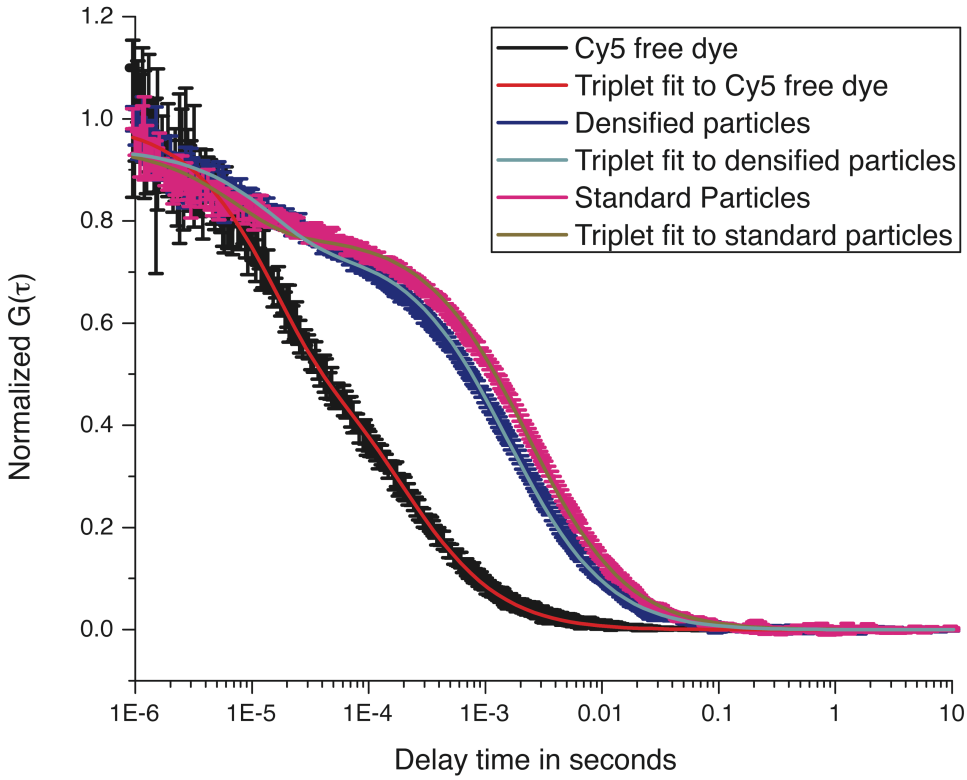


Figure 6.2: Normalized average FCS autocorrelation data for 5 one minute runs of Cy5 maleimide dye, standard core-shell silica nanoparticles, and densified core-shell silica nanoparticles. The error bars show the first standard deviation and the solid line overlays show the fits of the data using Equation 1. The standard particles are larger than the densified particles.

Table 6.1: Core-shell silica nanoparticle size and brightness values as calculated from FCS autocorrelation data.

| Sample | Hydrodynamic radius (nm) | Per-probe brightness (thousand counts per second) |
|---|---|---|
| Cy5 maleimide free dye | 0.9 | 3.5 |
| Standard Cy5 core-shell nanoparticles | 11 | 12.4 |
| Densified Cy5 core-shell nanoparticles | 7.7 | 11.1 |
| DY730 succinimidyl ester dye | 0.6 | 0.8 |
| Standard DY730 core-shell nanoparticles | 5 | 1.5 |
| AF647 maleimide dye | 0.80 | --- |

transfer between dyes. Instead the focus was on the photobleaching behavior for which absolute brightness considerations were secondary.

In addition to dye and standard fluorescent core-shell silica nanoparticles we also wanted to study the photobleaching behavior of densified or aged nanoparticles. We speculated that particle densification could lower the accessibility of the dyes in the silica matrix for species like oxygen, that accelerate photobleaching, thus improving dye photostability. To this end the standard Cy5 particles were heat-treated in their synthesis reaction solution for 9 hours at 58°C in a Parr-Bomb apparatus as described in the experimental section. Such post-synthesis densification processes are well known in ceramic processing as aging or heat/pressure induced densification, whereby the heat or pressure is used to drive the dangling silanol bonds in the silica matrix to more fully condense to cross-linked $SiO_2$.[28] When condensation occurs, the fractal nature of the matrix compacts, leading to a decrease in the hydrodynamic size of the particles.[29] In aerogel and xerogel processing this matrix compaction is known as shrinkage.[28] Results of FCS measurements on densified Cy5 particles are also shown in Figure 6.2. Indeed, as expected the correlation for these aged particles drops faster than that of the standard particles, implying a smaller size. A fit of these data and analysis (see Table 6.1) showed a 30% decrease in particle radius through the densification from 11 nm for the standard Cy5 particles to 7.7 nm for the densified dots, which we interpret as an increase in the density of the sol gel silica matrix during heat/pressure treatment. In contrast to the size, the densification process only marginally affected particle brightness, see Table 6.1.

### *6.3.2 Results of Photobleaching Studies.*

After characterizing free dye, standard, and densified particles using FCS, photobleaching experiments were performed on absorption matched aqueous solutions

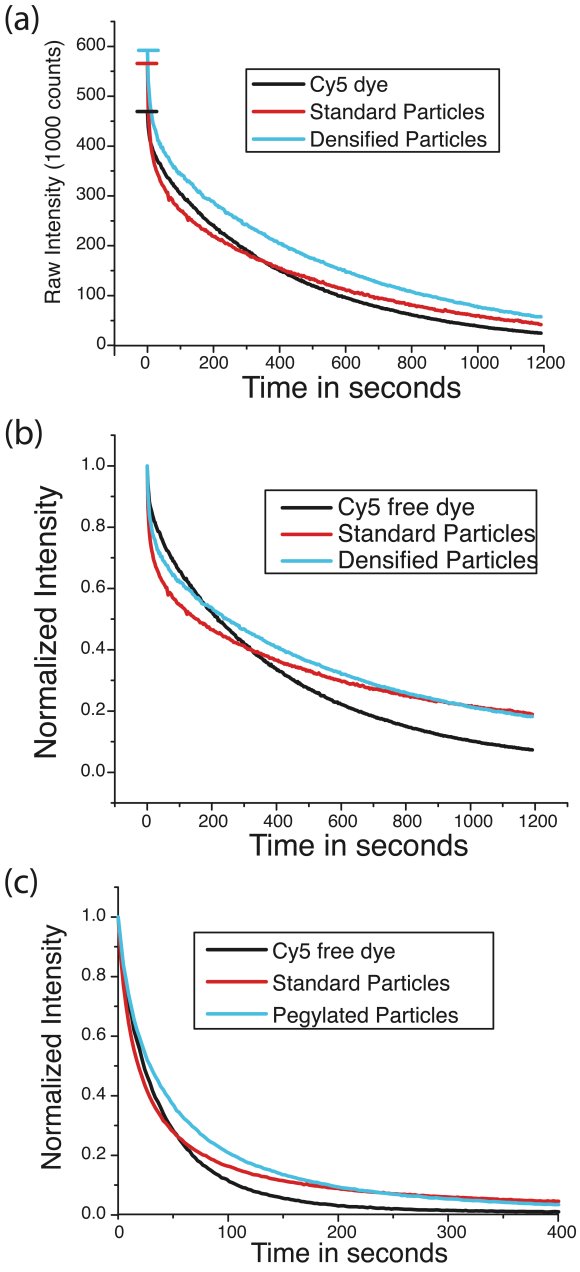


Figure 6.3: (a) Raw fluorescence intensity measuring photobleaching as a function of time for Cy5 free dye, standard and densified Cy5 containing particles, showing that both dye and particles have a fast and slow component in their respective photobleaching behavior. (b) Normalized fluorescence intensity data of (a). (c) Normalized photobleaching plots for Cy5 free dye, standard Cy5 containing core-shell silica nanoparticles, and Cy5 containing core-shell silica nanoparticles that have had a PEG-silane added to the surface. The particles that have a PEG-silane coating photobleach less quickly than both the dye and uncoated particles. Data in (a) and (b) were taken with 0.6mW laser power while data in (c) were taken at 3.5mW.

of all three species using a protocol described in the experimental section. By employing a capillary set up it was ensured that the laser beam affected the entire sample volume, thus eliminating diffusion-based artifacts in the bleaching data sets. Figure 6.3a displays plots of raw counts per second as a function of bleaching time for representative twenty minute runs of Cy5 dye, standard and densified particles, respectively. The horizontal bars at the beginning of each run show the different start intensities to the curve at zero time. Surprisingly, comparison of the data for free dye and standard core-shell silica particles suggests that initially, the particles bleach faster than the free dye. It is not until after about the first five minutes (about 300 seconds) that the bleaching curve of the free dye undercuts that of the particles and displays faster bleaching as one would have initially expected. This is even more evident from a normalized data plot, as shown in Figure 6.3b. The curve for the densified particles shows slower bleaching over the entire time window studied. A similar effect, i.e. slower photobleaching over most of the studied time window, can alternatively be achieved by PEGylating the standard Cy5 based core-shell silica nanoparticles (Figure 6.3c) with a PEG-silane (Gelest SIM6492.7) as described in previous publications,[1,15] which only adds ~2nm to the total hydrodynamic diameter of the particles as was checked by FCS (data not shown). Please note that higher laser intensity was used for the acquisition of the data set in Figure 6.3c (as described in the experimental section), thus it shows a much accelerated photobleaching behavior. Hence, the time scale for the standard particle experiments was 1200s (20 minutes), while for the PEG silane particles it was just 400s (or just over 6.5 minutes).

In order to investigate these trends in a more quantitative way, as described in the experimental section, the respective data sets for Cy5, standard, and densified Cy5 particles were normalized to their initial values and the resulting curves were fitted with three types of fitting functions, shown in Eqs. 4, 5, and 6, using a standard

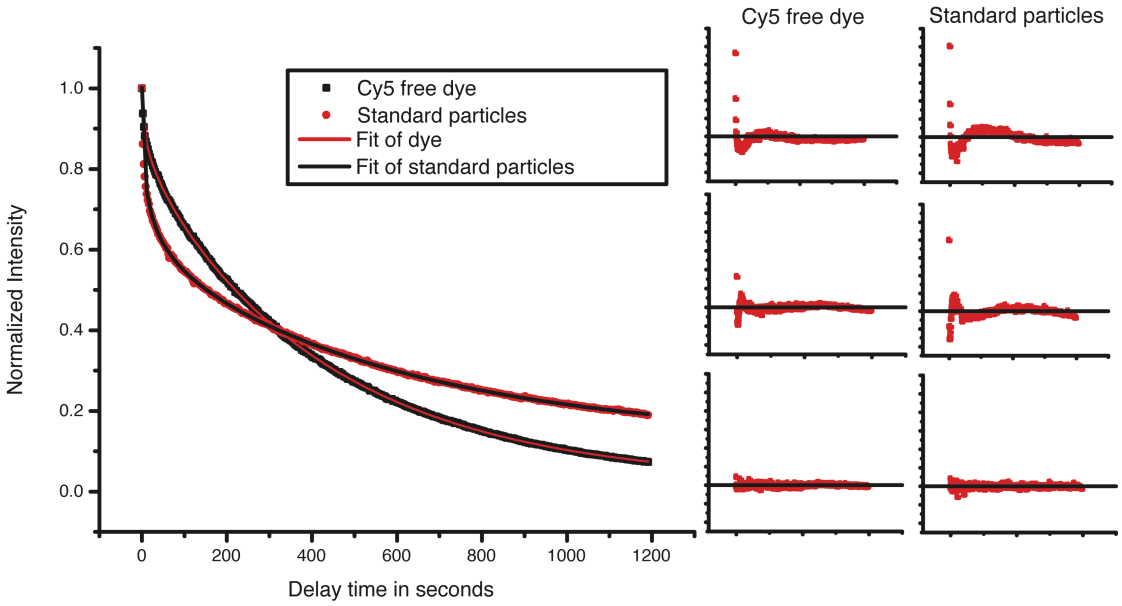


Figure 6.4: Left: Fluorescent photobleaching data and best fits for Cy5 free dye and standard Cy5 containing core-shell silica nanoparticles. Right: Residuals of fits with, from top to bottom, a stretched exponential (Eq. 4), a double exponential (Eq. 5), and a stretched plus single exponential (Eq.6) for Cy5 free dye and standard Cy5 containing core-shell silica nanoparticles in the left and right columns, respectively. The horizontal time axis for the residual plots is the same as for the data on the left and the vertical axes are plotted from -0.05 to 0.12, with zero demarcated by a horizontal line.

nonlinear least squares fit routine: (i) a stretched exponential or Kohlrausch-Williams-Watts (KWW) function (Eq. 4); (ii) a double exponential function (Eq. 5); and (iii) a stretched exponential plus a single exponential function (Eq.6). For Cy5 dye and standard particles, examples of best fits to the normalized photobleaching data are shown on the left of Figure 6.4, further emphasizing that initially the particles bleach faster than the free dye. On the right side of the same figure for both data sets, residuals are plotted for all three fitting functions (from top to bottom: stretched exponential, double exponential, stretched plus single exponential). The horizontal time axis is the same for all plots in this figure. For the residual plots the vertical axes have a range from -0.05 to 0.12, with zero demarcated by a horizontal line. From these residual plots it is evident that Eq. 6, i.e. a sum of stretched and single exponentials (plus background), fits both data sets best, as all other fits show systematic deviations from the data.

Results of the fits to Eq.6 in terms of amplitudes, characteristic decay times, and $\beta$ parameters are summarized for Cy5 dye and standard particles (as well as the densified particles) in Table 6.2. For the stretched exponential in Eq. 6 rather than the characteristic decay times, $\tau_1$, the mean decay times, $<\tau_1>$, are depicted in Table 6.2, which can be calculated as the first moment of the underlying distribution function of decay times from the fitting parameters $\tau$ and $\beta$ according to Eq. 7 [30].

$$\langle \tau \rangle = \frac{\tau}{\beta} \Gamma\left(\frac{1}{\beta}\right) \qquad Eq.7$$

Here $\Gamma$ is the standard gamma function. As the results displayed in Figure 6.4 and Table 6.2 suggest, both the Cy5 dye as well as the Cy5 dye-based particles have two photobleaching components under laser illumination, a fast one and a slow one, which have well separated decay constants (tens versus hundreds of seconds for the fast and

Table 6.2: Amplitudes and characteristic decay times for Cy5 free dye, standard core-shell silica nanoparticle, and densified core-shell silica nanoparticle photobleaching fits using Equation 6. Cy5 data clearly show an increase in $A_1$ going from free dye to standard particles and then a decrease upon densification of the particles. Note for all cases: The background, $y_0$, was determined in independent fits, subtracted from the dataset and the data refit so that the magnitudes of the individual decay amplitudes sum to one. Refitting did not change the other fitting parameters.

| Sample | $\beta$ | $\langle\tau_1\rangle$ | $A_1$ | $\tau_2$ | $A_2$ |
|---|---|---|---|---|---|
| Cy5 maleimide free dye | 0.48 | 32 | 0.20 | 442 | 0.80 |
| Standard CY5 nanoparticles | 0.47 | 36 | 0.49 | 629 | 0.51 |
| Densified CY5 nanoparticles | 0.55 | 25 | 0.34 | 620 | 0.66 |
| Cy3 maleimide free dye | --- | --- | ---- | 1110 | 1.00 |

slow component, respectively). Furthermore, encapsulation within the core-shell silica matrix of the standard particle leads to an increase of the amplitude of the fast process by more than a factor of two while the $\beta$ parameter remains at approximately 0.5. The decay time of the slow process becomes significantly longer, increasing by about 50% compared to the free dye. Finally, the particle densification process leads to a decrease of the amplitude of the fast component by more than 25% relative to the standard particle and resumption of the dominance of the long component, as in the case of the free dye.

### *6.3.3 Results of Photobleaching Cross Experiments.*

In order to elucidate the origin of the two bleaching components observed for Cy5, we also looked at the photobleaching behavior of the maleimido derivative of Cy3 free dye. This dye has a shorter, three carbon-containing bridge (as opposed to a five carbon-containing bridge for Cy5, see Figure 6.1b), connecting the two condensed ring systems, but is otherwise identical to Cy5. When the Cy3 derivative is photobleached in aqueous solution with a 488nm diode-pumped solid-state laser with 38mW at the sample, the resulting data set can be fitted rather well with a single exponential fit function, as shown in Figure 6.5. The single exponential has a characteristic decay time of about a thousand seconds ($\tau$ is 1110s), thus suggesting that only a slow photobleaching component is observed for this dye while a fast component is absent. Obviously dye architecture has a strong effect on the photobleaching kinetics.

Finally, in order to check whether the existence of a fast photobleaching component is unique to Cy5 in solution or is also present in other NIR cyanine dyes with a five carbon-containing bridge between the condensed ring systems but with different substituent groups, we studied the photobleaching behavior of DY730

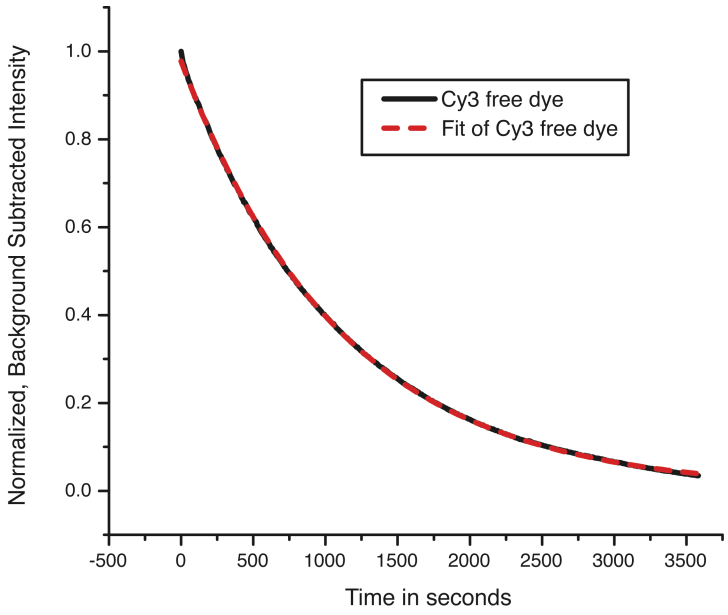


Figure 6.5: Normalized and background subtracted photobleaching trace for Cy3 maleimide free dye in aqueous solution with a single exponential fit.

succinimidyl ester and standard core-shell silica nanoparticles derived from it. The dye structure together with the conjugation chemistry to convert it to a silane species that can be covalently conjugated to the silica network of the silica nanoparticle is shown in Figure 6.1c. The normalized photobleaching data for dye and standard particles are shown in Figure 6.6. While the details of the kinetics are different when compared to the Cy5 dye and particles, the results clearly show that (i) for both, DY730 succinimidyl ester and standard particles derived from it, a fast and a slow bleaching component is present, and that (ii) through encapsulation the fast component is emphasized (see inset of Figure 6.6). Furthermore, upon pegylation with the PEG-silane, the particles also bleached slower than the dye and standard DY730 particles (data not shown), thus exhibiting the same trends as the Cy5 particles.

### *6.4 Discussion.*

Previous studies on fluorescent dyes indicate that there are a number of mechanisms that can account for photobleaching, depending on pump power, the presence of dissolved oxygen, and the fraction of dyes that are in the triplet state.[31] The presence of oxygen has both beneficial and detrimental effects. Oxygen has been shown to be a strong quencher of dye triplet states, enhancing lasing intensities in dye lasers and otherwise increasing the number of photons emitted by a single molecule.[32-34] However, oxygen is commonly known to act as a promoter of photobleaching when in the highly reactive singlet state where it can react with either excited state or ground state dye molecules, destroying their fluorescence. [35,36] Hence, there may be a balance between oxygen contributions to a lower triplet population and a higher photodecomposition yield.[23]

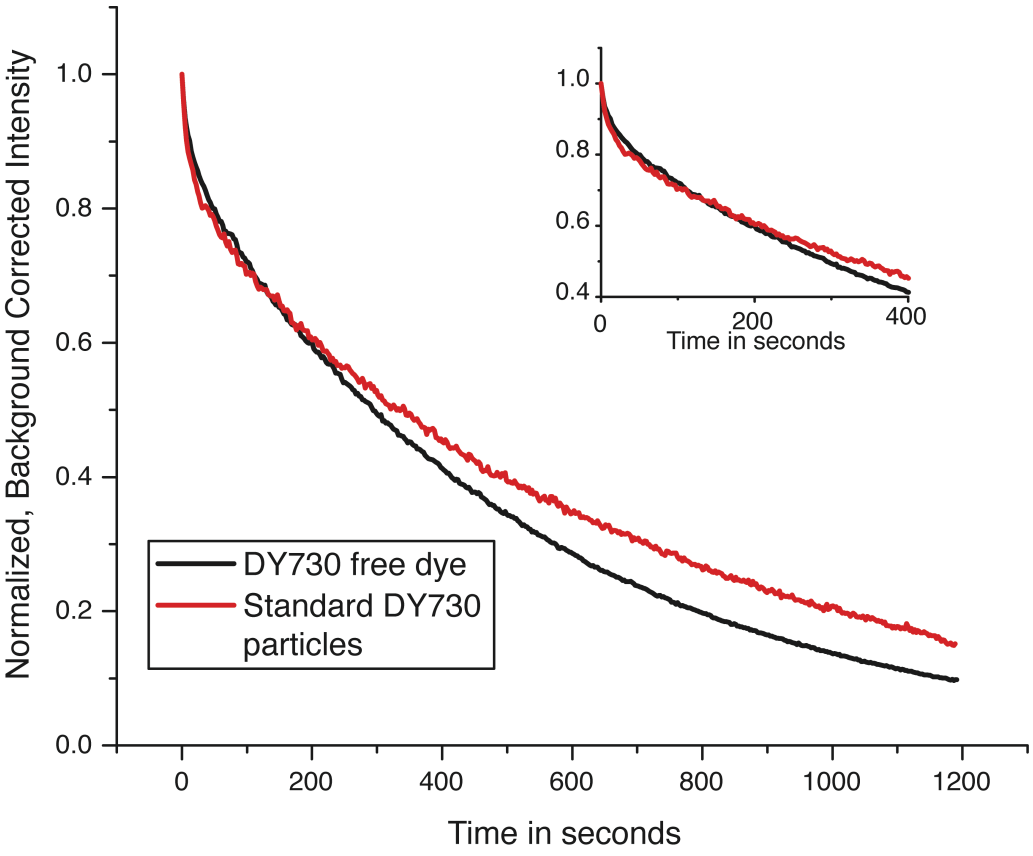


Figure 6.6: Normalized and background subtracted photobleaching traces for absorption matched DY730 succinimidul ester free dye and standard DY730 containing core-shell silica nanoparticles in water.

Generally past studies of homogeneously dissolved dye solutions by spectroscopic methods yielded single-exponential photobleaching observations.[37] Several studies have found that photobleaching is likely not just a photo-oxidative phenomenon or, alternatively, is tremendously sensitive to any residual dissolved oxygen that remained after de-oxygenation.[37-39] Finally, Song and co-workers found that under microscopy conditions photobleaching of *bound* flourescein molecules was not described well by a single exponential.[37]

In our studies on the photobleaching behavior of NIR fluorescent core-shell silica nanoparticles containing covalently bound organic dyes we observed a fast, stretch exponential and a slow, single exponential decay. The slow, single exponential decay components, observed in the photobleaching upon intense laser illumination in aqueous solution of the cyanine dyes and particles derived from them, may represent regular photo-oxidative processes that are seen in various dye families.[37,40-42]

The fast photobleaching component is observed in both Cy5 and DY730 dyes and particles, i.e. for dyes with a five carbon-containing bridge between the two condensed ring systems and irrespective of the details of the substituent groups. The fast component disappears when going over to Cy3 free dye in solution, a cyanine dye with only a three carbon-containing bridge. Furthermore, from fits of the Cy5 data sets the amplitude of the fast component and thus its importance increases when the dye is encapsulated in the rigid, glassy silica matrix, consistent with data on DY730.

Fast, anomalous relaxation behavior of dyes encapsulated in glassy matrices is a well-studied phenomenon.[43-45] For example, in earlier investigations of photoinduced isomerization of azobenzene covalently coupled to a polymer matrix and studied below the glass transition temperature of the polymer, one of the co-authors of this paper showed the existence of anomalously fast relaxation components characterized by a broad distribution of relaxation times absent in solution and in addition to a

"normal" component that was expected from isomerization studies in solution.[46] In the case of azobenzene these fast relaxation components are believed to be associated with strained dye conformations frozen in the glassy state of the polymer matrix and which, upon excitation, relax anomalously fast. Since a glass is a heterogeneous environment the characteristic relaxation times of the anomalously fast components were broadly distributed as reflected by low $\beta$ parameters ($\beta \approx 0.15$) in fits with stretched exponentials.

In analogy to the azobenzene case here we hypothesize that the short time scale, fast photobleaching process observed for NIR Cy5 dyes and particles (as well as for NIR DY730 dyes and particles), modeled with the stretched exponential term to indicate a spread of decay times, stems from non-equilibrium conformations of the dye, which photobleach more readily from the excited state of the molecule, even in solution. These non-equilibrium conformations are substantially accentuated upon dye encapsulation within the silica particles where strained conformations get frozen-in in the glassy state of the silica matrix. The long carbon bridge that in NIR cyanine dyes connects the two condensed ring systems, albeit stiffened through the π-electron delocalization, can be expected in solution to lead to significant large-amplitude conformational fluctuations around the flat equilibrium dye conformation. This means that the dye statistically spends a significant amount of time while in solution in strained conformations. When irradiated with light the molecule instantaneously gets excited into a higher electronic state, on time scales much faster than the conformational transitions. Subsequent photodegradation mechanisms may thus often start from such strained, non-equilibrium conformations, thus leading to anomalously fast bleaching kinetics. When the dye is encapsulated in the silica matrix of the core-shell silica nanoparticles, in analogy to the azobenzene case, more of these strained,

non-equilibrium conformations are populated and frozen-in in the silica glass, leading to the observed increase in amplitude of the fast photobleaching component.

When the Cy5 particles are densified, the amplitude of the fast component is reduced by more than 25% relative to the standard particle and the long component resumes its dominance. This suggests that the heating process, through a reorganization of the silica matrix surrounding the dye molecules as indicated by the particle size decrease, allows relaxation of some of the strained dye conformations. Alternatively, the heating process may also decrease the porosity in the sol-gel silica matrix enough that water with oxygen dissolved in it has less access to the dyes, leading to a slowing of the degradation processes.

That decreased particle porosity is at least in part responsible for a slow down of the degradation kinetics is supported by the observation that slower photobleaching over the studied time window is alternatively achieved by PEGylating the standard Cy5 based core-shell silica nanoparticles with a PEG-silane (Figure 6.3b). The PEG-coating may lead to a very thin but dense silica-type layer on the particle surface which may help to seal some of the matrix pores, thus again reducing access of water containing dissolved oxygen to the dyes.

### *6.5 Conclusions*

In this report we have demonstrated that fluorescent core-shell silica nanoparticles (C dots) encapsulating the NIR dyes Cy5 maleimide and DY730 succinimidyl ester undergo photobleaching in water that can best be described by a sum of a fast, stretched exponential and a slow, single exponential decay. While both bleaching components are also observed for the free NIR dyes in solution, surprisingly the fast component is enhanced through dye encapsulation, leading to anomalously fast particle bleaching behavior at short times. This anomalously fast bleaching is not

observed for Cy3 maleimide in solution. The fast component is attributed to photobleaching processes from strained, non-equilibrium conformations already present in solution for only the NIR dyes, which are emphasized through freezing-in of all dyes in the glassy silica matrix of the particles. The strained conformations may be due to large amplitude structure fluctuations induced by the long carbon bridge connecting the two condensed ring systems in NIR cyanine dyes leading to "floppy" structure characteristics in solution. Slowing of the photobleaching kinetics is observed when standard Cy5-based nanoparticles are densified through a post-synthesis heat treatment, leading to a reduction of the amplitude of the fast process, possibly due to a relaxation of strained dye conformations during rearrangements of the silica matrix upon heating. Furthermore, the particle photobleaching rate can be slowed by PEGylating the standard Cy5 particles using a PEG-silane coating, suggesting that reducing accessibility to the dye of water containing dissolved oxygen may also be a valid mechanism leading to a slowing of the photobleaching in NIR fluorescent core-shell silica nanoparticles. Altogether, the observations reported upon here suggest powerful design criteria for creating next-generation, more photostable NIR fluorescent silica nanoparticle probes for biological imaging including the use of rigid backbone based fluorescent dyes, post-synthesis densification of the silica nanoparticles and the use of dense surface coatings.

### *6.6 Acknowledgements*

A special thank you to Jason Dorvee and Prof. Laura Estroff for allowing us to use their Parr-Bomb apparatus and for great discussion. The authors thank the Army for funding through award number W911NF-06-C-0124, in collaboration with the NEI Corporation. We acknowledge the Cornell Center for Materials Research (CCMR) for facility support. Support for the CCMR is provided through the NSF Grant DMR 0520404, part of the NSF MRSEC Program. We thank the Cornell Nanobitechnology Center for use of several of their facilities. U.W. is a cofounder of Hybrid Silica Technologies.

# APPENDIX B

# FLUORESCENCE CORRELATION SPECTROSCOPY INSTRUMENTATION AND USERS MANUAL

## *B1.0 Brief History and Introduction to Fluorescence Correlation Spectroscsopy*

The invention of fluorescence correlation spectroscopy (FCS) in the 1970s, at Cornell by the Webb group and by a group at the Karolinska Institute in Sweden, has built on the concepts of fluctuation correlation spectroscopy and allowed for the in-depth investigation of biomolecular processes at the single molecular level [47-50]. More recently, in the 1990s, the technique benefited from significant advances in confocal optics, sensitive photon detectors, and fast data processing tools [51,52]. With additional refinements in the organic dyes used as markers for biomolecules, increases in the quantum yields and photobleaching resistance were possible, allowing for higher emissions for longer periods of time from samples of interest. The higher number of photons available significantly enhanced the signal to noise ratio of the FCS measurements during this period. The FCS of today is a basic research tool in several laboratories and companies worldwide [53].

## *B2.0 Instrumentation*

Figure B1, below, shows a FCS setup we have built in our laboratory, with greater detail displayed in Figure B2 and a photograph in Figure B3. Figure B1 shows a general aerial schematic view of the laser and FCS box positions on the air-cushioned optical table. A commercial instrument would have a similar beam path for emission collection, but usually can only accommodate 3 laser wavelengths for excitation. Looking at Figure B2, the excitation beam is reflected up at the sample by the excitation/emission dichroic, through the 60X Olympus UPlanSAPO, 1.2NA water

immersion objective. The sample is a droplet sitting on a No. 1.5 cover slip in Mattek well. The dyes in the sample emit fluorescent light, which is (partly) collected by the objective, passes through the excitation/emission dichroic and is reflected into lens 1 by the emission mirror. The emission light is focused by lens 1 and passes through a long-pass filter (in single color mode), to remove any remaining excitation light and collect only emission photons. A 50 micron pinhole was used to axially limit the effective volume from which fluorescence is collected and to clean up the beam by limiting entry of scattered light into the detector, thereby increasing the signal to noise ratio. [20,21] The light then passes through lens 2 and into the Perkin Elmer avalanche photodiode detector. Please note that the second beam path, starting at the beam splitter after lens 1 is used for cross-correlation and dual color experiments and has been installed for future experiments, but will not be discussed here.

The basic concept of FCS is based on the idea that fluctuations in the intensity of emitted light from a given observation volume may be compared at different time points and correlated to find the probability that a molecule that is in the focal volume at time t=0 will still be there at time t=t. The focal volume is created by a focused excitation beam and confocal detection optics and usually approximated as a three-dimensional Gaussian distribution of the fluorescence detection efficiency. A typical trace over time of the fluorescence intensity from a low concentration sample of dye in water (Alexa Fluor 647 (AF647) excited by a 635nm diode laser) is shown in Figure B4.

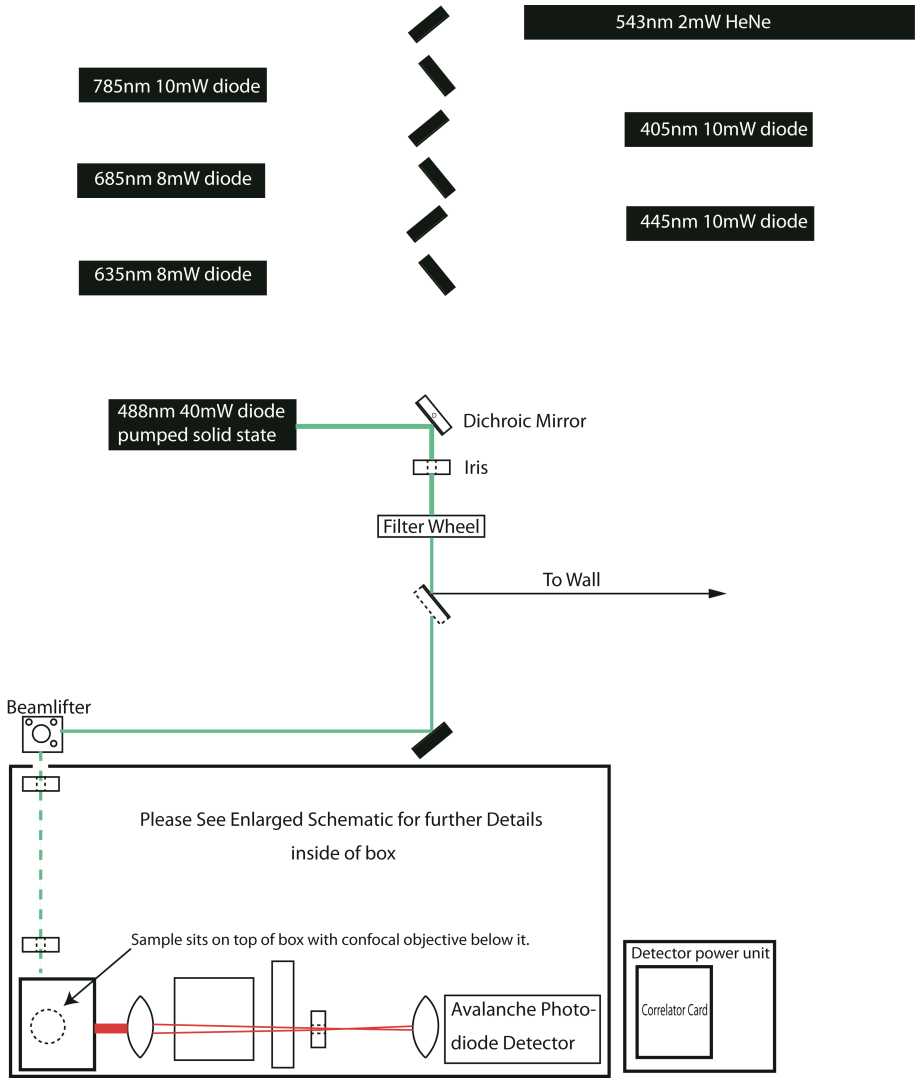


Figure B1: General aerial schematic of our FCS build, indicating position of the lasers, peak power available for each laser and the general view of the beam path.

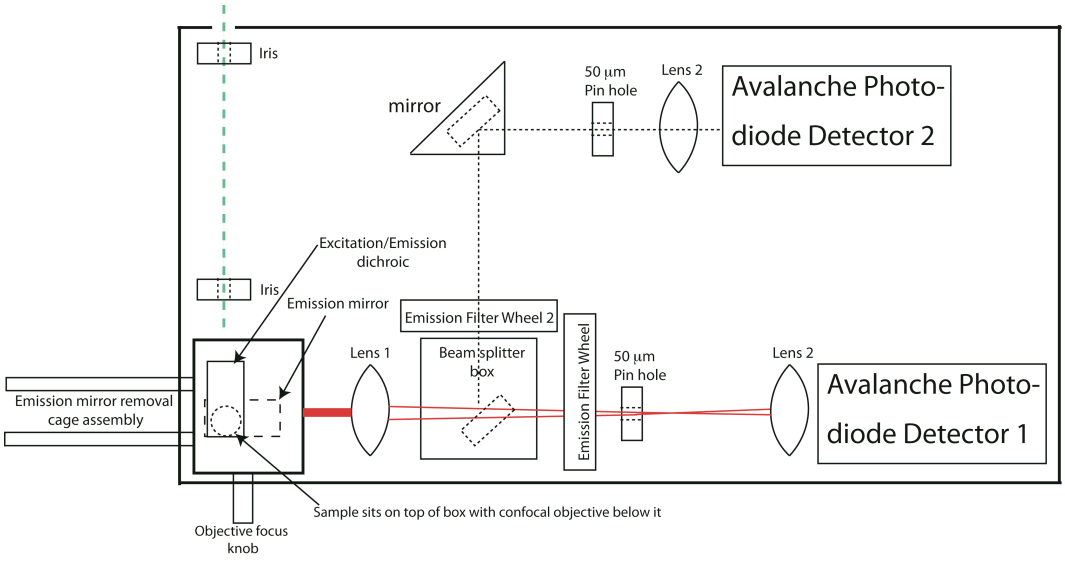


Figure B2: Detailed top view of the internal schematic of FCS box, as built.

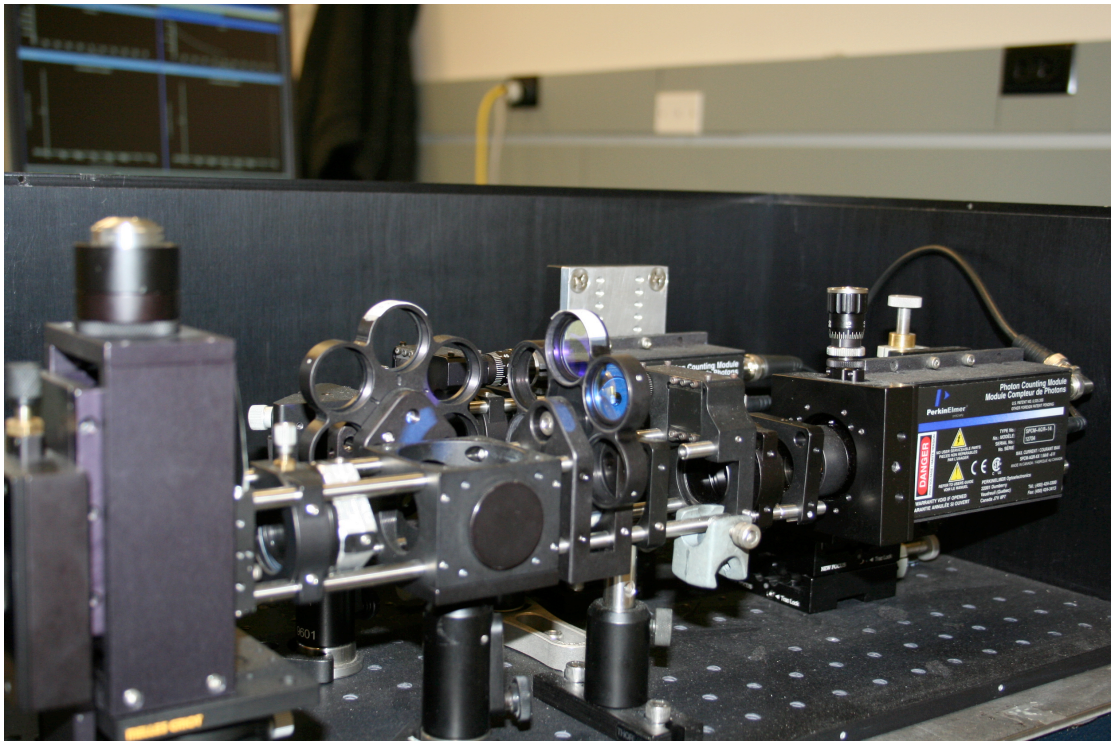

Figure B3: Photograph of the inside of the FCS box, with front and top sides removed. The objective is on the top left and the detector is on the right.

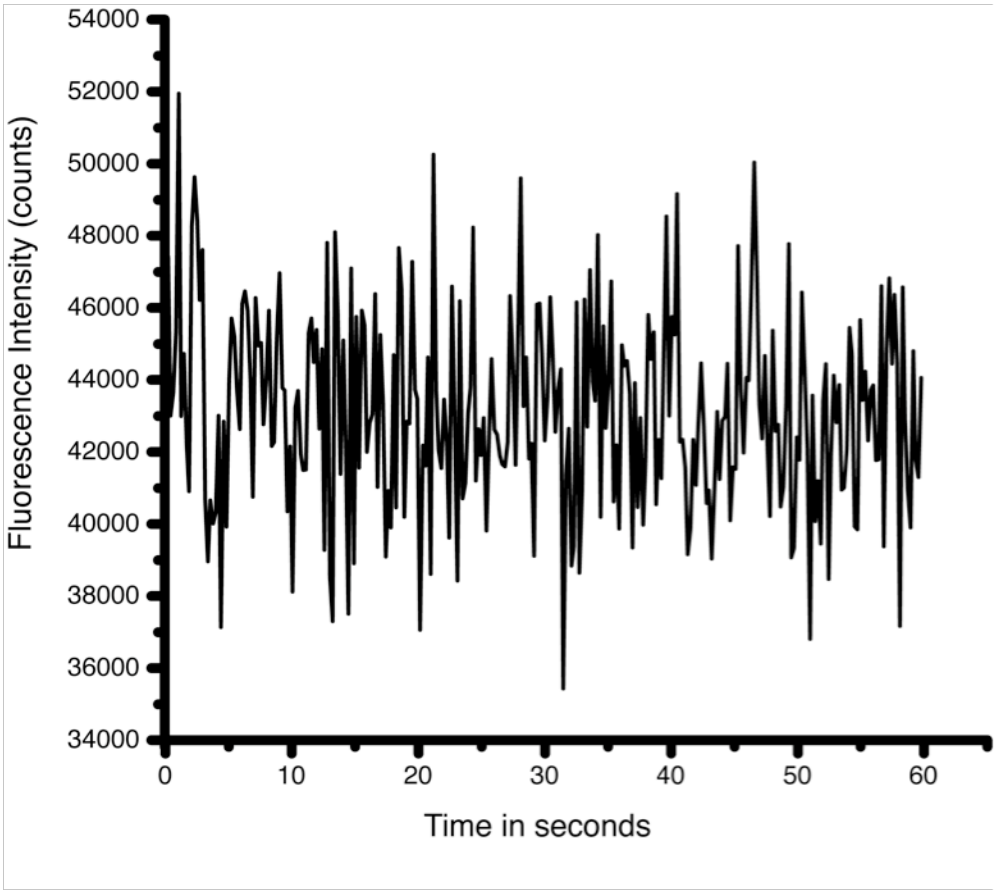


Figure B4: Representative fluorescence intensity vs time plot from Alexa Fluor 647 excited by a 635nm diode laser, taken as raw data in FCS.

From this plot, one can deduce that deviations from an average focal volume fluorescence intensity, or stated another way, the collection of fluorescent molecules within the focal volume, are indicative of one or several molecules entering or leaving the focal volume within a given bin time, to a first approximation. The time and ensemble averages are constant and equivalent for homogeneous samples and may be denoted by $\langle F \rangle$, as defined below in Equation 1 as a time average[54]:

$$\langle F \rangle = \lim_{T \to \infty} \left[ \int_0^T dt F(t) \right] \qquad Eq.1$$

Where F is the fluorescence intensity, T is the time of the experiment and t is the collection time (or bin size in terms of time). The fluctuation of the fluorescence intensity from this average at a given time t is defined as $\delta F(t)$. When $\delta F(t)$ is correlated with the fluorescent intensity fluctuations at a later time, t+$\tau$, and normalized by the square of the average fluorescence (because then the correlation at $\tau$=0 is related to the average number of particles per focal volume), the resulting solution is the primary fit equation, Eq. 2, used in FCS to calculate concentration and the fluorescent molecule or particle diffusion constants. This equation is the temporal autocorrelation function.[55]

$$G(\tau) = \frac{\langle \delta F(t) \delta F(t+\tau) \rangle}{\langle F \rangle^2} \qquad Eq.2$$

A representative plot of data obtained using a correlator.com autocorrelator card is shown in Figure B5, with 5 individual traces (as in Figure B4) autocorrelated and the average and standard deviation plotted.

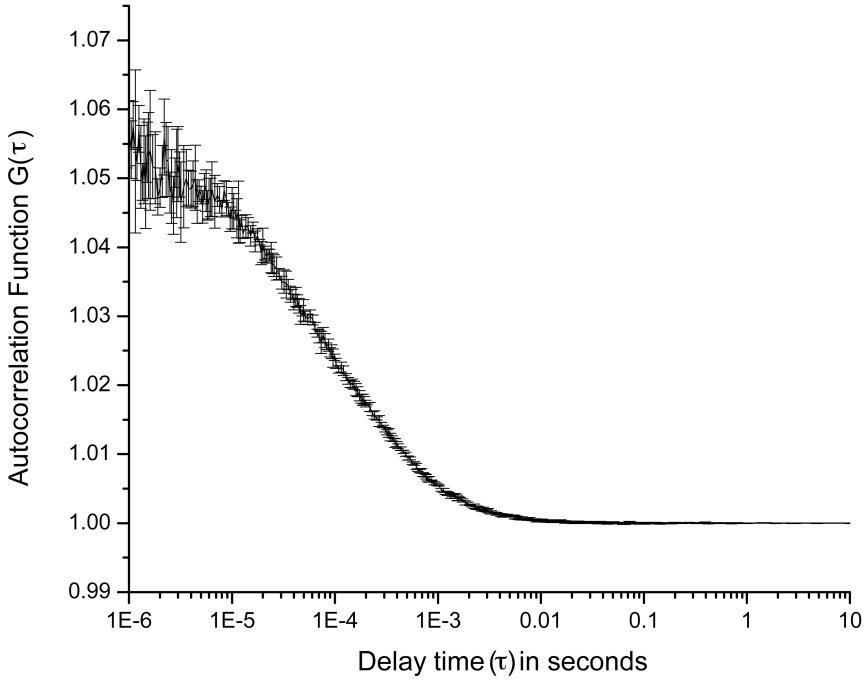


Figure B5: A typical fluorescence correlation spectroscopy autocorrelation curve for organic dye. Shown in this case is the average data from five, sixty second sequential runs on Alexa Fluor 647 excited at low power intensity (0.60mW), averaged. The error bars show the standard deviation over the five runs.

The temporal autocorrelation function may be rewritten in analytical form, as shown in Eq. 3, to allow for direct fitting of the autocorrelation data in Figure B5, explained briefly below and in greater detail in the FCS Users Manual, section B3.0.[56]

$$G(\tau) = 1 + \left(\frac{1}{N}\right) \times \left(\frac{1}{1 + \frac{\tau}{\tau_D}}\right)\left(\frac{1}{\sqrt{1 + \frac{\tau}{\tau_D} s^2}}\right) \qquad Eq.3$$

Where *N* is the number of dye molecules or particles, $\tau$ is the delay time and $\tau_D$ the characteristic diffusion time. The structure factor parameter is denoted by s and is the ratio of the axial over the radial radius of the three-dimensional Gaussian distribution of the fluorescence detection efficiency. The structure factor parameter is determined by fitting Eq. 3 to the autocorrelation data from a standard dye, as in Figure B5 and allowing the parameter to vary freely. A standard dye is one for which the diffusion constant is either provided in literature directly or that has been compared to another dye found in literature and has a diffusion time that is indistinguishable from the literature value (in the case of AF647 the diffusion constant is within less than 5% of AF633, but it is more stable in water). Once the structure factor parameter is determined for a given instrument setup (on a given day), it is then fixed and the equation used to fit unknown samples (and thereby find the diffusion time of the unknown sample).

Since many dyes and even some particles have a triplet state into which the excited state may deviate at high excitation, and which causes the excited molecule to blink on or off (in terms of its singlet state emission) while it is in the focal volume, the autocorrelation function is often amended to include a triplet portion to take account of the anomalous behavior of these molecules. The triplet manifests itself in

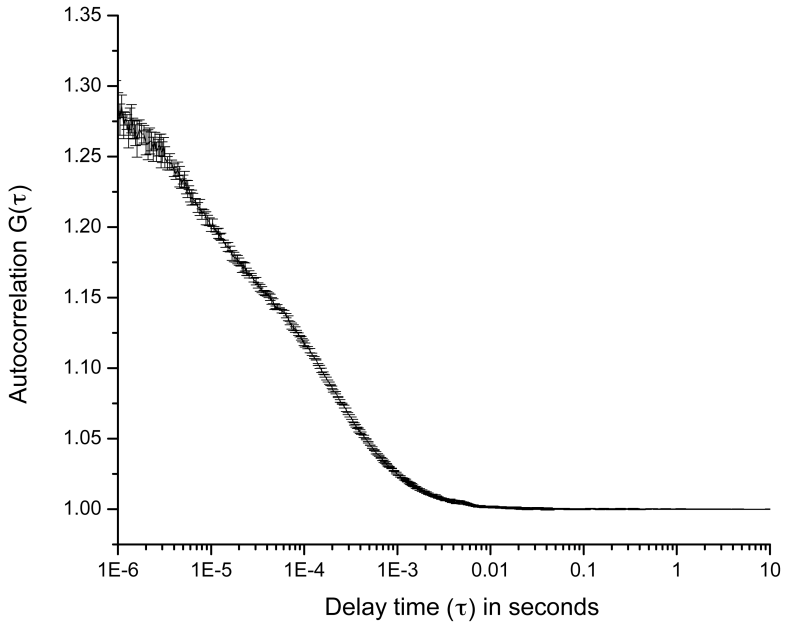


Figure B6: A typical fluorescence correlation spectroscopy autocorrelation curve containing triplet induced artifacts at short time scales. Shown in this case is the average data from five, sixty second sequential runs on Alexa Fluor 647 excited at high power intensity (5.7mW), averaged. The error bars show the standard deviation over the five runs.

autocorrelation data as shown in Figure B6, where the Alexa Fluor 647 dye shown in Figure B5 is excited at a higher laser intensity, introducing an increased short time scale signal to the autocorrelation curve, when compared to Figure B5.

To introduce the triplet correction to the analytical form of the autocorrelation function, an apparent diffusion time of the molecules in the triplet state and amplitude thereof are added to the equation and the normalization factor, as shown in Eq. 4.[22,23]

$$G(\tau) = 1 + \left(\frac{1}{N}\right) \times \left(1 - A + A \times \exp\left(-\frac{t}{\tau_R}\right)\right) \times \left(\frac{1}{\left(1 + \frac{t}{\tau_D}\right)}\right) \times \left(\frac{1}{\sqrt{\left(1 + \frac{t}{\tau_D} s^2\right)}}\right) \qquad Eq.4$$

Where A is the amplitude of the triplet correction, $\tau_R$ is the apparent diffusion time of molecules in the triplet state, and $\tau_D$ is the diffusion time of the molecule in the singlet state. The number of molecules per focal volume is N and the structure factor parameter that describes the three-dimensional Gaussian focal volume is termed s. From these data and the average binned brightness for the focal volume, the average per molecule or particle brightness may be calculated. The three quantities – concentration, particle or molecule hydrodynamic size and brightness are, along with photobleaching resistance, perhaps the most important parameters of interest for fluorescent particle investigations and quality control.

**B3.0 Photobleaching**

Photobleaching is the excited state destruction of fluorescence (and usually the molecule) due to a chemical interaction between the excited dye and an ionic or molecular species. Often photobleaching is more narrowly defined to mean photo-

oxidative bleaching due to the many interactions that occur between oxygen and the excited states of fluorescent molecules.[37,40-42] Furthermore, photobleaching is a specific subset of the more broadly defined stability, which can mean stability of the molecule in solution as a suspension, stability of the fluorescence intensity, or reactive stability of the molecule. Unfortunately, there is no standard means of measuring photobleaching. A relatively common method is to use a strong laser beam with a large physical cross-section and set a cuvette in front of it, measuring the fluorescence intensity from the sample at a right angle to the excitation.[18,57] The challenge with this method is that unless the laser beam is significantly expanded, there are often areas of the sample that are not excited (and constitute a reservoir of non-bleaching molecules) or, because the laser beam has a non-homogeneous (and usually Gaussian) beam profile, reproducing the exact power density distribution over the sample becomes virtually impossible. Measurements taken with this kind of setup often suffer from significant plateaus in the photobleaching due to the effect of the reservoir and difficulties in reproduction due to sample placement. Furthermore, most such measurements rely on a relatively large volume of sample.

Due to these reservations about the current methods employed and a need to decrease the measurement volume, we have built a photobleaching attachment for the fluorescence correlation spectroscopy instrument described above. The photobleaching beam path is identical to the setup shown in Figures B1 and B2 and the photograph in Figure B3, however, the objective is exchanged for a 3.5X, 0.10 NA objective to only lightly focus the beam and allow for a much larger working distance. A positioner is placed on top of the FCS box and used to hold a 0.4mm inner diameter microcapillary tube, aligned parallel to the laser beam with a custom 3-axis tilt mount, as shown in Figure B7.

By filling the microcapillary and aligning it properly with the laser beam, as described in Section B3.6, a sample as small as 2 microliters at concentrations in the nanomolar range may be measured in a repeatable fashion. Absorption matching of samples allows for comparison of the useful lifetime of the particles versus the dyes in identical aqueous solutions with matched concentrations of dye either free in solution or in particles in solution, using the Beer-Lambert law, shown in Eq. 5.

$$\log\left(\frac{I_0}{I}\right) = \varepsilon cd = optical\ density \qquad Eq.5$$

Where $I_0$ is the intensity of the incident light on the sample, I is the intensity of the light that passes through the sample, ε is the molar absorption coefficient, c is the concentration (in moles) and d is the optical path length through the sample. Concentrations should generally be kept such that the optical density at the peak is below 0.1 OD for a 1cm path length cuvette, in order to remain in the linear regime of the Beer-Lambert law. This satisfies the requirement that the molecules are acting independently of each other by insuring that the solution is at a low enough concentration to minimize interaction. Furthermore, absorption matching should be performed at the wavelength that will be used for photobleaching. For example, for Cy5 maleimide dye the absorption matching was carried out at 635nm, the available excitation wavelength for this dye in the FCS/photobleaching setup. An example curve of the absorption matching for Cy5 maleimide and 10nm particles containing the dye, covalently encapsulated within the silica matrix in a core-shell particle architecture is shown in Figure B8.

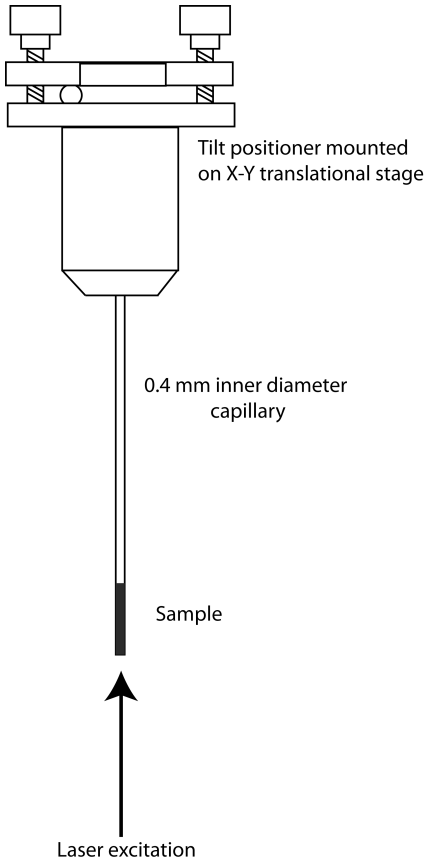


Figure B7: 3-axis tilt positioner for photobleaching samples.

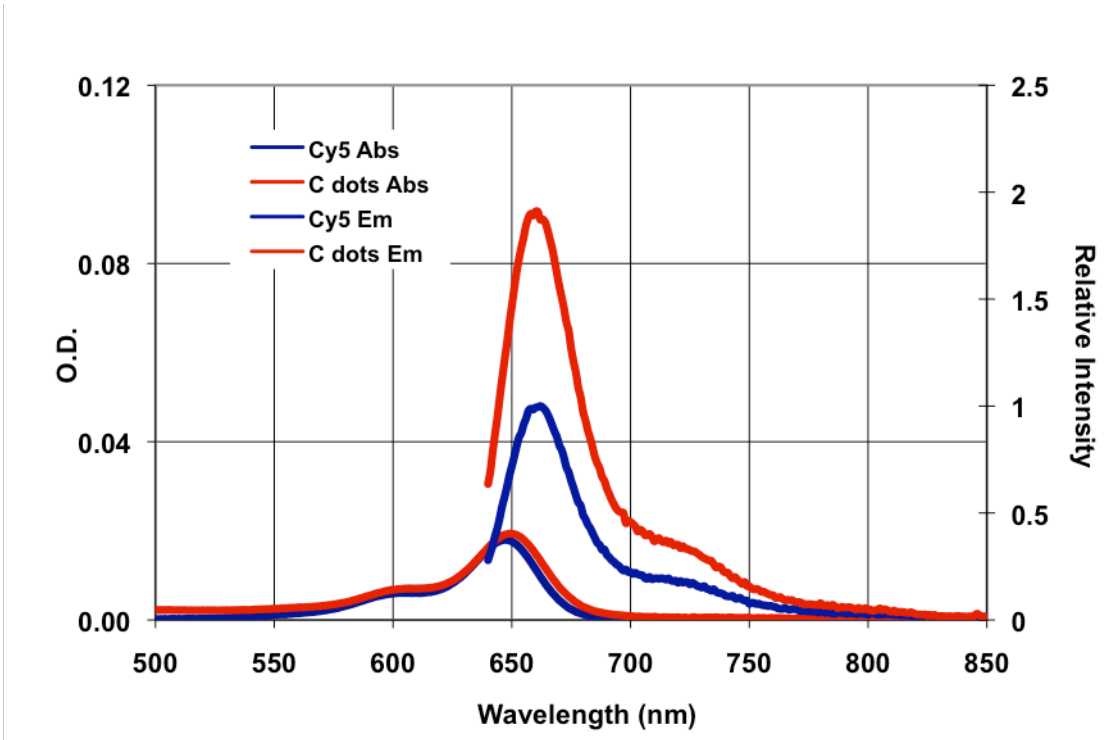


Figure B8: Absorption matching of Cy5 maleimide free dye and Cy5 containing core-shell silica nanoparticles at 635nm (left axis) and corresponding emission (normalized to peak emission of free dye).

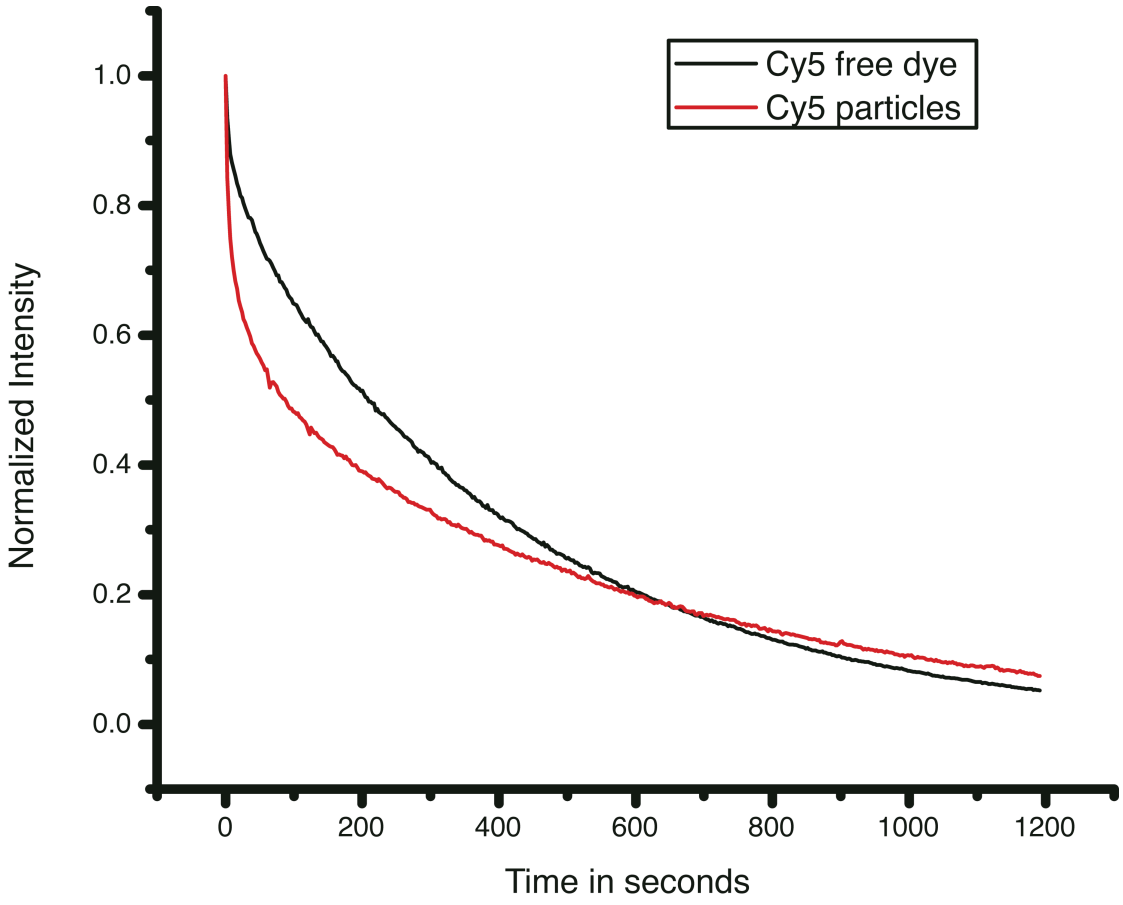


Figure B9: Representative plots of background subtracted and normalized fluorescence photobleaching as a function of time for absorption matched Cy5 maleimide free dye and Cy5 particles.

When the dye and then the particles are excited with 0.6 mW of 635nm laser light for 20 minutes, the drop in fluorescence intensity that results (photobleaching) is shown in Figure B9, normalized and background subtracted. Further discussion and description of background subtraction for these results can be found in the above chapter, here they serve as an example of the photobleaching results collected.

**B4.0 FCS User's Manual**

Except for the 488nm laser, all other lasers are mounted on x-y tilt positioners for ease of positioning the beam. All of the lasers are aligned to the alignment of the 488nm laser because it is bolted directly to the optical table and has the least degrees of positioning freedom. The 488nm laser also fixes the height of the optical beam path outside the FCS box. The dichroic mirror in front of the 488nm laser is designed to reflect laser light below ~500nm and pass light that is greater than 500nm. This means that once the 488nm laser is aligned, the detection system is aligned for all wavelengths greater than 488nm. By placing a mirror between the neutral density filter wheel and the second mirror, pointing towards a solid object (a wall) some feet away, as shown in Figure B2, alignment of two laser beams may be achieved by overlapping the beam spots at the dichroic mirror *and* at the spot on the wall. By extending the beam path, a visual approach may be used to roughly align the beams. Further alignment should be done with a high concentration sample (i.e. 0.1mM for intensity *and* a removable neutral density filter directly in front of the detector). Alignment consists of maximizing the signal for the high concentration sample. Once this has been accomplished, a one to five nanomolar concentration sample should be tested for correlation and, finally a structure factor should be determined for a standard sample with known, literature supported, diffusion constant in water (a list is provided in Table B1).

Table B1: Diffusion constants for standard dyes, with literature references.

| Laser Wavelength | Reference dye | Diffusion constant ($10^{-6}cm^2/s$) | Reference |
|---|---|---|---|
| 488nm | Rhodamine Green or Alexa Fluor 488 | 2.8 or 1.96, respectively | Ref [58] and Ref [59], respectively |
| 543nm | Tetramethyl rhodamine (T-490) | 2.88 | Ref [60] |
| 635nm | Alexa Fluor 647 | 3.0 | Ref [26] for AF633 – matches within 5% but AF647 is more stable |

**B4.1 FCS daily start-up and standardization of the instrument to literature**

Start the laser of choice a half hour before starting measurements. This allows the laser to properly warm up and stabilizes the output. Next, check to make sure the neutral density filters that control the laser intensity (Filter Wheel 1) are correctly set (2.04 total optical density is standard). Making sure that the detector power supply and the correlator card are plugged in, start the computer (if the correlator card is not plugged in, the computer fails to initialize it correctly).

Inside the FCS box, check that the correct long-pass or band-pass filter is in place, using the filter wheel – remember that filters are labeled opposite to their position for ease of identification. This means that when the label for the filter is at the top (and therefore clearly readable), the filter is in the beam path and ready to use.

With the laser beam blocked, put a standard dye sample at the appropriate concentration (for example for the 488nm laser, 30 μL of 15nM Rhodamine Green dye plus 90 μL of de-ionized water) into a microwell dish (MatTek P35G-1.5-7-C) and place on top the of the water immersion objective with a drop of DI water between the objective and the microwell plate. On the computer, start the "Flex01lqmt" program; this is control program for the correlator card. The Flex program is set up with the correlation data (from Channel A) shown in the lower left panel, the fluorescence intensity trace over time in the upper right, the lower right panel remains blank for single detector studies (it is for Channel B), and the upper left panel is for the histogram distribution (this should ideally be Gaussian in shape and may be used as an indicator of good alignment). At the extreme lower left are two labels for Channel A and B, indicating the instantaneous count rate in kHz, or thousands of counts per second. For standardization, as described here, Channel B will always be zero. The sensitivity of the detectors is such that the dark room background is 0.10kHz (the

detectors are 25 count/s dark count detectors) and the maximum count rate allowable on the detector is approximately 1,000kHz for short bursts and 500kHz for long runs.

Reset the correlator card to “Dual Auto” in the drop down box, at the top left of the menu bar. Additionally, change the duration time to 60 seconds. Turn off the room lights and make sure the door to the room is closed. Begin the data collection by clicking the “Start” button. Turn on the detector using the red button on the detector power supply. Keeping your finger on the red button, remove the beam block and check the intensity of light that the detectors are picking up. It is too high if you approach 500kHz in Channel A. For single wavelength fluorescence, there is only one detector in use, so Channel B should show zero intensity. If Channel A is too high (i.e. first numbers appearing on the screen are over 500kHz), shut down the detector immediately and dilute the sample. Once the appropriate intensity has been achieved, the focus should be adjusted, using the focus knob shown in Figure B2. When the objective is fully retracted, the “fluorescence” measured will be very low and may be considered the background. Bring the objective up with the detector running and once in contact with the bottom of the cover slip of the sample, a large spike should be seen as the first and then the second interfaces are passed, with the second being larger than the first due to the dyes that settle or stick to the bottom of the dish. After these spikes, the fluorescence of the sample is being measured and one should bring the objective up far enough to insure that all of the focal volume is within the sample, as indicated by a lack of change with position. After focusing, a series of 15 runs in three sets of 5 may be initiated by clicking on the “S” button (for script). Click the file open icon and create a new folder with today’s date as the name. From a previous day’s folder, copy the “test” file and put it into today’s folder.

Next, open this file. The script text should read, for example:

autosave RhG_OD2.04_A

multiplerun 5

This means that five runs will be autosaved with the file name RhG_OD2.04_A zero to four. The sample name is RhG (for rhodamine green, a standard dye for 488nm), while the optical density (OD) of the filters that control the laser intensity were 2.04, total. The series name was A. Once a set of runs has been collected, turn off the detector. Open the Origin 8 program and go to File-Open Excel File. Open the file named "MACRO for data average and brightness average b" and allow macros, then click on the "Book1" Origin worksheet to reactivate Origin.

Go to File-Import-Multiple ASCII and choose the five ".sin" files you have just created using the autosave function, above. For the example script above, these would be RhG_OD2.04_A0,1,2,3,and 4.sin, respectively. Click Add Files and OK, then unclick Results Log (also note: Add Sparklines should read NO and import mode should read Start New Columns) and click OK on the next screen. This will import the 5 runs in column format and rename "Book1" with the name of the file that was first imported. Select all the columns, copy, and paste into the MACRO Excel file, "Sheet 1", replacing all of the data there. Now, by clicking Alt+F8, open the Macro control panel and run Macro4, which cleans up the data so that only the delay times and calculated correlation values are retained in Sheet 1, Column A and Columns B-F, respectively. Columns G and H are the average and standard deviation of Columns B-F. On Sheet 2, the focal volume intensity values over the 60 seconds are given in Columns B-F, with time (in binned increments) given in Column A. The Average Focal Volume Brightness for all five runs is given in Column G. Next copy all of Sheet 1 in the Excel file and create a new tab in the Origin file by right clicking on the

Sheet 1 tab *in Origin* and selecting Insert, then paste the Sheet 1 Excel data into it. Then set column H(y) as y-error by right clicking on the H(y) header, Set As, Y Error. Select H(yEr±), G(y) and A(x) and right click Plot, Line, Line. Now click Ctrl+Y to open the Nonlinear Fit (NLFit) routine. Under the Settings tab, go to Function Selection, Category, and select the "FCS triplet" function. This function fits Eq. 4 to the data just generated. It assumes that all dyes spend some time in the triplet state and that this needs to be accounted for in the fit of the autocorrelation function.

Continuing under the Settings tab, go to Data Selection and in Weights select No Weights. Then, under the Parameters tab, the following Values should be entered and *not* fixed for the standardization runs: A = 0.2,  = 1e-6,  = 1e-4, s = 0.1, N = 20. These are the initial guesses that the Nonlinear Fit routine uses to fit the FCS triplet function to the given data. Note that N will vary according to the concentration of the sample you are exciting. The number of molecules, N, may be estimated using the Eq. A1.

where G(0) is the value where the fit to the correlation data intercepts the y axis. Hence, for example, the y-intercept in Figure B5 is approximately at 1.05, corresponding to N  20.

Finally, click Fit and wait until the program has gone through the iterations necessary. A window will pop up with all of the fit parameters and their errors, as fit to the current data that is plotted.

For standardization of the instrument to literature values, the following values and error ranges are considered generally acceptable:

A = 0 to .8, error on A in the range of 0.01

TauR = 1e-5 to 1e-7, error on TauR is usually one order of magnitude lower than TauR itself

TauDiff = 1e-4 and up, with variable error, generally one to two orders of magnitude lower than TauDiff.

S = 0.08 to 0.3 error on S should be no more than 1/3 of S

N = 5 to 30 error on N should be no more than 1 molecule

If all of the fit values for set A of the standardization runs are within the proper ranges and errors are acceptable, the second and third runs may be undertaken and fit as described above.

Cumulative data should be collected in the "Concentration and brightness calculation spreadsheet," saved in the same date folder. Make sure that the diffusion constant in the upper left of the spreadsheet is correct for the dye you are using to standardize the instrument. For each run you will need to collect the following data in this spreadsheet: the set name, S, TauDiff, N, and the focal volume brightness. Note that S, TauDiff, and N may be found in the Origin fit result for each set and the focal volume brightness may be found in the "MACRO for data average and brightness average b," in Sheet 2. Knowing these values the spreadsheet will calculate the molecule size, concentration, and average per-molecule brightness using the equations described in the next section. There are two parts to the spreadsheet, the standardization and measurement portions. In this section, the standardization portion

will be used to calculate an average S for use throughout the rest of the day's data collection using this laser, with this power, this concentration of dye and objective focus. Now the instrument is ready for particle or other dye measurements.

**B4.2 Explanation of equations used in concentration and brightness calculations**

As the runs are performed and fit, all necessary data should be included in the "Concentration and brightness calculation spreadsheet." Briefly, the spreadsheet takes the inputs S, Taudiff, N, and the per focal volume brightness, as well as the known diffusion constant of the standardizing dye and the viscosity of the solvent to calculate the particle hydrodynamic size, concentration, and single particle average brightness. An example, starting with the results of the fit routine described above, as applied to Figure B5 and shown with the triplet fit in Figure B10, the equations used will be demonstrated.

In the spreadsheet, the run number and type of sample are designated in column A. The necessary inputs, as mentioned above are listed in Columns B,C,D, and E, for S, Taudiff, N, and the per focal volume brightness. The known diffusion constant is entered in cell B1 and the known viscosity in cell B4. From the entered data, the brightness per particle (or dye) is calculated in Column F. The radial radius of the 3-D Gaussian focal volume, $r_0$, in centimeters is calculated in Column G using Equation A2. Note that the two radii, $r_0$ and $z_0$, and S are only calculated for the standard dye and then remain the same for all particle or unknown dye calculations.

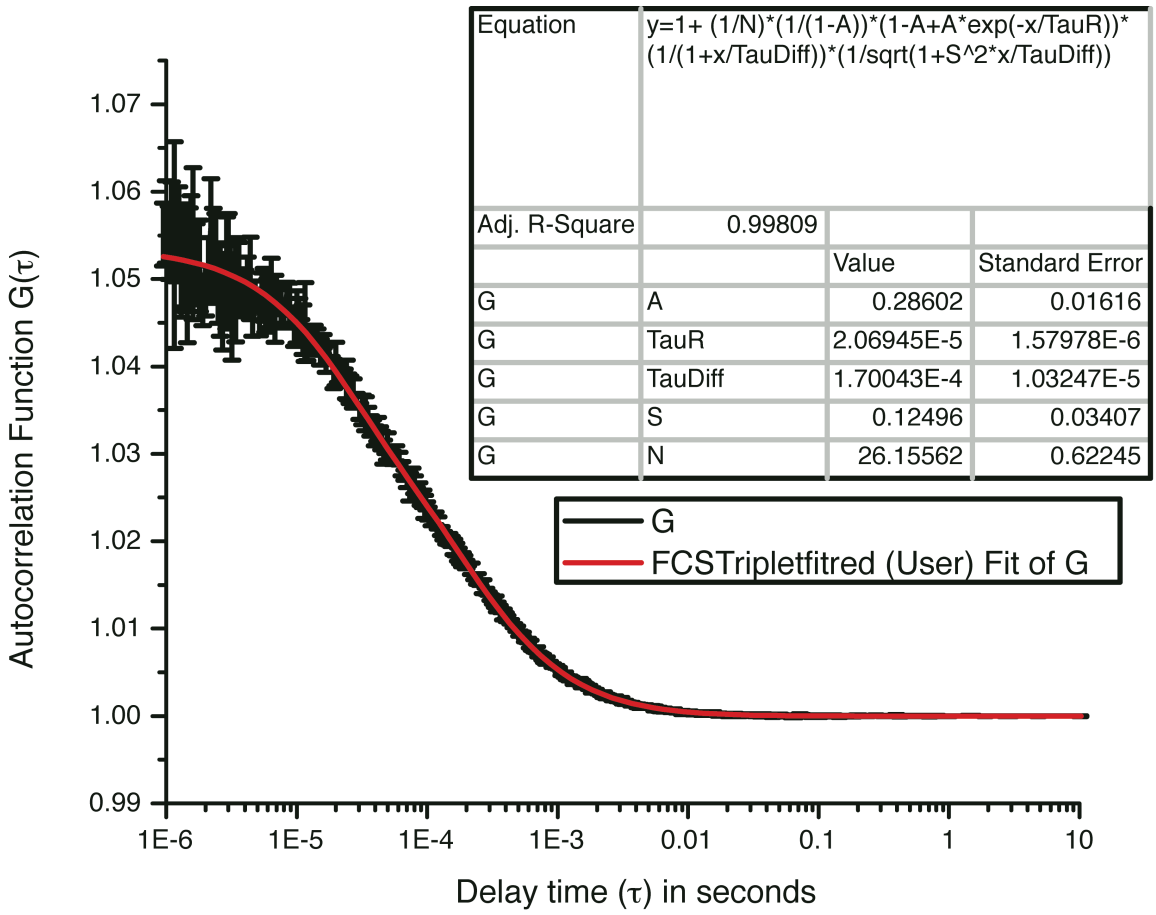


Figure B10: FCS autocorrelation curve (Figure B5) fitted with Eq. 4, with fit results shown in inset.

$$r_0 = \sqrt{4D\tau_D} \qquad Eq.A2$$

The diffusion constant for the standard dye is already known, but for other dyes and particles measured, it is related to $r_0$ by Equation A3 and calculated in Column H of the spreadsheet.

$$D = \frac{r_0^2}{4\tau_D} \qquad Eq.A3$$

Once the diffusion constant is known, the particle or dye hydrodynamic radius may be calculated using the Stokes-Einstein equation, rearranged in the way shown in Equation A4, in the spreadsheet this is done in Column I.

$$r_{particle} = \frac{kT}{6\pi\eta D} \qquad Eq.A4$$

Since the structure factor parameter, S, and the radial radius, $r_0$, has just been calculated, the axial radius, $z_0$, in centimeters may be calculated in Column J, using Equation A5, the definition of the structure factor parameter.

$$z_0 = \frac{r_0}{S} \qquad Eq.A5$$

The *effective* confocal volume in liters is then calculated using $r_0$ and $z_0$, and Equation A6. Equation A6 is the result of integrating the Gaussian form of the measurement volume.

$$V_{eff} = \pi^{\frac{3}{2}} r_0^2 z_0 \qquad Eq.A6$$

Please note that the confocal volume, as defined in some FCS literature is also calculated in Column L, using Equation A7, but is not used further.

$$V_{confocal} = \left(\frac{1}{2}\right)^{\frac{3}{2}} V_{effective} \qquad Eq.A7$$

The concentration of the as measured sample is then calculated in Column M, using Equation A8, where $N_A$ is Avogadro's number.

$$c_{as\ measured} = \frac{N}{V_{effective} N_A} \qquad Eq.\ A8$$

Knowing the dilution factor used to arrive at the as measured sample (entered as total microliters in the measured sample over the added fraction), the concentration in moles per liter of the original (concentrated) sample may be calculated.

**B4.3 Changing the laser excitation source**

To change the laser excitation source, turn on both the laser source last used (and currently aligned) and the laser source to which the setup is being switched. Allow to warm up for ½ hour. Remove the excitation/emission dichroic and the emission mirror by loosening all of the screws holding the left side of the box and then loosening all eight of the set screws associated with the two block mounts of the dichroic removal cage assembly, left of Figure B11. After loosening these screws, gently pull back on the cage assembly to slowly remove the whole emission mirror assembly. Upon completion, the setup should look like Figure B11. Next remove the excitation/emission dichroic holder by grasping the edge of the holder (indicated in Figure B11 with a white arrow), and slowly wiggling the holder loose. Note, please be aware of where the emission mirror is in relation to the holder you are now removing, as a collision would cause damage to one or both and palm prints on the mirror are also to be avoided. Upon removal of the excitation/emission dichoroic, keep fingers clear of the dichroic surface. A couple photographs indicating what the dichroic holder looks like are shown in Figure B12, showing the position of the holder when it is removed and a picture of the dichroic position.

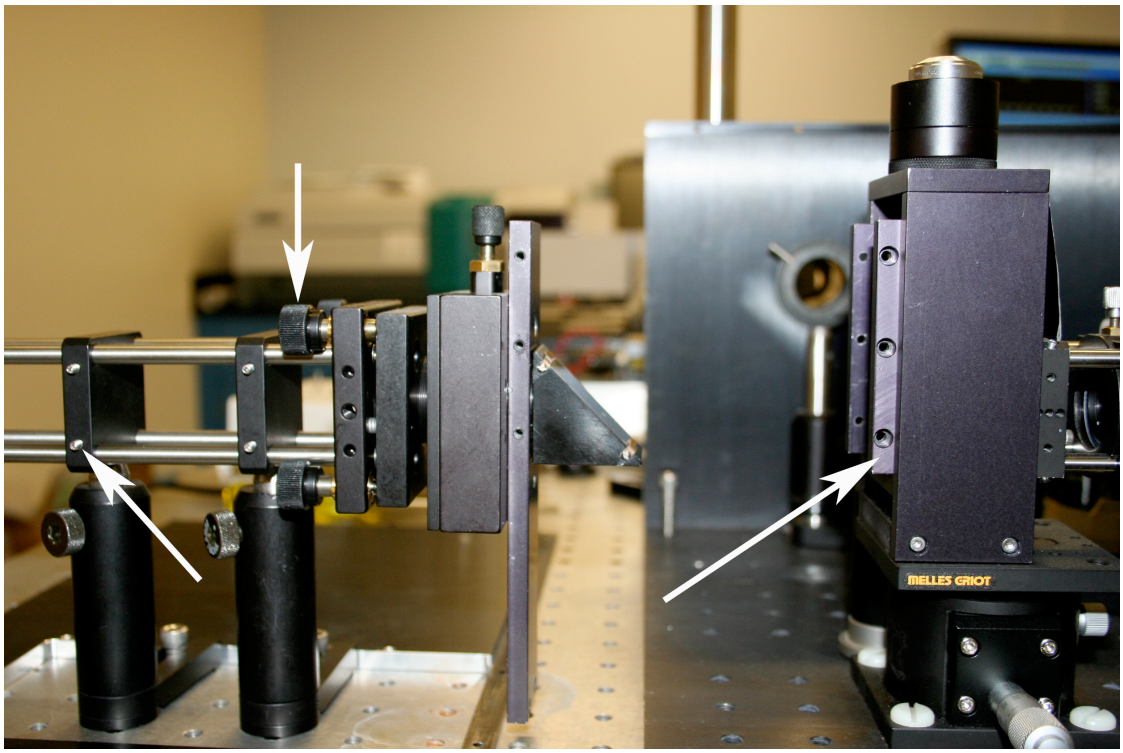


Figure B11: Side view photograph of the emission mirror removal cage assembly in retracted position. Left arrow points to cage assembly mounting screws, the middle wedge shaped mount is the side view of the emission mirror mount. The vertical arrow points to the adjustment thumb screws. On the right is the objective focus column. The right arrow points to the excitation/emission mirror mount, of which only a small portion with three holes is visible.

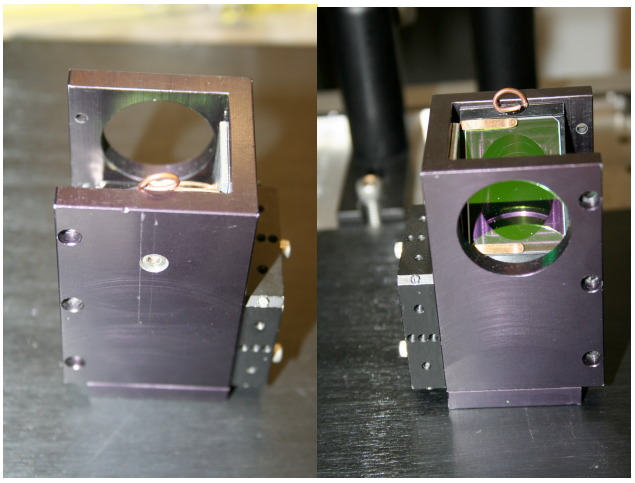

Figure B12: The excitation/emission holder as removed from the FCS (left) and with view of the dichroic (right).

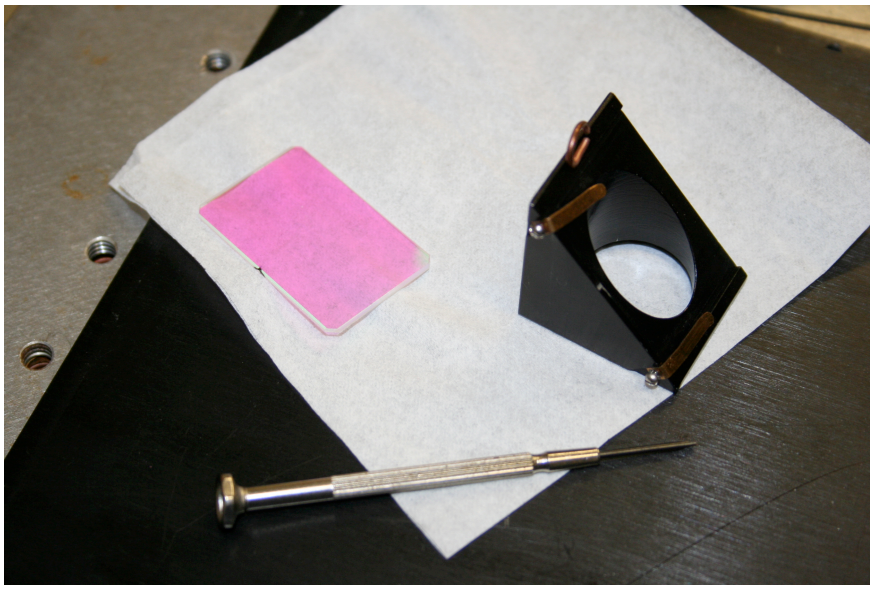

Figure B13: Picture showing the two clamps that hold the dichroic (pink rectangle on left) in place.

The hex screw shown in the left image of Figure B12, at the center of the holder, must be removed in order to pull the excitation/emission dichroic. Once the triangular dichroic holder is removed, two screws on the side of the holder are visible, which hold the two copper clamps in place. These should loosened slightly to allow the clamps to move and then the dichroic may be removed, as shown in Figure B13.

Proper handling of the excitation/emission dichroics is important as they are produced with rather delicate coatings. Figure B14 shows the proper way to handle the dichroic during removal or installation. Upon installation of the new dichroic, all parts should be put back together in the reverse order from which they were removed from the instrument and all necessary screws tightened again. Of key importance are that the excitation/emission dichroic and emission mirror are placed back in the FCS tightly and that the correct emission filter in the filter wheel is chosen (please note that the labeling on the filter wheel is such that the label is directly opposite the filter, so that when the label is on top, the filter is in the beam path). After this is accomplished, alignment of the excitation/emission dichroic may commence using the three thumb-screws on the back of the cage assembly mount (see vertical arrow in Figure B11).

Figure B14: Proper handling of the dichroic by supporting the edges with a cupped hand. To pick up, just pick up by the edges, so as to avoid all finger prints on the optical surfaces.

**B4.4 Trouble shooting typical problems**

1. No correlation:

Make sure that the correct dye and laser are being used. Insure that the correct filters are in place. Check that the sample is positioned correctly and that there is enough water for the water immersion objective. Also check that the collet ring on the objective lens is set to 0.17 (this may require a light source and some contortion to get a good viewing angle inside the box). If the sample is a dye, check that the calculated/expected concentration is in the nanomolar concentration regime or adjust accordingly. If the sample is a particle sample, run two additional runs with a higher concentration and a lower concentration to insure that the lack of signal is not due to lack of intensity (on the low concentration side) or large of a number of emitters per focal volume to measure a clear correlation (on the high concentration side). If all of these things seem to be proper, commence realignment of the excitation mirror, in front of the laser in use, unless another optic is known to have been bumped, or is suspect. Remember that realignment of the excitation or emission half of the beam path should be undertaken sequentially.

2. Significant triplet that cannot be fit with the FCS triplet function:

The first response is to reduce the pump laser power by increasing the neutral density value on the filter wheel. Often this will take care of the triplet. Alternatively, another dye will need to be used as a standard.

3. Spikes in the fluorescence intensity trace:

Spikes in the trace indicate that there is aggregation and the sample either needs to be filtered or a new sample needs to be prepared. Please note that when measuring large particles with high fluorescence dynamic light scattering measurements and other

procedures to minimize aggregation spikes should be taken to avoid damage to the detector.

4. Decrease in fluorescence over the time scale of a single collection run:

When running certain charged dyes, there will be apparent photobleaching on the time scale of a single 60-second collection run. Though unlikely, it is possible the photobleaching *is* to blame, however, often this decrease in fluorescence is due to sticking of the dye to the cover slip. To determine which phenomenon is being observed, take several measurements on the same sample and compare the per-dye (or particle) brightness and number of dyes (or particles) per focal volume. If the number of dyes (or particles) remains constant and the per-dye (or particle) brightness drops, photobleaching is occurring. If the number of dyes (or particles) drops and the per-dye (or particle) brightness remains the same, the dyes (or particles) are being removed from the focal volume by either sticking to the coverslip or by settling out of solution (usually for larger particles).

**B4.5 Moving the FCS**

When moving the FCS, certain considerations need to be taken into account.

1. The idea of having the FCS box pre-aligned will save significant time by allowing you to only have to align the excitation side of the optics to the (already aligned) emission side. If both sides have to be realigned simultaneously, the process becomes more tedious.
2. The FCS box is heavier than it looks and may require two people to carry it without bumping it into doors, etc.
3. There are four through-holes in the bottom of the FCS box that need to be checked for screws that need to be removed first.

4. Expect to spend 3-5 days realigning the instrument after a move (less if you have done it before!).
5. Align the instrument prior to a move, with the cage assembly mounted to the moving plate, as shown in Figure B15 and B16.
6. Make sure to retain enough (5-10mL) of several standard dye solutions at different concentrations to be able to realign the instrument if necessary. Measure these solutions on the day prior to the move and retain data for comparison. Measure the power at the sample for known setups and record for comparison after system has been set up again.
7. Make sure to retract the objective so as to protect it during the move.
8. Avoid placing the instrument or the lasers on a cart during the move unless well cushioned due to the effects of vibrations on the alignment of the FCS box and possible damage to the lasers.
9. Move the FCS box and then install the 488nm diode pumped solid state laser first, as all other lasers must be aligned to this one (it has the least axes of motion).

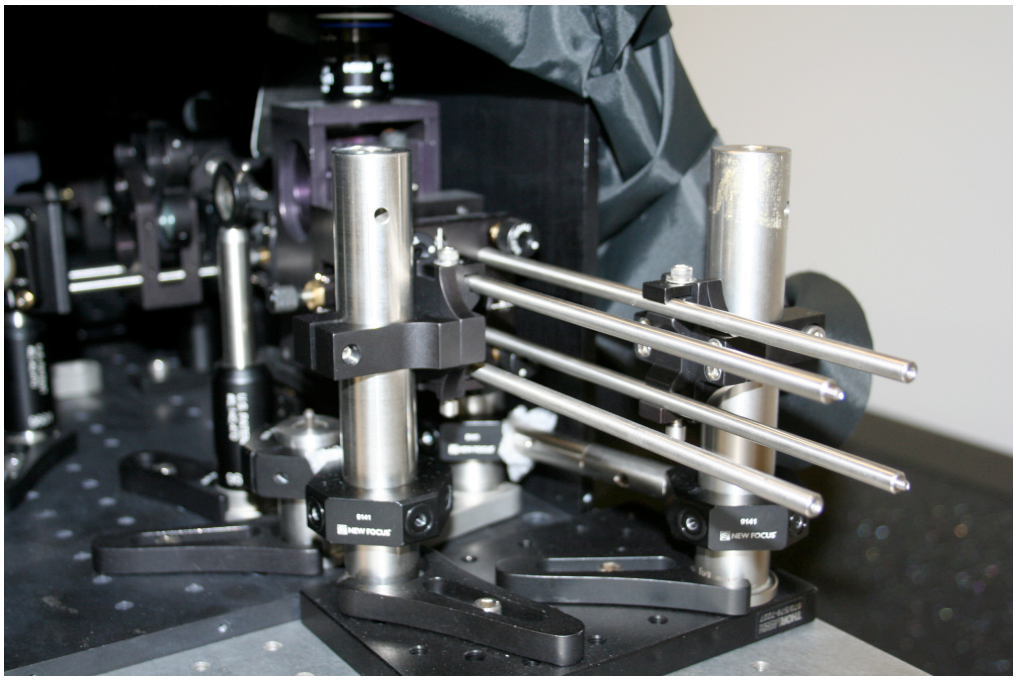

Figure B15: Cage assembly base plate and anchors for moving. Note that there are four anchors; two tall ones hold the cage assembly that are mounted on the moving plate and two shorter ones that are mounted on the inside of the FCS box and serve to hold the taller ones at a fixed distance (see Figure B16).

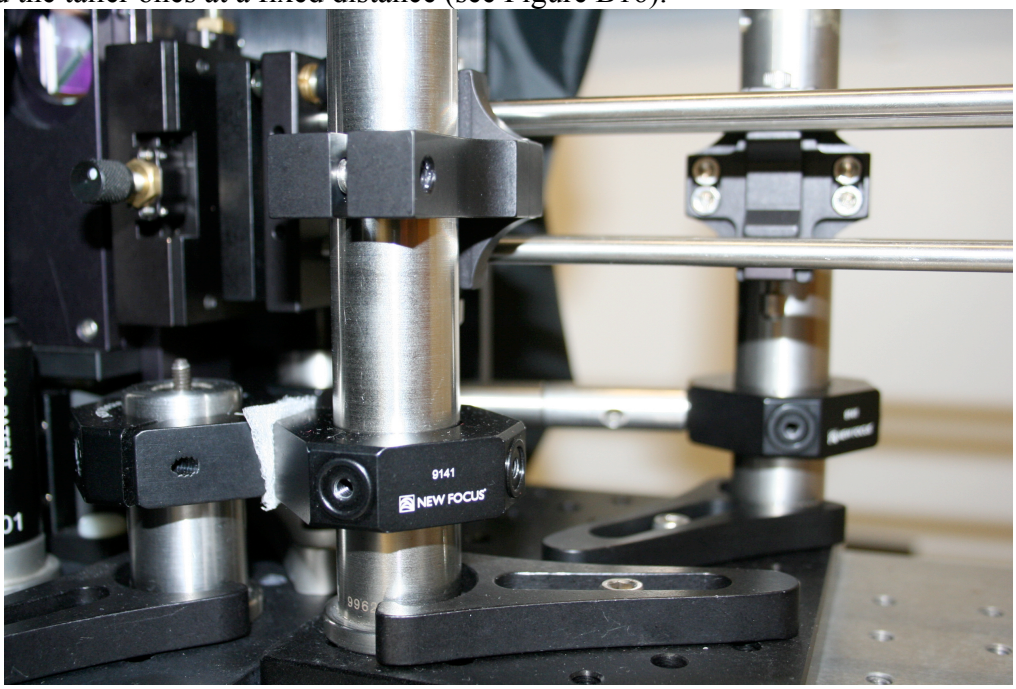


Figure B16: Another view of the cage assembly moving plate and anchors for moving, showing the base plate on right with tall anchors holding the cage assembly and short anchors on left, inside the FCS box tied to the tall anchors by cross ties.

**B4.6 Photobleaching Instructions**

The photobleaching attachment is simple to setup and use, but also very easy to misalign. First, the FCS should be aligned in FCS mode, to insure that the beam paths are aligned. After alignment, the 60X objective may be carefully removed and replaced with the 3.5X objective. It is important to realize that this objective will collect significantly more light and hence, more care must be taken to protect the detector. Next, a glass cover slip should be taped over the hole in the lid of the FCS box, to protect the objective, should the sample slip from the holder and fall. Next, the sample holder should be placed on top of the box. Please note, the sample holder has a very heavy base and must be placed carefully without dropping it onto the FCS box. The lid to the FCS box should be removed and a heavy black cloth should be used to cover the instrument well. This will minimize the amount of displacement that occurs between the capillary and the laser beam/detection when placing or removing the 0.7ND filter in front of the detector (see below).

Next fill a 0.4mm inner diameter capillary tube with 2 microliters of absorption matched sample by measuring the 2 microliters with a pipette and placing the droplet on the inside of a microcentrifuge tube lid (or other appropriately clean surface). Bringing the capillary tube into contact with the sample droplet causes the droplet to be drawn up into the capillary by capillary action. With a total of 2.54 ND laser filters in place to reduce the incident power, place the capillary in the capillary holder, swing it into place (do <u>not</u> tighten the thumb screw) and begin alignment (usually performed in the dark to enhance visibility of the laser light and reflections and avoid damage to the APD detector). In order to align the first capillary well, the x-y translation should be used to bring the capillary into the beam. The two tilt knobs may then be used in tandem to attain the proper verticality. A properly aligned capillary will have a large

scattering of laser light from the top meniscus of the sample and a strong back-reflection visible in reflection from the cover slip.

Once these visual cues are met, the detector may be switched on and a full round of small movements on each of the X-Y and tilt translations should be undertaken to maximize the amount of fluorescence reaching the detector, while still demonstrating the strong back-reflection from the center of the capillary. This visual cue is important because back-scattered laser light from the end of the capillary can provide a false signal that will not bleach. Once aligned, the detector should be turned off and the laser beam blocked before the ND filter wheel. A 0.7ND filter should be placed in front of the detector and the ND filter wheel should be set to 1.04 ND or lower (depending on the expected robustness of the dye). The cloth cover should be replaced well over the FCS box and the lights turned back off. Turn on the detector, set the FCS to run for 1200 seconds (or the desired run time) and the run started. Count to 5 and remove the beam block in front of the laser. This starts the photobleaching run; at this point it is important not to bump the table or otherwise change the environment, this includes increasing or decreasing stray light. If the laser beam has been well aligned, a series of interference fringes will show up on the ceiling during the run.

## REFERENCES


(1) Burns, A., J. Vider, H. Ow, E. Herz, O. Penate-Medina, M. Baumgart, S. M. Larson, U. Wiesner, M. Bradbury *Nano Letters* **2009**, *9*, 442-448.

(2) Parungo, C. P.; Ohnishi, S.; Kim, S.-W.; Kim, S.; Laurence, R. G.; Soltesz, E. G.; Chen, F. Y.; Colson, Y. L.; Cohn, L. H.; Bawendi, M. G.; Frangioni, J. V. *J Thorac Cardiovasc Surg* **2005**, *129*, 844-850.

(3) Bailey, R. E.; Smith, A. M.; Nie, S. *Physica E* **2004**, *25*, 1-12.

(4) Mancini, M. C.; Kairdolf, B. A.; Smith, A. M.; Nie, S. *Journal of the American Chemical Society* **2008**, *130*, 10836-10837.

(5) Chang, E.; Thekkek, N.; Yu, W. W.; Colvin, V. L.; Drezek, R. *Small* **2006**, *2*, 1412-1417.

(6) Kirchner, C.; Liedl, T.; Kudera, S.; Pellegrino, T.; Javier, A. M.; Gaub, H. E.; Stölzle, S.; Fertig, N.; Parak, W. J. *Nano Lett* **2005**, *5*, 331-338.

(7) Altinoglu, E.; Russin, T.; Kaiser, J.; Barth, B.; Eklund, P.; Kester, M.; Adair, J. *ACS Nano* **2008**, *2*, 2075-2084.

(8) Larson, D. R.; Ow, H.; Vishwasrao, H. D.; Heikal, A. A.; Wiesner, U.; W.W.Webb *Chemistry of Materials* **2008**, *20*, 2677.

(9) Ow, H.; Larson, D. R.; Srivastava, M.; Baird, B. A.; Webb, W. W.; Wiesner, U. *Nano Lett.* **2005**, *5*, 113-117.

(10) Choi, J.; Burns, A.; Williams, R. M.; Zhou, Z.; Zipfel, W.; Wiesner, U.; Nikitin, A. Y. *Journal of Biomedical Optics* **2007**, *12*, 1-11.

(11) Burns, A.; Ow, H.; Wiesner, U. *Chemical Society Reviews* **2006**, *35*, 1028-1042.

(12) Piao, Y.; Burns, A.; Kim, J.; Wiesner, U.; Hyeon, T. *Advanced Functional Materials* **2008**, *18*, 3745-3758.

(13) Bringley, J.; Penner, T.; Wang, R.; Harder, J.; Harrison, W.; Buonemani, L. *Journal of Colloid and Interface Science* **2008**, *320*, 132-139.

(14) Herz, E.; Ow, H.; Bonner, D.; Burns, A.; Wiesner, U. *Journal of Materials Chemsitry* **2009**, *in press*.

(15) Herz, E.; Marchincin, T.; Connelly, L.; Bonner, D.; Burns, A.; Switalski, S.; Wiesner, U. *Journal of Fluorescence* **2009**, *submitted*.

(16) Burns, A.; Sengupta, P.; Zedayko, T.; Baird, B.; Wiesner, U. *Small* **2006**, *2*, 723-726.

(17) Fuller, J. E.; Zugates, G. T.; Ferreira, L. S.; Ow, H.; Nguyen, N. N.; Wiesner, U.; Langer, R. S. *Biomaterials* **2008**, *29*, 1526-1532.

(18) Herz, E.; Burns, A.; Lee, S.; Sengupta, P.; Bonner, D.; Ow, H.; Liddell, C.; Baird, B.; Wiesner, U. *Proceedings of SPIE* **2006**, *2006*, 6096-6108.

(19) For a comparison of absorption and emission spectra of free dye versus dye in the particles the interested reader is referred to previous publications (e.g. ref 14)

(20) Rigler, R.; Mets, U.; Widengren, J.; Kask, P. *European Biophysics Journal* **1993**, *22*, 169-175.

(21) Qian, H.; Elson, E. L. *Applied Optics* **1991**, *30*, 1185-1195.

(22) Schwille, P.; Kummer, S.; Heikal, A. A.; Moerner, W. E.; W.W.Webb *Proceedings of the National academy of sciences USA* **2000**, *97*, 151.

(23) Widengren, J.; Mets, Ü.; Rigler, R. *Journal of Chemical Physics* **1995**, *99*, 13368.

(24) Widengren, J.; Rigler, R.; Mets, U. *Journal of Fluorescence* **1994**, *4*, 255-258.

(25) Dittrich, P. S.; Schwille, P. *Applied Physics B: Lasers and Optics* **2001**, *73*, 829-837.

(26) Doeven, M. K.; Bogaart, G. v. d.; Krasnikov, V.; Poolman, B. *Biophysical Journal* **2008**, *94*, 3956-3965.

(27) Williams, G.; Watts, D. C. *Transactions of the Faraday Society* **1970**, *66*, 80-85.

(28) Phalippou, J.; Dieudonne, P.; Faivre, A.; Woignier, T. In *Applications of Sol-Gel Technology*; Sakka, S., Ed.; Kluwer: Boston, 2005; Vol. 3, p 96.

(29) Brinker, C. J.; Scherer, G. W. *Sol-Gel Science: The physics and chemistry of sol-gel processing*; Harcourt Brace Jovanovich: Boston, 1990.

(30) Lindsey, C. P.; Patterson, G. D. *The Journal of Chemical Physics* **1980**, *73*, 3348-3357.

(31) Kassab, K. *Journal of photochemistry and photobiology B: Biology* **2002**, *68*, 15-22.

(32) Gregor, I.; Heupel, M.; Thiel, E. *Chemical Physics* **2001**, *272*, 185-197.

(33) Marling, J. B.; Greg, D. W.; Thomas, S. J. *IEEE Journal of Quantum Electronics* **1970**, *6*, 570-572.

(34) Schaefer, F. P.; Ringwelski, L. *Zeitschrift Naturforschung Teil A* **1973**, *28*, 792-3.

(35) Soper, S.; Shera, E. B.; Martin, J. C.; Jett, J. H.; Hahn, J. H.; Nutter, H. L.; Keller, R. A. *Analystical Chemistry* **1991**, *63*, 432-437.

(36) Weiss, S. *Science* **1999**, *283*, 1676-1683.

(37) Song, L.; Hennink, E. J.; Young, I. T.; Tanke, H. J. *Biophysical Journal* **1995**, *68*, 2588-2600.

(38) Widengren, J.; Rigler, R. *Bioimaging* **1996**, *4*, 149-157.

(39) Johnson, G. D.; Davidson, R. S.; McNamee, K. C.; Russell, G.; Goodwin, D.; Holborow, E. J. *Journal of Immunological Methods* **1982**, *55*, 231-242.

(40) Asimov, M. M.; Gavrilenko, V. N.; Rubinov, A. N. *Journal of Luminescence* **1990**, *46*, 243-249.

(41) Eggeling, C.; Widengren, J.; Rigler, R.; Seidel, C. A. M. In *Applied Fluorescence in Chemistry, Biology, and Medicine*; W. Rettig, B. S., S. Schrader, Ed.; Spring: Berlin, 1998.

(42) Stracke, F.; Heupel, M.; Thiel, E. *Journal of photochemistry and photobiology A: Chemistry* **1999**, *126*, 51-58.

(43) Dubini-Paglia, E.; Beltrame, P. L.; Marcandalli, B.; Carniti, P.; Seves, A.; Vicini, L. *Journal of Applied Polymer Science* **1986**, *31*, 1251-1260.

(44) Eisenbach, C. D. *Makromolecular Chemie* **1978**, *197*, 2489.

(45) Paik, C. S.; Morawetz, H. *Macromolecules* **1972**, *5*, 171-177.

(46) Wiesner, U.; Antonietti, M.; Boeffel, C.; Spiess, H. W. *Makromolecular Chemie* **1990**, *191*, 2133-2149.

(47) Ehrenberg, M.; Rigler, R. *Chem. Phys.* **1974**, *4*, 390-401.

(48) Ehrenberg, M.; Rigler, R. *Quart. Rev. Biophysics* **1976**, *9*, 69-81.

(49) Elson, E. L.; Magde, D.; Webb, W. W. *Biopolymers* **1974**, *13*, 29-61.

(50) Magde, D.; Elson, E. L.; Webb, W. W. *Phys. Rev. Lett.* **1972**, *29*, 705-708.

(51) Eigen, M.; Rigler, R. *Natl. Acad. Sci. USA* **1994**, *91*, 5740-5747.

(52) Rigler, R.; Mets, U.; Widengren, J.; Kask, P. *European Biophysics Journal* **1993**, *22*, 169-175.

(53) Koltermann, A.; Kettling, U.; Stephan, J.; Winkler, T.; Eigen, M. In *Fluorescence Correlation Spectroscopy: Theory and Applications*; Rigler, R., Elson, E. S., Eds.; Springer: Berlin, 2001, p 187-203.

(54) *Fluorescence Correlation Spectroscopy: Theory and Applications*; Springer: Berlin, 2001; Vol. 65.

(55) Thompson, N. L.; Mitchell, J. L. In *Fluorescence Correlation Spectroscopy: Theory and Applications*; Rigler, R., Elson, E. L., Eds.; Springer: Berlin, 2001; Vol. 65, p 438-458.

(56) Pramanik, A.; Rigler, R. In *Fluorescence Correlation Spectroscopy: Theory and Applications*; Rigler, R., Elson, E. L., Eds.; Springer: Berline, 2001; Vol. 65, p 101-131.

(57) Saylor, J. R. *Experiments in Fluids* **1995**, *18*, 445-447.

(58) Foeldes-Papp, Z.; Demel, U.; Tilz, G. P. *Proceedings of the National Academy of Science USA* **2001**, *98*, 11509-11514.

(59) Pristinski, D.; Kozlovskaya, V.; Sukhishvili, S. A. *Journal of Chemical Physics* **2005**, *122*, 014907.

(60) Shueler, J.; Frank, J.; Trier, U.; Shaefer-Korting, M.; Saenger, W. *Biochemistry* **1999**, *38*, 8402-8408.

# CHAPTER 7

# CONCLUSIONS AND OUTLOOK

## 7.0 Conclusions

Fluorescence has been a useful tool in the biological, chemical, security, and information technology fields for over 100 years and will continue to be of interest for the foreseeable centuries as well. Fluorescent particles are a more recent invention and have many uses from the original model colloid to flow tracing and cell tagging. Successful integration of organic dyes into the silica matrix of a sub-micron particle has occurred within the last 15 years or so.

In the work presented here, fluorescent silica nanoparticles of a wide range of absorption and emission wavelengths have been synthesized, building on the previous silica particle work. In depth studies of the scattering corrected relative quantum yield and of near-infrared particle synthesis and photobleaching have been presented. Large Stokes shift dyes have been incorporated into silica nanoparticles, producing sub-10nm particles and allowing for multiplexing with a single excitation source. In support of all of this work, a fluorescence correlation spectroscopy (FCS) instrument was built to allow for testing of fluorescent particle size, per-particle brightness and concentration. The FCS instrument also has the capacity to measure photobleaching over time and was extensively used to that end for investigations of Cy5 and DY730 particles.

* Parts of this chapter have been accepted for publication in *Nature*.

## 7.1 Outlook

Several areas of research interest remain. Of particular importance, in light of the photobleaching data on Cy5 containing particles will be determining synthetic routes and architectures that limit photobleaching even further. Additionally, exploration of multi-colored particles and optimal architectures thereof to minimize energy transfer will be important for barcoding, cell-tagging and demanding security applications. To facilitate multicolor particle research, the FCS instrument was built with the capacity for two color excitation and emission measurements. Finally, introduction of new dyes and dye attributes (such as photoswitchability, photactivatability, or triplet production) is desirable. Some recent work we have done in this area includes the use of absorber dyes as chemiluminescent probes (in our case NIR dyes). Such dyes may be used for the measurement of hydrogen peroxide concentration or as time-delayed fluorescent beacons. Further work should be done in this area to allow the particles to be used in biologically relevant systems.

For successful integration into biological imaging applications, stability in biologically relevant media and targeting the particles at particular cell types, tissues, or organs will be of key importance. Specific antibody, peptide, and other cell uptake/targeting methods will need to be explored. The surface chemistry of the particles, either with electrostatic stabilization or with steric stabilization (as in the case of polyethylene glycol surface modifications), will need to be understood in order to tailor the particle performance. The same holds true for integration into polymer matrix applications, where the surface chemistry of the particles and the size of the particles will dictate how they interact with the polymer chains and the solvents needed for polymer casting.

Another future direction that warrants significant attention, especially from materials scientists is the area of metamaterials. Metamaterials are macroscopic

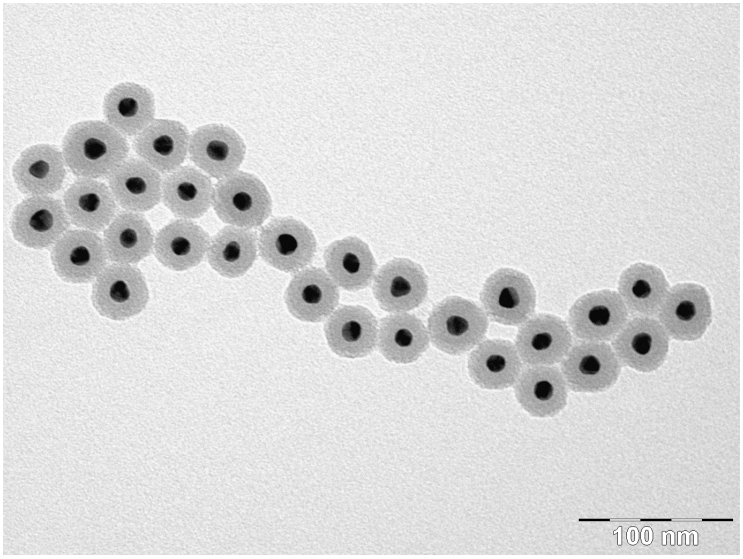


Figure 7.1: An example of a transmission electron micrograph of gold core, dyed silica shell metamaterial particles (courtesy of Teeraporn Suteewong).

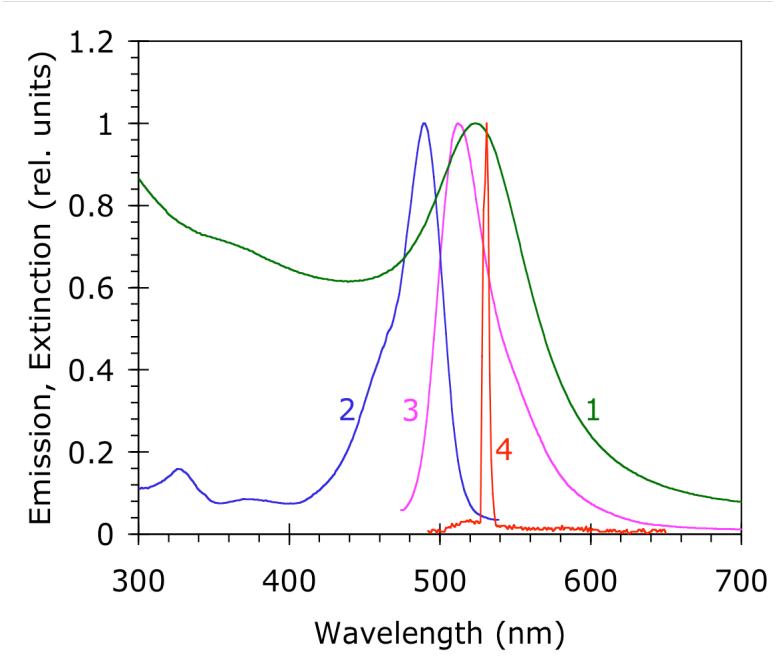


Figure 7.2: Composite plot of normalized (1) Gold particle plasmon extinction, (2) Oregon Green 488 (OG488) dye excitation, (3) OG488 dye emission, and (4) Lasing emission from gold core - OG488 dyed silica shell particles.

composites having a manmade architecture that achieve performance beyond the limitations of conventional materials. The fluorescent silica particle platform, with sizes from sub-10nm up to microns in diameter, are of interest for incorporation into such metamaterials or as metamaterials themselves. To this end, we have explored the production of gold core, dyed silica shell particles to investigate the interaction between the metal surface plasmon and the excited state of the dye. As shown in the transmission electron micrograph in Figure 7.1, such particles may be formed with excellent size uniformity and sphericity at relatively small overall diameters. An example of the surprising results one may obtain undertaking optical investigations of such particles is shown in Figure 7.2. In this composite graph of normalized (1) gold particle plasmon extinction, (2) Oregon Green 488 (OG488) dye excitation, (3) OG488 dye emission, and (4) Lasing emission from gold core - OG488 dyed silica shell particles one can see that with the proper number of dyes per gold core a colloidal nanolaser (and in this case the first demonstration of a SPASER, please see paper) may be synthesized. These results and other similar results indicate that there are many interesting research areas to be pursued, building upon the understanding of how to incorporate the different dyes into a silica matrix. The resulting particles and materials will provide for new scientific understanding in synthetic chemistry and physics as well as enabling new technological advances in the biological imaging and security fields.